ABSTRACT

Title of Document: INTERFACE EFFECTS ON NANOELECTRONICS

Brad Richard Conrad, Doctor of Philosophy, 2009

Directed By: Professor Ellen D. Williams, Department of Physics

Nanoelectronics consist of devices with active electronic components on the nanometer length scale. At such dimensions most, if not all, atoms or molecules composing the active device region must be on or near a surface. Also, materials effectively confined to two dimensions, or when subject to abrupt boundary conditions, generally do not behave the same as materials inside three dimensional, continuous structures. This dissertation is a quantitative determination of how surfaces and interfaces in organic nanoelectronic devices affect properties such as charge transport, electronic structure, and material fluctuations.

Si/SiO_2 is a model gate/gate dielectric for organic thin film transistors, therefore proper characterization and measurement of the effects of the SiO_2/organic interface on device structures is extremely important. I fabricated pentacene thin film transistors on Si/SiO_2 and varied the conduction channel thickness from effectively bulk (~40nm) to 2 continuous conducting layers to examine the effect of substrate on noise generation. The electronic spectral noise was measured and the generator of the noise was determined to be due to the random spatial dependence of grain boundaries,

independent of proximity to the gate oxide. This result led me to investigate the mechanisms of pentacene grain formation, including the role of small quantities of impurities, on silicon dioxide substrates. Through a series of nucleation, growth and morphology studies, I determined that impurities assist in nucleation on SiO_2, decreasing the stable nucleus size by a third and increasing the overall number of grains.

The pentacene growth and morphology studies prompted further exploration of pentacene crystal growth on SiO_2. I developed a method of making atomically clean ultra-thin oxide films, with surface chemistry and growth properties similar to the standard thick oxides. These ultra-thin oxides were measured to be as smooth as cleaned silicon and then used as substrates for scanning tunneling microscopy of pentacene films. The increased spatial resolution of this technique allowed for the first molecular resolution characterization of the standing-up pentacene crystal structure near the gate dielectric, with molecules oriented perpendicular to the SiO_2 surface. Further studies probed how growth of C_{60} films on SiO_2 and pentacene surfaces affected C_{60} morphology and electronic structure to better understand solar cell heterojunctions.

INTERFACE EFFECTS ON NANOELECTRONICS

By

Brad Richard Conrad

Dissertation submitted to the Faculty of the Graduate School of the
University of Maryland, College Park, in partial fulfillment
of the requirements for the degree of
Doctor of Philosophy
2009

Advisory Committee:
Professor Ellen D. Williams, Chair
Professor Theodore L. Einstein
Professor Janice E. Reutt-Robey
Associate Professor Michael Fuhrer
Assistant Professor Min Ouyang

Dedication

To Kelly
&
The owners of the shoulders I have stood on

Acknowledgements

My decision to study at the University of Maryland, although to a large degree a random event, is by no means something I would change if given the opportunity. I consider my opportunity to work with Ellen to be the best thing that ever happened to me as a scientist. Ellen was always available when I needed assistance, yet I always felt as if the research I was embarking upon was truly of my own design. She expected nothing less than excellence from me and my only hope is that I didn't let her down too often. In Ellen's group, I wholeheartedly thank Daniel Dougherty, Michelle Zimmermann, Blake Riddick, Chenggang Tao, Tracy Moore, Dan Hines, and Elba Gomar-Nadal, who contributed in equal parts.

Part of why it saddens me to leave UMD is the plethora of people who amaze me on a regular basis. One of those people is Professor Ted Einstein and accordingly, it would be dishonest of me to not acknowledge the role that Ted played in my education. I cannot count the number of times I have gone to Ted's office and had the most complex made simple and had what appeared to be the most simple made the most complex. In both cases, I am a better physicist for it. The value of such interactions, those between Ted's group and Ellen's group, cannot be overstressed. And above all else, I consider Professor Ted Einstein to be a true scholar, a true gentleman, and a true friend.

I cannot forget to include Janice Reutt-Robey, Michael S. Fuhrer, and Min Ouyang in a list of those who have influenced me. I have grown to know their groups quite well and been assisted by them probably more time than they realize. And, thanks to them, I now know all the equipment bartering rules. In terms of (their)

students, of particular note are Dan Lenski, Wei Jin, Dave Tobias, and Adrian Southard.

I would also like to acknowledge all of the Physics Department and MRSEC staff for all of their assistance and friendship. I want to specifically mention Jane Hessing, Linda O'Hare, Donna Hammer, Julie Callis, Carolyn Garvey, and Alex Prasertchoung.

I cannot forget to thank three individuals that I have spent my entire graduate school career with: Colin McCann, Peter Redl, and Simon Slutsky. I'm grateful for them putting up with me all these years. And it would be a mistake to not thank Bill Cullen. He was an invaluable resource, played a vital role in every experiment that I accomplished, and was a great friend. I like to think that all my 'good' lab habits come from Bill. You will be missed.

Table of Contents

List of Tables

List of Figures

Chapter 1: Introduction

Societal trends increasingly demand the incorporation of electronics into many aspects of our daily lives. This push in the direction of ever-more-present chemical sensors, flexible displays, RFID communication tags, hand-held readers, and portable power supplies is driving the need for smaller, less expensive and more efficient electronic materials and components[1]. In addition, the demand for ever-faster computing technology requires more logic circuits in a similar or smaller volume. In order to accommodate these socioeconomically driven areas of development, we must understand how both new materials and the reduction in size of current technologies affect electronic transport.

1.1 Motivation

As this new field of device development has evolved, it has become apparent that the use of new materials, such as organic semiconductors, is a promising solution to many problems that are not easily solved by traditional silicon devices. Since the early advances of integrated circuits, the material of choice for manufacturing electronic structures has been silicon. Extremely abundant, this element is well understood and relatively easy to generate and modify. However, there are several reasons why silicon is not the ideal material to use for this new, developing class of low power, ubiquitous devices. In conventional configurations, silicon devices are rigid, brittle, and optically opaque. Also, the process of generating device quality Si is relatively energy intensive and environmentally taxing[2]. Therefore, as these devices become more prevalent, the energy wasted and potentially irreversible environmental damage will scale with the number generated.

It is possible that another category of materials, based on organic molecules and polymers, can be used for this novel class of electronic devices. Organic materials are generally soft, or relatively flexible, materials[3]. They can be processed on inexpensive, flexible plastics, are compatible with existing high-throughput roll based printing technologies, and can be made transparent[4]. These attributes make organic semiconductors promising candidates for electronic components such as transistors, diodes, chemical sensors, and large area photovoltaics.

As is true with traditional silicon technology, surface effects are not only important but can dominate device characteristics. The basic electronic device that

will be used to study the relationships between surface effects and charge transport in this dissertation is the thin film transistor (TFT). In such devices, it is well known that the majority of the transport is limited to the layers of the conduction channel in intimate contact with the surface of the gate dielectric, suggesting that surface characterization is vital to determining transport characteristics, especially for large area device geometries. Film morphology also plays a critical role in determining transport in TFTs since the conduction channels are often composed of not a single crystal but a polycrystalline material, creating grain boundaries. The regions between grains can be ill defined, creating charge-carrier trapping locations, disrupting transport and decreasing device lifetime. It is also well known that metal-organic interfaces, such as electrical contacts, can vary wildly over nanometer length scales and can generate static dipole fields. Therefore, it is vital that the surfaces composing a device and their effects on transport be well understood if progress is to be made in the field of organic electronics.

As this new class of devices decreases in size, just as traditional electronics have, surface phenomena and electronic properties become ever more important to fundamentally understanding transport mechanisms. As devices decrease in size, a larger fraction of the total active region becomes surface-property dependent. And since the properties of materials at the surfaces, such as statistical properties and energetic excitations, often differ from the bulk, we expect devices to behave differently as they decrease in size. And as these devices realize their full potential by decreasing to truly nanosized length scales with a finite number of constituents,

quantum mechanical effects will begin dominate the electronic structures, further altering transport characteristics.

1.2 Organic Semiconductors

The study of organic semiconductors, particularly the effects of surfaces, doping, and morphology on electronic properties, remains a very active area of development[4-8]. Considering the wide variety of properties, both electrical and physical, interest in developing commercially viable organic materials is well founded[9-11]. Since these materials are chemically engineered to begin with, further chemical modification and chemical blending allows for the tailoring of properties, unlike silicon[12, 13]. Furthermore, many organic-semiconductor materials can be suitably deposited using high-output methods, such as ink-jet, transfer printing, drop casting, and spin coating on a variety of substrates: hard, arbitrarily shaped oxide surfaces such as SiO_2, transparent glass, flexible polymers, and even other organic materials. This flexibility in deposition allows for a rich variety in the possible low-cost applications: chemical sensors, energy harvesting solar cells, logic circuits, analog electronic devices such as transistors or diodes, and even communication devices such as RFID tags.

Although the study of organic semiconductors is not new[14], the last few years have seen a rapid acceleration in the reports on both mobility and commercially feasible materials[15]. Early advances in organic semiconductor technology were primarily accomplished by the traditional, heavily funded electronics research groups: government laboratories and silicon semiconductor companies[16]. As the performance and range of viable organic materials has increased, interest has

broadened to include the academic community and those interested in engineering commerial applications[17, 18]. The initial breakthrough in realizing the potential of organic materials really began with the studies of molecular chain transport in 7,7,8,8-tetracyanoquinodimethane (TCNQ) around 1960[19]. In terms of applications, the discovery of fluorescence in anthracene crystals in the mid 1960's hinted at the successful future of organic light emitting diodes (OLEDs)[20, 21]. The (accidental) discovery of organic molecule doping (in this case polymer doping), such as the tailoring of film conductivity over 11 orders of magnitude by varying impurity levels on the order of 1%, accelerated organic transistor development[22].

Due to these early advances and much more recent work, organic semiconductors have become commercially viable. Of all the different classes of organic devices, OLEDs have seen the highest levels of accomplishment, and have been successfully incorporated into many products as small-scale retail displays in digital cameras, cell phones, and other hand-held electronic electronics. OLEDs are even currently being used in commercial large-scale (>27 inches) televisions from Samsung and Sony in late 2008[23] and early 2009[24]. The motivation for developing OLED displays includes several important advantages OLEDs have over the current liquid crystal displays (LCDs). OLEDs can be printed on a variety of substrates, including flexible substrates, enabling novel device structures. OLEDs have faster response times, higher on-off contrast ratios, a larger number of possible colors, consume less energy in the off state, and can be packaged into a smaller volume than comparably sized LCDs.

1.3 Charge Transport In Organic Semiconductors

Organic semiconductor properties, particularly in terms of charge transport, are fundamentally different from those of traditional semiconductors. One of the most basic yet most important differences is that the structure of these materials is mostly determined by weak van der Waals interactions, imparting the properties of both semiconductors and insulators[25]. Van der Waals dispersion forces originate from the instantaneous charge fluctuations, or multipole moments, within a net charge neutral molecule. These multipole moments induce moments in neighboring molecules, generating moment-moment forces that are always attractive for the distances of interest for organic films (~1 Å). Other generators of van der Waals forces can come from permanent multipole moments in the constituent molecules, generating forces in manner similar to instantaneous charge fluctuations while inducing additional moments in other nearby molecules. These types of forces can be attractive or repulsive on the length scales of interest. In comparison, traditional semiconductors' structure is formed by covalent interactions, relatively strong forces arising from charge sharing between individual neighbors. Despite knowing the relevant organic molecular interactions, details of charge transport are typically dependant on material and even deposition conditions since organic materials vary in terms of molecule or complex size, atomic configurations, and even transport mechanisms.

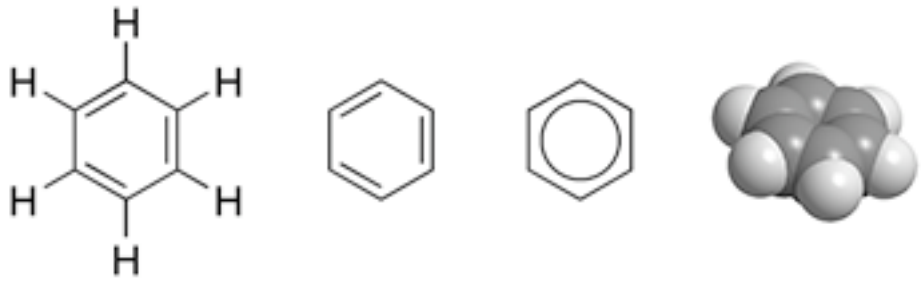

Figure 1.1: Illustration of various representations of beneze, C_6H_6. (Image care of cacycle, Wikimedia Commons)

Currently, it is common to divide the structure of organic semiconductors into several broadly defined, overlapping categories: small molecules, 'large' carbon-based structures, organic-inorganic structures, and polymer chains. Although varied in terms of structure, the property of conduction is usually attributed to the conjugated bonds present in these materials. Bond conjugation usually refers to the alternation of concurrent single and double carbon bonds, either in a chain or in a ring. As an example, materials composed of only carbon, due to the bond conjugation of the four electrons per carbon atom, have three sp^2-hybridized orbitals forming single (sigma) bonds while the remaining hybridized p orbital forms a pi-bond with a neighboring p orbital. Since sigma bonds are strong covalent bonds, electrons tend to be highly localized between the involved atoms and not involved in conduction. Due to a decreased amount of electron wave function overlap in the constituent p-orbtials, pi-bonds tend to be weaker than sigma bonds. Therefore, pi-electrons tend to be non-localized over the entire molecular bond. Pi-orbitals can be chemically constructed adjacent and planar to other pi-orbitals, allowing for pi-electron delocalization along the continuous conjugated bonds, as illustrated in the third graphical representation of

benzene in Figure 1.1, where three pi-bonds are shared over all six carbon-carbon bonds.

When organic molecules are brought in close proximity to each other by the previously described weak dipole interactions, well-defined structures may form. If a well ordered structure forms, such as a crystal, and the molecular constituent pi-orbitals of each molecule sufficiently overlap, charges are free to migrate between molecules and, ideally, over the entire well-ordered structure. If a less ordered structure or crystal forms with farther spaced, non-overlapping pi-orbitals, it is possible that the pi-orbitals are close enough to allow for tunneling between orbitals at reasonable energies. Such a transport process is generally referred to as charge hopping. It is even possible to have materials that are polycrystalline, including both modes of transport. As a result of the variety of conducting structures possible, organic semiconductors are typically considered wide band gap semiconductors because the the energy region void of electronic states (band gap) can range up to 4 eV[14]. From this quantity alone, insulating behavior might be expected for a substantial subset of these materials. However, various techniques are commonly and easily employed to allow for conduction through these materials: chemical doping, photon excitations, and electrode/device charge injection.

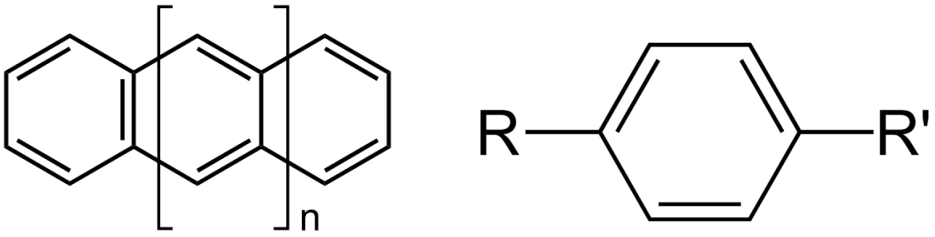

Figure 1.2: Illustration of the general chemical structure of acenes and phenylene (Images care of Wikimedia Commons).

Figure 1.3: Illustrations of anthracene, tetracene, and pentacene (Images partial care of Wikipedia Commons).

The first group of organics to be studied consisted of relatively small aromatic hydrocarbon rings, such as TCNQ and anthracene[20, 21, 26, 27]. In general, they are formed from acenes and phenylenes, which are shown in Figure 1.2. Commonly used members of the acenes group include anthracene, tetracene, and pentacene, as seen in Figure 1.3. Materials of this group, specifically pentacene, have produced working devices with mobilities as high as 35 cm^2/Vs, in pentacene single crystals at room temperature[28]. These small molecules are also often modified chemically in an attempt to modify their deposition properties and prepare more useful, robust materials[29, 30]. One of the primary limitations to development is the large derivative phase space. As an example, one of the earlier high mobility pentacene studies was conducted in 1996 by Dimitrakopoulos[31] but successful attempts to modify the pentacene's chemical structure to allow for greater pi-orbital overlap and air stability, specifically 6,13-bis(triisopropyl-silylethynyl) pentacene (TIPS-pentacene), were not seen in the literature until 2001[32].

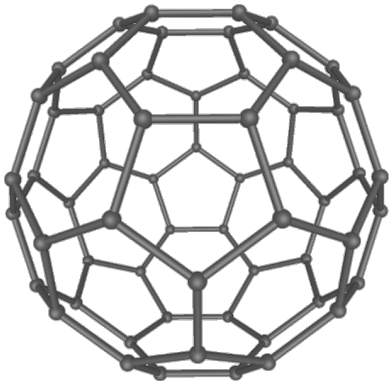

Figure 1.4: **Illustration of C_{60} (Image care of Michael Ströck, Wikimedia Commons)**

Commercially viable organic semiconductors are not limited to small molecules. One of the most exciting developments in the field has come from fullerenes and carbon allotropes. One of the simplest carbon structures is a sphere of carbon and is illustrated in Figure 1.4. The first carbon allotrope to be heavily studied, C_{60} has a soccer ball like structure consisting of sixty carbon atoms. Discovered in 1985, C_{60} was eventually dubbed buckminsterfullerene, or the buckyball[33]. In this structure each carbon atom is bonded to three other carbon atoms with sp^2 bonds with average bond lengths of 1.44 Å, similar to the 1.42Å bond length of graphene[34]. It was first used to form a working field-effect transistor in 1993 and studied by single molecule experiments in 2000[35, 36]. This structure is naturally semiconducting with mobilities in excess of 1 cm^2/Vs and is commonly doped with a wide variety of materials potentially resulting in much higher mobilities[37]. Doped C_{60} also has the special property of becoming superconducting at moderate temperatures[34, 38].

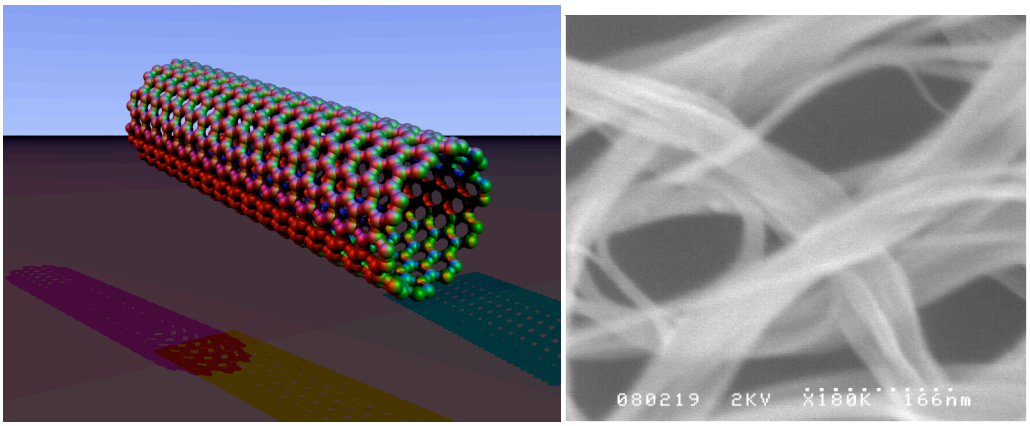

Figure 1.5: **a) Illustration of a single walled carbon nanotube. (Image care of Wikipedia commons) b) Scanning electron microscope image of a carbon nanotube mesh, taken at 2kV (Image care of R. Raffaelle, RIT).**

If buckyballs were elongated, thus forming a tube of sp^2 bonded carbon atoms, the result would be carbon nanotubes (CNTs) as illustrated in Figure 1.5 without the spherical endcaps (which are not necessary). After the discovery of CNTs in 1991[39], intense research efforts over the last two decades have lead to an immense number of papers discussing applications for electrical components, sensors, biological applications, and many more diverse uses[40, 41]. Part of reason for interest in CNTs is their remarkable physical and electrical characteristics. In terms of physical strength, a multi-walled CNT was reported as having a tensile strength of at least 63GPa, at least a factor of 30 higher than the best steel[42, 43]. Carbon nanotubes have been incorporated into many materials to increase strength[44], flexibility, and electrical conductivity[43, 45, 46]. Electrically, CNTs display both semiconducting and metallic behavior, depending on the chirality, and have been made into field effect transistors using the semiconducting nanotubes[47]. Among the many current research initiatives, methods of controlling or selecting CNT size, length, and electronic properties are among the most sought after[25].

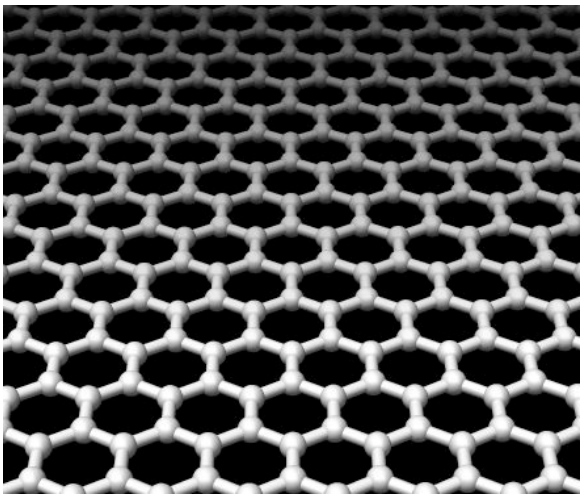

Figure 1.6: **Illustration of graphene. (Image care of Wikimedia Commons)**

It is also possible to simply have the planar material that is rolled up to form fullerenes and CNTs, namely graphene. Graphene, the base allotrope of carbon, is a single sheet of sp^2-bonded carbon in a honeycomb lattice, or a single layer of graphite, as illustrated in Figure 1.6. First isolated in 2004, it has been shown to have remarkably high mobilities[48], doping-dependent electrical properties[49], and even form excellent insulating layers through oxidation[50]. Graphene has also been incorporated into printed, flexible electronic devices[51]. Graphene is a zero-band-gap semiconductor, giving rise to conduction and valence bands touching at two points, called Dirac points. This is novel because metals have overlapping conduction and valence bands while semiconductors have a gap between them. Therefore the material is somewhere between a metal and a semiconductor since the valence and conduction bands only meet at two singularities. The existence of the Dirac points leads to charges behaving analogous to relativistic quasiparticles, called Dirac fermions[52]. An important consequence of this is that these Dirac fermions travel through graphene at constant velocity irrespective of energy and direction[53].

Graphene's high potential mobility results from many factors: high Fermi velocity, high sound velocity, small electron-phonon coupling, and the absence of backscattering due to pseudospin.

More complex materials, namely polymers, are among the earliest organic electronic successes and to this day remain an active area of development in the field[54, 55]. Polymers are composed of repeating structural units, or monomers, that are connected by relatively strong covalent bonds. Heavily used in commercial applications[56], polymers are typically easily formed from solution processes, allowing large area, high-throughput manufacturing. Major developments occurred in the field of semiconducting polymers, specifically the development of polymeric field-effect transistors (FETs) and electroluminescence, in the 1980s[25]. One of the first successful polymeric transistors was developed in 1983 using polyacetylene[54] while the first polymer chemical sensor was developed using polypyrrole in 1986[17]. Of all the polymer systems studied thus far, one of the most studied device polymers is poly-3-hexylthiophene (P3HT)[57]. The first completely solution-processed polymer devices, developed by Assadi et al., had organic films that were spun cast by P3HT dissolved in chloroform and displayed mobilities $<10^{-4}$ cm^2/Vs[18]. The most recent improvement in P3HT mobility comes from the use of a solvent generated self-assembled monolayer (SAM), increasing the mobility of FET devices up to 0.12 cm^2/Vs. (It is important to note that the development of SAMs have allowed for increased mobilities in many systems other than P3HT.) This family of polymers have benefited from extensive synthesis work in systematically varying the chemical composition[58].

1.4 Organic Electronic Devices

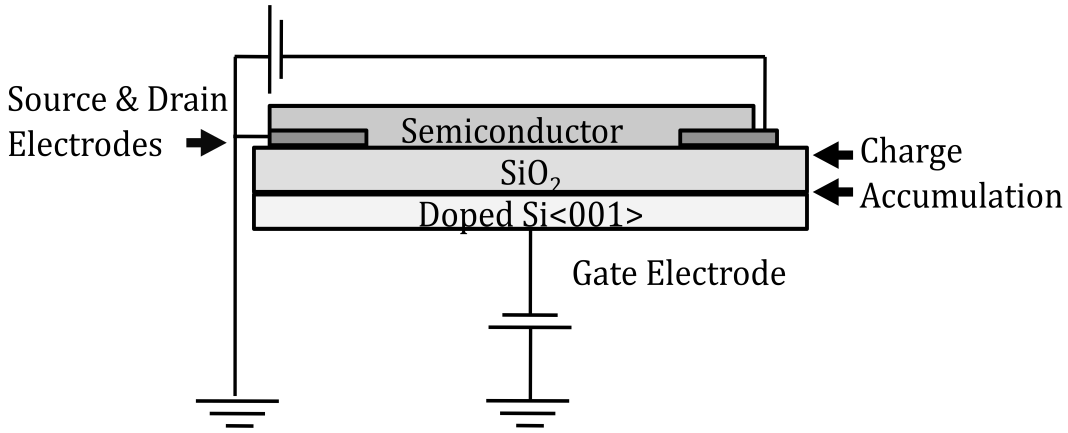

Figure 1.7: Illustration of a thin film transistor and electrical configuration.

Most methods of evaluating charge carriers in organic semiconductors originate from the models used to understand transport in traditional inorganic semiconductors, beginning with the first transistor. The first functional transistor was developed at Bell Labs in 1947[59]. Since then, many different types of transistor have been developed. One of the most common types, a thin-film transistor, is illustrated in Figure 1.7. When voltage V_g is applied to the gate electrode, relative to the source and drain electrodes, charge accumulates on the borders of the oxide, similar to a capacitor. This accumulated charge in the semiconductor is responsible for conduction between the source and drain electrodes, assuming that the electric field generated by the source and drain electrodes does not greatly perturb the field across the insulator. When operating, charge will migrate between the source drain electrodes, and transport is typically modeled as occurring in energy bands, highly delocalized plane waves perturbed by a periodic potential, or through a hopping mechanism, localized charges migrating between sites.

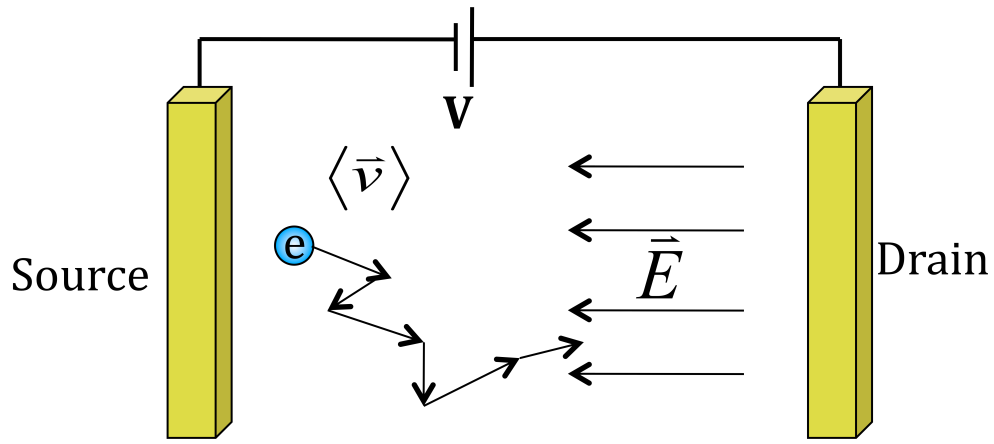

Figure 1.8: **Illustration of the Drude model.**

Despite the recent advances in organic semiconductors, the relationships between the macroscopic properties of morphology and device parameters and the microscopic dynamics of charge transport remain inadequate. One of the most broadly used measures of performance in transistor studies is the mobility, or the relative freedom of charge migration through the conduction channel when an electric field is applied. Relating transport through an organic material to a Drude-type model[60], the repeatedly scattered charge migration illustrated in Figure 1.8 can model the functioning of a device similar to that of Figure 1.7. Assuming a charge carrier exists in a conductor placed between two electrodes, the charge carrier will experience a force proportional to the electric field $\vec{E}$ that is established when a voltage is applied between the two electrodes. Given no scattering sites, conduction channel imperfections or scattering sites, a charge will accelerate with only the length of the conduction channel and the relativistic effects inhibiting the magnitude of the velocity. However, in real materials scattering and trapping sites as well as very high resistive areas (grain boundaries) do exist, creating a path of motion similar to a biased random walk[61], as seen in Figure 1.8. This biased random walk can be

averaged over, resulting in an average speed $\vec{v}$ through the material or an average time τ between charge scatterings/trappings/collisions. Therefore, motion through the material can be modeled as:

$$m_e \cdot \left(\partial \vec{v} / \partial t\right) = e\vec{E} - m_e \cdot \left(\vec{v} / \tau\right) \qquad \text{Eq. 1.1}$$

where m_e is the mass of the charge and e is the effective charge of the material. Since this model assumes a steady-state configuration, the velocity is constant, and we can solve Eq. 1.1:

$$e\vec{E} = m_e \cdot \left(\vec{v} / \tau\right) \rightarrow \left(e\tau / m_e\right) = \left(\vec{v} / \vec{E}\right) \qquad \text{Eq. 1.2}$$

Over an arbitrary time t, a charge Q consisting of an effect number of charge carrier n will have been transported from one electrode to the other over the channel length L. Since the measured parameter is current, we can consider the total current traversing the conduction channel j (dropping vector notation for simplicity):

$$j = \sigma E = n \cdot e \cdot \left(v\right) \rightarrow \sigma = n \cdot e \cdot \left(v / E\right) \qquad \text{Eq. 1.3}$$

Relating the induced carrier velocity v per electric field E to the conductivity σ, or Eq. 1.3 to Eq. 1.2, we observe that

$$\sigma = n \cdot e \cdot \left(v / E\right) \rightarrow \sigma = n \cdot e \cdot \left(e\tau / m_e\right) \rightarrow \sigma = n \cdot e \cdot \left(\mu\right) \qquad \text{Eq. 1.4}$$

where we have *defined* the term in parentheses to be the mobility μ. From Eq. 1.4, it can be seen that the mobility of the charge carriers is proportional to the charge carriers' drift velocity. Phenomena that cause an increase in the time necessary for charge carriers to traverse the conduction channel will decrease mobility. This includes charge scattering from phonons, trapped charges, and impurities. It is common to attribute the variability of charge carrier mobility induced by scattering to the average scattering time τ. If charges must tunnel across regions with low

conductance, which occurs in charge hopping, mobility will decrease proportionally to a tunneling time constant. Correspondingly, due to decreased hopping between polymer chains, more highly ordered polymers display a higher mobility than more disordered polymers or even oligomers[8, 25, 62]. Since the mobility can be lowered if charges become effectively immobile due to energetically deep traps with capture lifetimes on the order of the measurement time, the mobility is in effect a measure of all charge interactions.

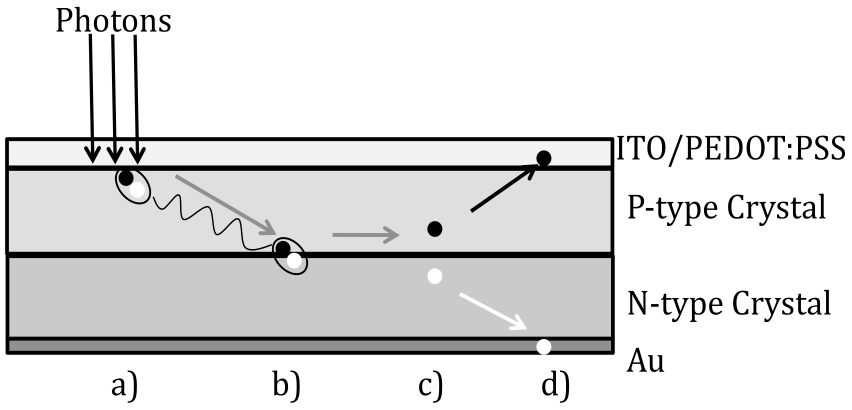

Figure 1.9: Illustration of photovoltaic dynamics in a bilayer crystal: photo absorption (a), exciton diffusion to the heterojunction (b), exciton dissociation (c), and charge transport to the electrodes (d).

Many of the fundamental processes concerning electronic mobility are also important in addressing problems in organic photovoltaics. Although much progress has been made in developing organic photovoltaics, the current record for efficiency is still only ~5%[12, 63-65]. The fundamental issues can be understood using the generic bilayer organic photovoltaic device, as shown in Figure 1.9. Light passes through a transparent electrode, generating excitons (electron-hole pairs), which ideally separate and migrate to opposite electrodes, generating a voltage. To increase the efficiency of organic photovoltaics, many groups have sought to improve the key physical processes dictating efficiency: photo absorption (a), exciton diffusion to the

heterojunction (b), exciton dissociation (c), and charge transport to the electrodes (d). A common example of how the issues of organic photovoltaics and transistors are related can be seen in many groups' attempts to increase the area of the heterojunction interface to increase the rate of exciton dissociation. Unfortunately, such increases usually generate more grain boundaries, current crowding, and trapping sites, complicating understanding of the charge migration mechanisms[64]. Therefore, the effects of polycrystalline materials must be understood before the limitation of the intrinsic interfacial processes are to be realized[64].

Much attention has been given to controlling device performance with surface treatments[66, 67] and charge, or chemical, doping in organic systems[68, 69]. Charge doping is the controlled introduction of donors and acceptors into or adjacent to the active conduction channel. It has been shown that dopants can alter electronic energy levels in productive ways, such as increasing conductivity and altering energy level alignments, thereby increasing charge injection, mobility and device performance[69]. Doping of organic semiconductors with long chain organic molecules also shows promise for enhancing the stability of organic devices[13, 68]. Although many p-type dopants such as DDQ and TCNQ have successfully been used a similarly broad array of n-type organic dopants, such as decamethylcobaltocene, remains underdeveloped but an active area of development in recent years[68, 69]. This increased conductivity has also been shown to increase exciton migration in solar cells and charge separation in both transistors and solar devices[68].

The most common measure of performance for a semiconductor is the mobility, which is most often generated from FET measurements, as outlined above.

Although a practical measure of charge conduction, it is highly interface and device specific since it is a net, holistic measure of transport. In Figure 1.8 the semiconducting material is illustrated as a continuous domain, similar to that of a single crystal, but most commercial large area devices have a polycrystalline conduction channel. Polycrystalline materials typically display lower mobilities, although notable new polycrystalline material materials display a mobility less than a factor of 10 smaller than the single crystal material[70]. This drop in measured performance is typically attributed to grain boundaries, decreased crystalline order in the smaller crystallites, and impurities or imperfections between grains[71, 72]. Therefore, to properly understand the intrinsic properties and limitations of organic semiconductors, surface effects of these materials must be properly understood.

1.5 Device Fabrication and Measurement

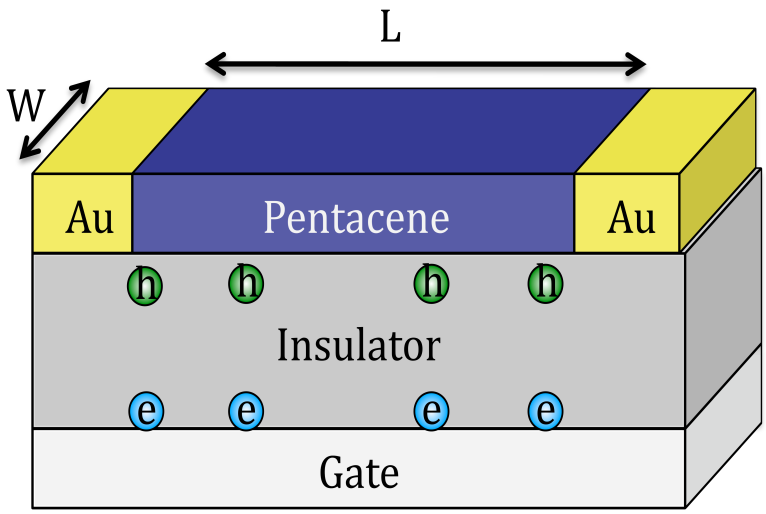

Figure 1.10: Illustration of an organic field effect transistor.

The most common method of measuring the in-plane mobility is through FETs, functionally similar in design to Figure 1.10. The FET is a three terminal device, with electrodes designated drain, source, and gate, operating effectively as variable current limiters. Patented in 1925 by Julius Lilienfeld, the first operational FETs were made by Pearson and Shockley and reported in 1948[73]. This postdates the first functional transistor, a point contact transistor, which was developed the year before by Bardeen and Brittain[74]. Due to their important contribution to electronics and the development of computers, these discoveries resulted in Bardeen, Brattain, and Shockley receiving the Nobel Prize for physics in 1956.

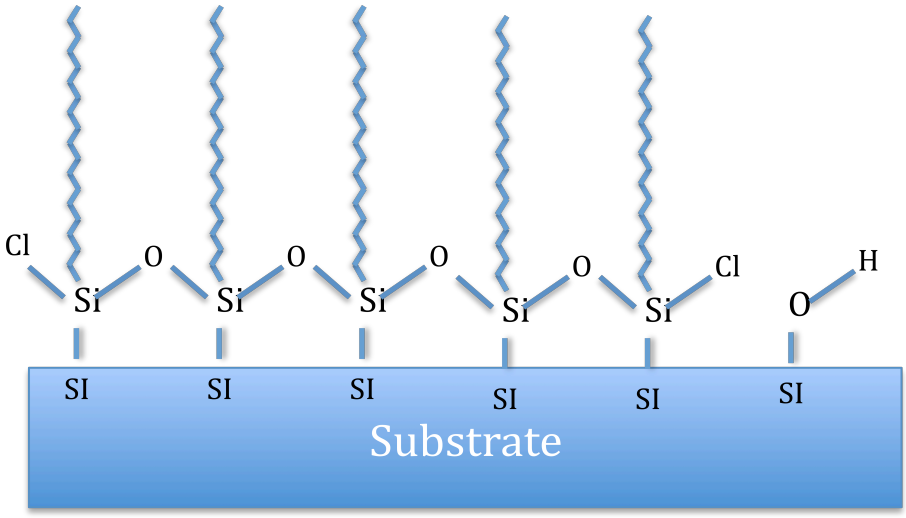

Figure 1.11 Illustration of OTS on an SiO_2 substrate[75].

Transistor current-voltage (IV) characteristics for FETs made of traditional materials are relatively well understood and will be the basis for understanding organic FET (OFET) IV characteristics[76, 77]. Therefore at least a cursory review of FET operation is necessary to properly understand OFET transport characteristics. Of the two most common device configurations for organic test structures, bottom and top contact inverted OFETs, only the top contact structure will be discussed in this dissertation. Typically heavily doped silicon <001> wafers with a thermally grown oxide layer are used as the gate and dielectric layers respectively. The oxide surface, including its morphology and dielectric properties, is extremely important for determining the electrical properties of fabricated devices since the conduction channel and electrical contacts are typically in intimate contact with the oxide. A recent development aimed at controlling this interface is the modification of the oxide surface using self assembled monolayers (SAMs)[78, 79]. SAMs bind to the insulator surface, acting as a buffer between the native oxide and the active areas of the device, as seen in Figure 1.11. It was initially found that modifying the growth

surface of small molecule organic semiconductors with SAMs, specifically octadecyltrichlorosilane (OTS), increased the field effect mobility in both pentacene[78] and tetracene[79]. This improved mobility was found to be due to improved conduction channel crystallinity and the establishment of electric dipoles at the SAM interface, effectively injecting charge into the surface of the conduction channel[66, 67, 80]. This technique has been successfully used to achieve the highest measured mobilities to date in such materials as poly(3-hexylthiophene)[80], fluorinated 5,11-bis(triethylsilylethynyl) anthradithiophene (diF-TES ADT)[70], and pentacene[81].

For top contact devices, the organic semiconductor can be applied to the dielectric surface (treated or untreated) using several very different methods depending on the physical properties of the material. For organic materials that are soluble in common solvents such as chloroform, spin coating, drop-casting and ink jet printing are feasible[82]. For materials that are not easily soluble, such as pentacene, vacuum evaporation is the most common for laboratory research. When it is advantageous to grow the semiconductor on another surface, for such reasons as improved cystallinity or surface incompatibility with the deposition method, it is often possible to transfer materials from one surface to another using transfer printing[83]. Transfer printing is the transfer of material from one surface to another due to the difference in adhesion energies of the surfaces involved, usually involving increased pressure and temperature to mediate the process. Transfer printing is a commonly used method, especially with carbon allotropes, due to their often complex fabrication and cleaning procedures[51]. Since the growth techniques of single

crystals of small organic molecules are not compatible with solution-based processes or flexible substrates, excluding a few notable exceptions[4, 70], most single crystal devices are fabricated using electrostatic adhesion or tranfer printing[12, 28, 83-86]. Independent of the semiconductor deposition method, the conduction channel is typically limited to a thickness d <50nm and moderate electrical characterization voltages (<60V) are applied inhibit electrical breakdown of the insulator[87]. To complete the top contact device, source and drain electrodes forming a conduction channel of length L and width W, shown in Figure 1.10, are deposited on top of the semiconducting material. The conduction width W is the distance between the source and drain electrodes while the conduction channel length L is the extent of the electrode perpendicular to the width W and the conduction channel thickness d. These physical parameters, and other properties of the electrodes, are important for interpreting electrical measurements of the transistor. As an example, non-ohmic contacts and semiconductor/electrode contact resistances can dramatically alter the measured device parameters[88].

Electrical characterization, specifically current-voltage (IV) measurements, on OFETs is often conducted in a benign dry nitrogen enviroment to extract the common device relevant parameters: linear μ_L and saturation mobilities μ_S, on-off ratio, threshold voltage V_{TH}, and subthreshold slope S. When a gate voltage V_G larger than a voltage V_{TH} is applied to the device, it is considered in the 'on' state and appreciable current I_D will flow between the source and drain electrodes when a source-drain voltage V_{SD} is applied. When $V_G<V_{TH}$, relatively little current (subthreshold leakage) will flow between the source and drain electrodes. In the on

state specifically, $I_D = V_{SD}/R$ where R is the channel resistance. We can relate the conductance, or one over the resistance, to the following[87]:

$$1/R = (W/L)\mu|Q| \qquad \text{Eq. 1.5}$$

where $|Q|$ is the total charge per area induced in the conduction channel due to the applied gate voltage. It is assumed that no charge trapping in either the dielectric or the semiconductor is occurring. It is now possible to write Eq. 1.5 as

$$I_D/V_{SD} = \left(\frac{W}{L}\right)\mu|Q|.$$

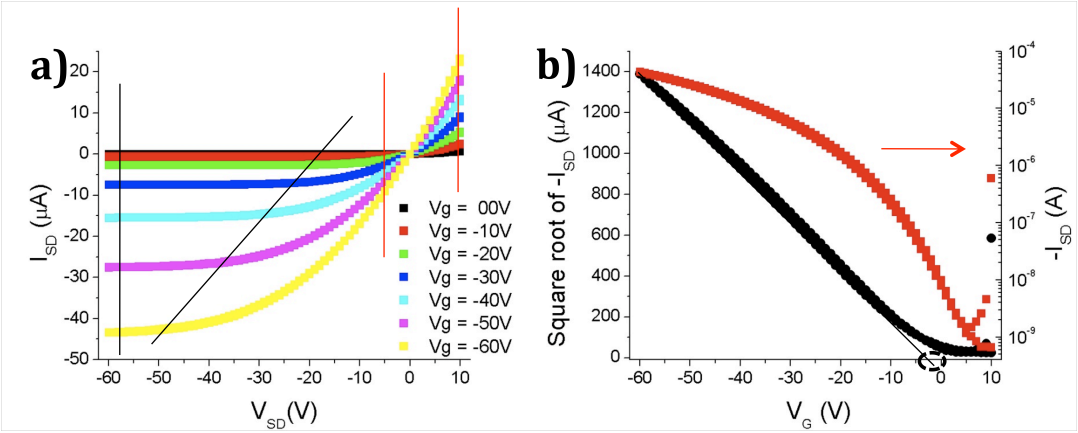

Figure 1.12: **a) Current as a function of voltage for a pentacene transistor at various gate voltages. Solid red lines indicate the linear regime while solid black lines indicate the saturation regime. b) A linear plot (black) of the square root of source-drain current and a semi-log plot (red) of source-drain current as a function of gate voltage for a pentacene device at V_{SD}=5V. A black line is a fit to the linear plot or the source drainc current over the range -60V to -40V and is extrapolated to zero gate voltage. A black circle highlights the zero source drain voltage.**

The total amount of induced charge is known for this parallel plate capacitor-type configuration and given by:

$$|Q| = CV_{effective} = C(V_G - V_{TH} - V_{SD}/2) \qquad \text{Eq. 1.6}$$

where $V_{effective}$ takes into consideration the threshold voltage V_{TH} and the charge distribution between the two electrodes, or across the device length L. Using Eq. 1.6, the drain current can then be written as

$$I_D = (W/L)\mu C V_{SD}(V_G - V_{TH} - V_{SD}/2) \qquad \text{Eq. 1.7}$$

For small $V_{SD}<<(V_G-V_{TH})$, we drop the second order V_{SD} term to arrive at:

$$I_D = \left(\frac{W}{L}\right)\mu C V_{SD}(V_G - V_{TH}) \qquad \text{Eq. 1.8}$$

In the on state, it is common to define two regimes of operation, linear and saturation. In the linear regime, when $V_{SD} << (V_G-V_{TH})$, there is a linear dependence of source-drain current on source drain voltage. This regime is illustrated as the region between the red lines in Figure 1.12. In this regime, the source-drain current I_{SD} can be modeled as having the form:

$$I_{SD} = \frac{W}{L}\mu C(V_G - V_{TH}) \cdot V_{SD} \qquad \text{Eq. 1.9}$$

where C is the capacitance per unit area of the device geometry. The assumptions in this equation include relatively small V_{SD}, uniform electric field E in the conduction channel, negligible trapping sites, no current crowding, and no charge injection barrier. If $V_G<V_{TH}$ is maintained, leaving the device in the on state, but $V_{SD} \geq (V_G-V_{TH})$ then the device is considered to be in the saturation regime. In this case, the accumulated charge variation along the dielectric layer must be taken into account. A depletion region forms at the drain (or source) electrode, sometimes called the pinch-off or space charge region[87]. In this regime, it is found that the source-drain current I_D is saturated, or independent of applied source-drain voltage. It is observed that the source-drain current I_D behaves as:

$$I_D = \left(\frac{W}{2L}\right)\mu C\left(V_G - V_{TH}\right)^2 \qquad \text{Eq. 1.10}$$

as is illustrated by the flat regions between the black lines in Figure 1.12a.

By measuring the IV characteristics of these devices, it is possible to measure the relevant device parameters mentioned earlier in this chapter. The most common measure of performance is the field effect mobility μ. It is possible to extract and common to quote this value in both the linear and saturation regimes. For $V_{SD} << (V_G - V_{TH})$, we examine the IV curves seen in Figure 1.12a. Beginning with Eq. 1.09, we take the derivative with respect the gate voltage V_G to arrive at:

$$\frac{\partial I_{SD}}{\partial V_G} = \frac{W}{L}\mu_L C\left(V_{SD}\right) \qquad \text{Eq. 1.11}$$

where $\partial I_{SD}/\partial V_G$ is commonly referred to as the transconductance *g*. Note that this is only valid for relatively small V_{SD}. Solving for the linear mobility, we arrive at

$$\mu_L = \frac{g \cdot L}{CW}\left(\frac{1}{V_{SD}}\right) \qquad \text{Eq. 1.12}$$

In practical terms, the transconductance g is proportional to the slope of the red curve in Figure 1.12b for source-drain voltages smaller than the gate voltage. For measurements of both the linear and saturation mobilities, the data are not continuous. Therefore, a specific region of data can be quoted along with the given mobility measurement.

For fixed source-drain voltage, the on-off ratio and subthreshold slope can be determined from measurements of the drain-current I_D as a function of gate voltage V_G, as seen in Figure 1.12b. The on-off ratio is the ratio of the on state maximum current to the off state leakage current, specifically $\sim 10^5$ for the red curve in Figure

1.12b. The subthreshold swing, S, is defined as the change in voltage required to induce a factor of 10 increase in the source-drain current I_D, or specifically,

$$S = \frac{\partial V_G}{\partial(\log_{10} I_D)} \qquad \text{Eq. 1.13}$$

Change in subthreshold slope S is often correlated with dielectric interface morphology and molecular ordering at conduction channel/dielectric interface[79]. The saturation mobility can be determined when $V_{SD} > (V_G - V_{TH})$ and $V_G < V_{TH}$ for a fixed source-drain voltage V_{SD}, with the common source-drain voltages quoted in the literature being -10 and -40 volts. Beginning with the expression for the source-drain current I_D in the saturation regime, specifically Eq. 1.11, taking the square root:

$$\sqrt{I_D} = (V_G - V_{TH})\sqrt{\left(\frac{CW}{2L}\right)\mu_S} \qquad \text{Eq. 1.14}$$

and a derivative with respect to the gate voltage V_G, assuming the mobility is independent of V_G:

$$\frac{\partial\left(\sqrt{I_D}\right)}{\partial V_G} = \sqrt{\left(\frac{CW}{2L}\right)\mu_S} \qquad \text{Eq. 1.15}$$

yields:

$$\mu_s = \left(\frac{2L}{CW}\right)\left(\frac{\partial\left(\sqrt{I_D}\right)}{\partial V_G}\right)^2 . \qquad \text{Eq. 1.16}$$

It is common to call this measurement of mobility the field effect mobility μ_{FE}. It is common to examine saturation IV curves as the square root of source-drain current I_D versus gate voltage V_G, as seen in Figure 1.12b. Practically, the linear portion of the figure is fit over some region of voltage and the slope is used to calcuate the saturation mobility μ_S. For a given source-drain voltage, the linear relationship of the

square root of source-drain current I_D versus gate voltage V_G can be extrapolated to zero source-drain current I_D, as is shown by the black line in Figure 1.12b. The voltage at which the extrapolated line goes to zero is defined to be the threshold voltage V_{TH}, as is indicated by the black line and circle in Figure 1.12b. It is a coarse measurement of the voltage at which the device begins to operate as a transistor.

Electrical characterization of devices is mediated by electrodes, and since they are completely responsible for charge injection and ejection it is thought that they are one of the most significant influences on device performance[89, 90]. Proper contact characterization remains an active area of research because of the difficulties associated with measuring buried interfaces. The interfaces typically have poorly measured morphology and largely unknown changes occurring to the organic surface during electrode deposition, which inhibit formulations of charge injection theories. Many different models have been proposed to explain the contact induced performance limitations[91-93], with the consensus being that charge injection can be described as a two step process including both thermionic emission and tunneling, with a host of physical considerations modifying transport[94]. These physical considerations help to determine the energy barrier that charges must overcome when crossing the interface[95, 96], which is the most important factor controlling charge injection[87, 94]. Specifically with pentacene, it has been shown that top and bottom contact devices yield different injection barriers, even with varying metals[97, 98], with part of the explanation being the creation of trap charges in top-contact devices[59, 99, 100]. In general, controlling the magnitude of the barrier through suitable matching of the source-drain electrode metals with the Fermi level of the

organic semiconductor is the most common method of establishing efficient charge injection[79] yet is it possible for dipole layers to form, increasing the charge barrier[89, 101, 102].

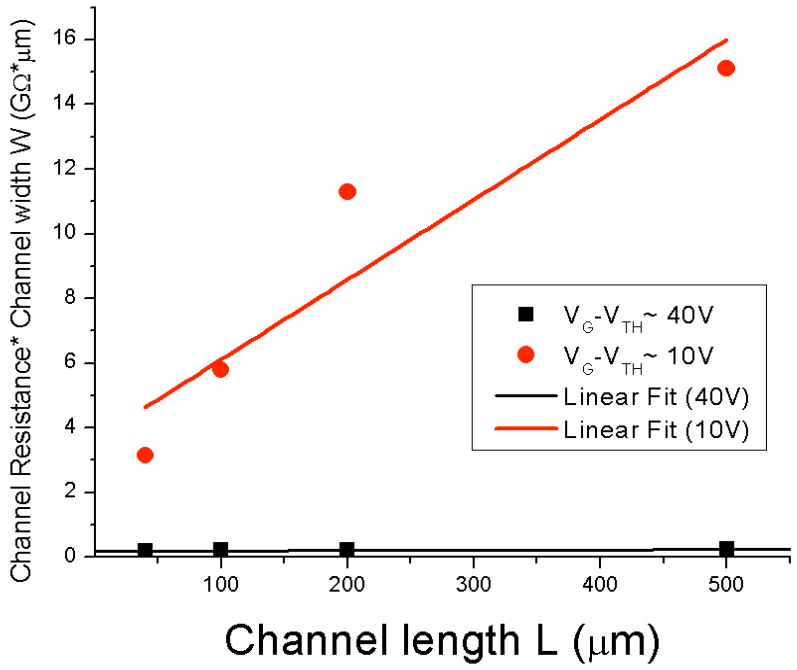

Figure 1.13: **A pentacene device's channel width times the resistance of the device width plotted versus the channel length L, as per Eq. 1.19.**

A relatively simple measure of the quality of the contacts, and therefore the charge injection is the contact resistance. Contact resistance is, coarsely, the barrier experienced by charges entering and leaving a device. The magnitude of the effect on transport properties depends on the relative sizes of the contact and series resistances, R_C and R_S respectively. Ideally measured by four point probes or transmission line measurements[103], contact resistances can also be extracted from two probe, DC IV measurements. First introduced to the organics literature by the Katz group[104], the

finite voltage drop across the gate-source and drain-source electrodes can be taken into account, in Eqs. 1.9 and 1.10, resulting in:

$$I_{SD} = \frac{W}{L}\mu C\left((V_G - I_D R_S) - V_{TH}\right)\cdot\left(V_{SD} - I_D R_s - I_D R_C\right) \qquad \text{Eq. 1.17}$$

$$I_D = \left(\frac{W}{2L}\right)\mu C\left((V_G - I_D R_S) - V_{TH}\right)^2 . \qquad \text{Eq. 1.18}$$

where V_G-$I_D R_S$ is the effective gate voltage and V_{DS}-$I_D R_S$-$I_D R_D$ is the effective source drain voltage[87]. The result is a smaller effective gate and source-drain voltage, thus lower transport characteristics that become exceedingly evident for small V_{SD} and V_G. The device resistance, the total measured resistance, for small source-drain voltage V_{SD} is the sum of the channel resistance R_{CH}, contact resistance R_C, and series resistance R_S:

$$R_{Device} = R_{CH} + R_C + R_S = V_{SD}\cdot\frac{L}{W}\frac{1}{V_{SD} C\mu\left(V_G - V_{TH}\right)} + R_C + R_S \qquad \text{Eq. 1.19}$$

where Eq. 1.9 was used in conjunction with Ohms law. Therefore, if the quantity $W \cdot R_{Device}$ is plotted versus the channel length L for various effective voltages (V_G-V_{TH}), a plot such as Figure 1.13 can be generated. If Eq. 1.18 (or more simply slope*length + (R_C+R_S)*width) is fit to data with similar gate voltages V_G-V_{TH}, the resistance at zero channel length L is the total parasitic resistance $R_{Parasitic} = R_S + R_C$. This resistance can then be accounted for and used to correct measurements of the mobility[87].

1.6 Scanning Probe Microscopy

The invention of Scanning Probe Microscopes (SPMs), specifically the scanning tunneling microscope (STM) and atomic force microscope (AFM), have

allowed the realization of Richard Feynman's 1959 talk at the annual APS meeting entitled, "Plenty of Room at the Bottom," continuing in ways Feynman could never have anticipated[105]. Understanding the relationships between the structure and function of surfaces and solids has been a very active area of research for the better part of the last century. The Nobel Prize was awarded in 1937 to Davisson and Thompson for their "experimental discovery of diffraction of electrons by crystals," a precursor to low energy electron diffraction (LEED)[106]. The Nobel Prize in chemistry was given in 1918 to Fritz Haber for his development of the Haber-Bosch process, which allowed the commercial development of ammonia through the use of iron catalysts on surfaces. Although ammonia synthesis was heavily used almost immediately after discovery, this process was poorly understood until the extensive studies of the 2007 chemistry Nobel Prize winner Gerhard Ertl[107-113]. Ertl went on to study many chemical reactions on surfaces, such as carbon monoxide formation on platinum[114-116], using many surface science techniques, such as LEED[114, 117] and STM[118, 119]. These works helped to establish the field of surface science and highlight the importance of studying surfaces.

The first scanning probe microscope was developed by Binnig and Rohrer in 1982 while working at IBM Zurich Research Laboratory[120]. This discovery immediately led to atomic resolution images of Si(111)-(7x7)[121] determining the real-space reconstruction, explained by the dimer-adatom-fault stacking model[122, 123]. This was a topic of heated debate due to the complex nature of inferring a 49-atom unit-cell distributed over 4 atomic layers from reciprocal space information[124-126]. Soon after this confirmation of the power of STM, both

homemade and commercial STM became quite common in surface science laboratories. Some claim that STM is now a vital component for any surface science laboratory, just as LEED had become earlier in the development of surface science[127].

Scanning tunneling microscopy is based on the quantum mechanical property of tunneling. In the most basic sense a sharp metallic object is brought close to a conducting material, a voltage is applied between the sharp tip and conducting object, and as the tip moves across the surface measurements of current are converted into topography. The bias-induced current is the result of electrons tunneling across the insulating space between the two conductors. More specifically, we can consider this to be physically equivalent to the 1D case of an electron encountering a potential barrier. The solutions for such a problem are well known[128]. For a finite square barrier of thickness t, barrier height V_o, and a voltage V applied across the barrier, the transmission of electrons across the barrier will result in a current:

$$I \propto \left(\frac{V}{t}\right)\exp\left(-a \cdot t \cdot \left(V_o\right)^{1/2}\right) \qquad \text{Eq. 1.20}$$

where *a* is a constant for a given particle type. Since the barrier height Vo is several eV and a typical value of the constant *a* is ~1 $nm^{-1}ev^{-1/2}$, the typical decay length is ~5-7 Å. Therefore, for a given tunneling situation, small changes in the barrier thickness and height result in large changes to the tunneling current.

In order to understand the operation of STM on a useful level, a more accurate modeling of the 3D tunneling current is required. The most commonly used theoretical model was developed by Bardeen in 1960[129]. Instead of solving the full 3D Schrödinger equation, Bardeen proposed using time-dependent perturbation

theory to solve for the overlap of the wavefunctions of two free systems, separated by an insulator, using Fermi's golden rule[128]. Specifically, Bardeen proposed that for two free systems the tunneling matrix element M for the transition between the two states would be given by the integral over the area *A* separated by a distance *d*

$$M_{ab} = \frac{\hbar}{2m}\int_{z=d}\left(\psi_a^*\nabla\psi_b - \psi_b\nabla\psi_a^*\right)\cdot dA \qquad \text{Eq. 1.21}$$

where $\hbar$ is Planck's constant divided by 2π and m is the mass of the electron[129]. The probability of tunneling between the free states *a* and *b*, can be solved via Fermi's golden (second) rule:

$$w_{a\to b} = \int dE_b\left(\frac{2\pi}{\hbar}\right)\left|M_{ab}\right|^2\delta\left(E_b - E_a\right)\rho\left(E_b\right) \qquad \text{Eq. 1.22}$$

where only states with the same energy are considered, specifically $\delta\left(E_b - E_a\right)$[130, 131]. Summing over all states, with a voltage V applied between the states:

$$I = \frac{4\pi}{\hbar}\int_{-\infty}^{\infty}\left[f\left(E_F - eV + \varepsilon\right) - f\left(E_F + \varepsilon\right)\right]\times \\ \rho_a\left(E_F - eV + \varepsilon\right)\rho_b\left(E_F + \varepsilon\right)\left|M_{ab}\right|^2 d\varepsilon \qquad \text{Eq. 1.23}$$

where f(E) is the Fermi distribution and $\rho_{a,b}\left(E\right)$ is the density of state for materials 'a' and 'b', respectively[130]. If the Fermi level is approximated as a step-function, and the tunneling matrix M is constant over the energy interval[132], we arrive at:

$$I \propto \int_o^{eV}\rho_a\left(E_F - eV + \varepsilon\right)\rho_b\left(E_F + \varepsilon\right)d\varepsilon \qquad \text{Eq. 1.24}$$

which indicate that both states contribute equally and symmetrically to the total current. Essentially, tip scanning is a convolution of the tip density of states and the sample density of states. For small voltages, the current is merely proportional to the

tip and sample density of states convolution at the point of measurement times the voltage applied:

$$I \propto V\rho_{sample}(E_F,\vec{r})\rho_b(E_F) \qquad \text{Eq. 1.25}$$

Thus, the measured current is not just topography, it is topography convoluted with the sample's local density of states. If the STM tip is metal, and therefore has free electrons, the local density of states can be measured by fixing relative tip-sample separation and measuring current as a function of voltage. When the tip is biased negatively relative to the sample, electrons will tunnel from the tip to empty surface states. Positive biasing will move electrons from the filled electronic states of the sample to the tip. Measuring the current as a function of tunneling-bias is called scanning tunneling spectroscopy.

For the STM work presented in this dissertation, all scanning was carried out in a constant-current mode. Constant-current mode uses a three-parameter feedback loop to maintain the tunneling current at a fixed value. Specifically the parameters are tunneling current, proportional gain, and integral gain. Tunneling current sets the equilibrium point, or desired stable current, for a given sample bias voltage. Proportional gain adjusts the tip-sample separation as a direct function of the current at that moment, $I = K_I d_{t-s}(t=0)$. Integral gain adjusts the tip-sample separation as a function of the current over some time interval t_o, $I = \int_o^{t_o} dt \mathrm{K}_I d_{t-s}(t)$. A common concern when imaging non-metal surfaces is the actual tip-to-sample distance since the feed back loop controls current only. When imaging oxide materials an increased tunneling barrier is encountered, effectively lowering the STM tip for a fixed current value. Therefore, if the topography of the surface is comparable to the tip-to-sample

separation or large organic molecules are being measured, such as pentacene, maintaining a large enough bias voltage is vital to inhibit tip-sample physical contact.

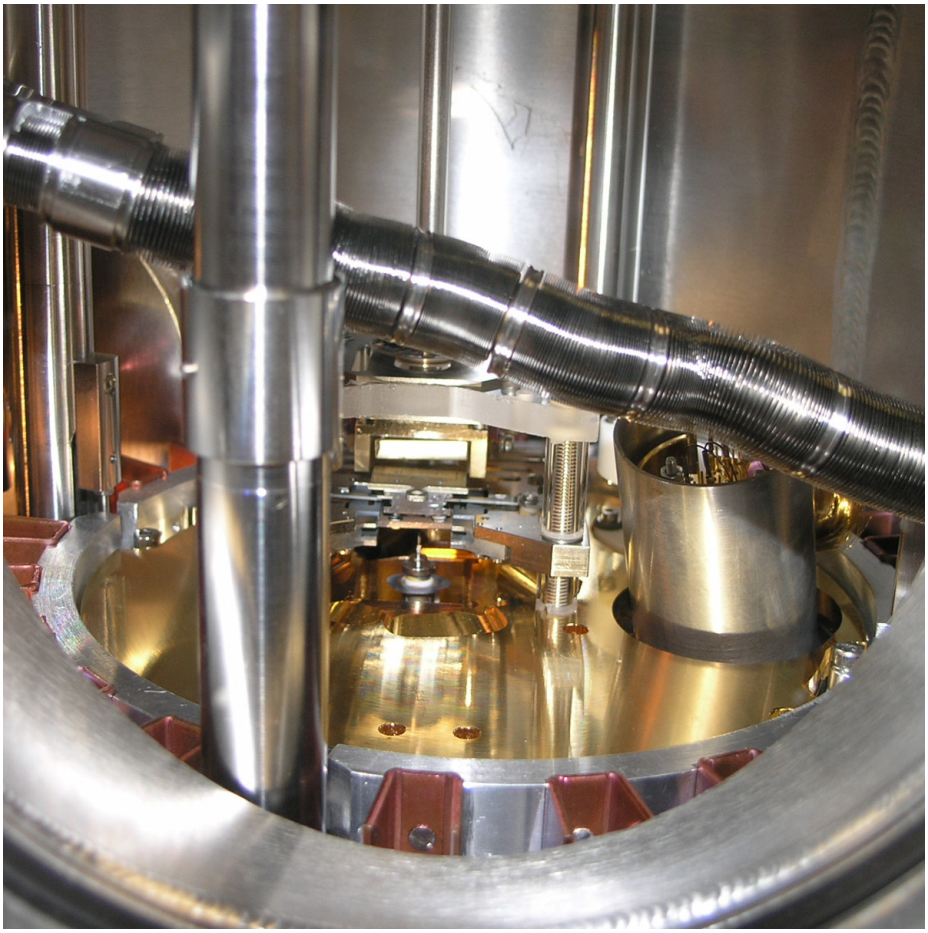

Figure 1.14: Photograph of the Omicron-VT STM.

A commercial Omicron-VT STM, as seen in Figure 1.14, was used for some studies in this dissertation. All STM measurements occured under ultra-high vacuum (UHV) conditions, with pressures typically $< 5 \times 10^{-11}$ torr, allowing for samples to remain clean ~10^5 seconds. Typical tunneling currents ranged from 30pA up to 10nA for brief periods. However, since organic overlayers on metal or thin oxide surfaces are known to be less robust than metal or semiconductor surfaces[133] to avoid current induced chemical modification[134], imaging currents were kept at <200pA.

Chapter 2: Nanoscale Fluctuations*

Spatial step edge fluctuations on a multi-component surface of Al/Si(111)-($\sqrt{3} \times \sqrt{3}$) were measured via scanning tunneling microscopy over a temperature range of 720K-1070K, for step lengths of L = 65-160 nm. Even though the time scale of fluctuations of steps on this surface varies by orders of magnitude over the indicated temperature ranges, measured first-passage spatial persistence and survival probabilities are temperature independent. The power law functional form for spatial persistence probabilities is confirmed and the symmetric spatial persistence exponent is measured to be $\theta = 0.498 \pm 0.062$ in agreement with the theoretical prediction $\theta = ½$. The survival probability is found to scale directly with y/L, where y is the distance along the step edge. The functional form of the survival probabilities agree quantitatively with the theoretical prediction, which yields an exponential decay in the limit of small y/L. The decay constant is found experimentally to be $y_s/L = 0.076 \pm 0.033$ for $y/L \leq 0.2$.

* This chapter is adapted from: Spatial first-passage statistics of Al/Si(111)-($\sqrt{3} \times \sqrt{3}$) step fluctuations, B. R. Conrad, W. G. Cullen, D. B. Dougherty, I. Lyubinetsky, and E. D. Williams,Phys. Rev. E 75, 021603 (2007) doi:10.1103/PhysRevE.75.021603

2.1 Stochastic Processes: Persistence and Survival

Interest in nanoscale fluctuations stems from the drive to reduce the dimensions of electrical devices to a length scale that is comparable to defect fluctuation amplitudes. In crystalline solids, the boundaries of layered material, or monatomic step edges, are the dominant source/sink for atomic motion for the surfaces of crystalline solids[135-138]. In the regime where thermally activated atomic motion is allowed, the steps will change shape with time, or wander[139]. Traditionally, these step edge fluctuations have been examined using correlation function approaches. However additional information is available in the form of first-passage analyses[61, 140-142], which may be pertinent to applications in self-assembly and nanoscale device properties[143-146].

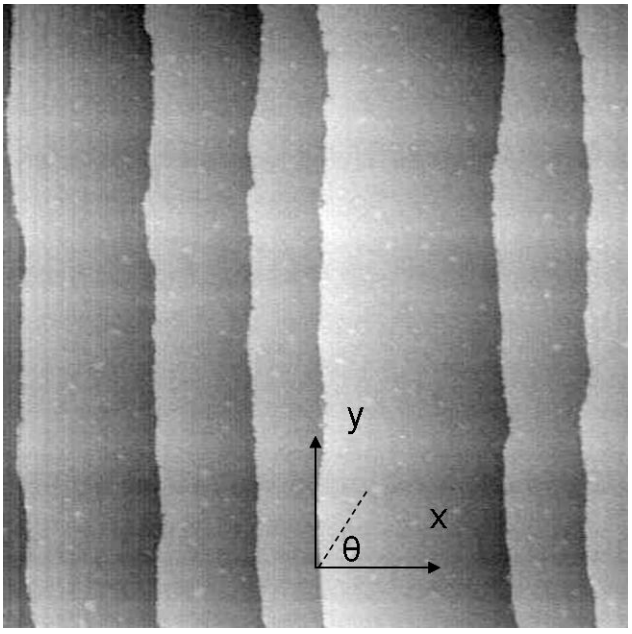

Figure 2.1: **STM image of continuous Al deposited on Si(111)-($\sqrt{3} \times \sqrt{3}$) at 720K. The lines present on the surface are the edges of terraces, or steps continued from the Si(111) substrate. A coordinate system with an origin on a step edge is displayed.**

As can be seen in Figure 1, the monatomic layer edges appear as lines in an STM image. These step edges can be seen to wander in an apparently random way

spatially as x(y), as observable in Figure 1, or by using consecutive temporal images of the same position[147]. Focusing on the random nature of the step wanderings, both Einstein[148] and Smoluchowski[149, 150] hypothesized that the motions of the pollen particles observed by R. Brown in 1828 were caused by the random thermal motions of surrounding molecules. A way to model this so called random motion was presented by Langevin, via the Langevin equations, in which the random motions of particles are incorporated into the equations of motion via a noise term[150]. A step edge is a discrete object in the x-direction but an extended object in the y-direction, that may be treated in a way analogous to Langevin's since the position of the step edge x(y) also moves randomly as a result of the random thermal motions of its constituent atoms.

As suggested above, it can be useful to calculate various quantities from the measured step edge position x(y). Traditionally, correlation functions have been used to quantify of thermodynamic properties such as step energy, step stiffness, and the kink energy[147, 151]. Statistically derived quantities have brought new insights in examining step fluctuations[152-164]. The idea of how far a fluctuation will persist along a step edge is particularly useful when device consisting on only a few atomic layers or even molecules are considered. Two quantities that measure fluctuation persistence have been defined, namely persistence and survival.

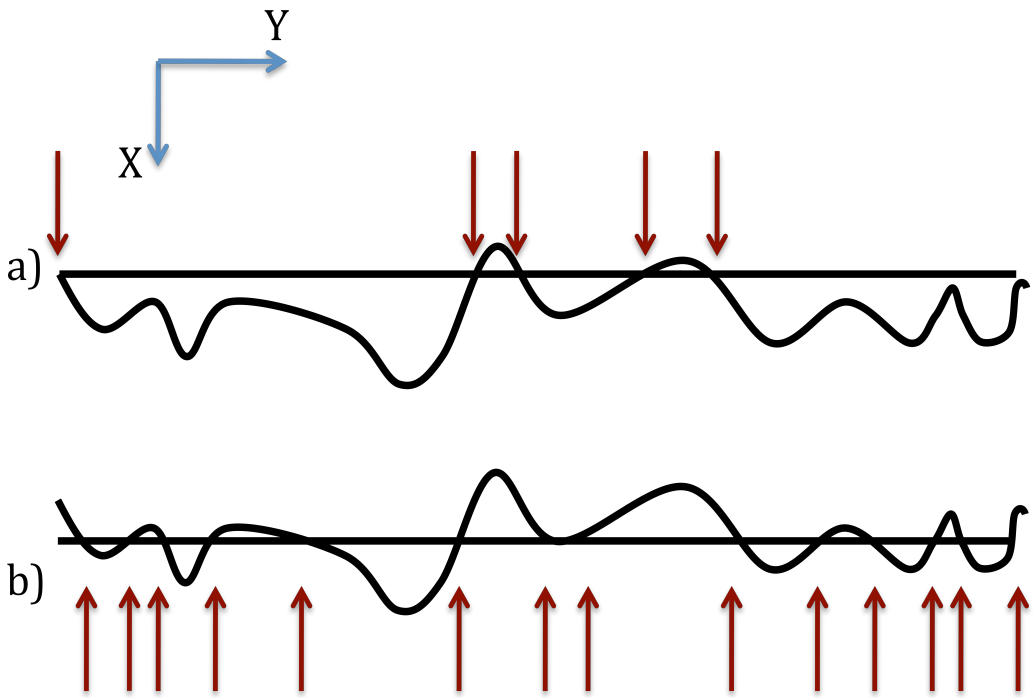

Figure 2.2: **a) Illustration of persistence. Note that the step must cross the initial value (t=0). b) Illustration of survival. Note that the line must cross the average.**

While first-passage problems are most often posed in terms of temporal fluctuations, spatial wandering is also an applicable problem. The distance that a fluctuation will persist along a step edge is particularly interesting as a measure of the stability of nanoscale structures[157, 163, 165]. Such information can be gained by examining spatial first passage statistics such as persistence and survival probabilities, P(y) and S(y), respectively. Persistence probability P(y) is the probability that a fluctuating step edge does not return to its initial position over a given distance, y, measured parallel to the average step edge, as illustrated for a meandering boundary in Figure 2.2a. A closely related quantity, survival probability S(y) is the probability that a fluctuating step edge does not cross its average position over a given distance y, as illustrated by a fluctuating boundary in Figure 2.2b. Formally, persistence and survival probabilities are defined as:

$$P_{ss}(y_o, y_o + y) \equiv \text{Prob}\left\{sign\left[x(y_o + y') - x(y_o)\right] = \text{constant}, \forall\ 0 \le y' \le y\right\} \qquad \text{Eq. 2.1}$$

$$S_{ss}(y_o, y_o + y) \equiv \text{Prob}\left\{sign\left[x(y_o + y') - \langle x \rangle\right] = \text{constant}, \forall\ 0 \le y' \le y\right\} \qquad \text{Eq. 2.2}$$

where x(y) is the displacement of the step, measured at a position y, from its average position. The brackets indicate an average over the length in question and it is assumed that steady-state conditions exist and no growth is occurring[157].

As is the case with many condensed matter systems, the number of degrees of freedom is too large to allow for an atomic treatment[151, 166]. The systems being dealt with here are composed of an effectively innumerable, but discrete, number of particles. Ergo, the general course of action is to treat this discrete problem in a continuous way, thereby making the problem manageable while maintaining an adequate edge description for discrete monatomic steps[147]. The most pertinent model that follows this course is the continuum step model, treating each step as a discrete, yet continuous, function x(y)[147]. Furthermore, it will be assumed that x(y) is stochastic, specifically that the fluctuations of the step edge are thermally induced and that the temperature of the system is well below the roughening-transition temperature of the terrace planes[139].In this fashion we can reduce the problem to a manageable level yet still answer fundamental questions of interest in a reasonable quantity of time.

It is well known that the Langevin formalism properly describes this type of a system[139, 147, 151, 161, 167]. As can be seen in Figure 2.1, for this treatment we shall use the “Maryland notation” [168]. In the formation of the step defined by x(y,t), there are two pertinent energies involved. The entropy increase due to the number of configurations available to the step and the energy required to create the

step will make up the free energy per unit length of step edge β[147, 166]. The step can be modeled by initially writing the free energy functional for an isolated, non-interacting step as[139, 151, 169-171]:

$$F\left[x(y,t)\right] = \int \beta(\theta) ds \qquad \text{Eq 2.3}$$

where ds is an infinitesimal length along the step edge and the step free energy β can possess angular dependence where the angle θ represents the angle of the step edge in relation to a specific direction in the plane of the surface. Noting Figure 2.1, the conventional definition for the angle θ is:

$$\frac{dy}{dx} = \tan\left(\frac{\pi}{2} - \theta\right) \qquad \text{Eq 2.4}$$

Using the Maryland convention and the above definition, we can write Eq. 2.1 as:

$$F\left[x(y,t)\right] = \int \beta(\theta) \sqrt{1 + \left(\frac{\partial x(t)}{\partial y}\right)^2}\, dy \qquad \text{Eq. 2.5}$$

By assuming only relatively small wanderings, e.g. dx/dy is small, and doing a Taylor expansion on both the step free energy β and the radical, we can safely write Eq. 2.5, keeping only terms to second order in dx/dy, as:

$$F\left[x(y,t)\right] = -F_o \int \frac{1}{2}\left[\beta\left(\frac{\pi}{2}\right) + \frac{\partial^2 \beta}{\partial \theta^2}\right]\left(\frac{\partial x(t)}{\partial y}\right)^2 dy \approx \int \frac{1}{2}\left[\tilde{\beta}\left(\frac{\pi}{2}\right)\right]\left(\frac{\partial x(t)}{\partial y}\right)^2 dy \qquad \text{Eq. 2.6}$$

where the term in square brackets is defined to be the step edge stiffness , or $\tilde{\beta}$ [151]. This approximation becomes more correct at higher temperatures since $\frac{\partial^2 \beta}{\partial \theta^2}$ approaches zero. As Jeong and Williams suggest, the Fourier transform of x(y,t) can be used to diagonalize the continuum step Hamiltonian, which has the same form as

Eq. 2.6, and evaluate the correlation functions. The spatial correlation function is defined by:

$$G(y) = \left\langle \left[x(y) - x(0) \right]^2 \right\rangle \qquad \text{Eq. 2.7}$$

where the brackets indicate an average over the entire ensemble. Using this equation, the spatial correlation function can be measured directly. If one assumes small y and computes the average of G(y), one arrives at:

$$G(y) \approx kT|y|/\tilde{\beta} \qquad \text{Eq. 2.8}$$

Ergo, the initial linear slope of G(y) gives the step edge stiffness for a given average system energy or temperature. It is important to note that by the very nature of using the Langevin equations, the above treatment is entirely continuous and thermodynamic.

Another method is to treat the step position as a discrete random walk problem in the dimension perpendicular to step edge progression[61]. Treatment of the step boundary via this model will not be presented here, but such an analysis links step diffusivity to a measurable quantity such as step edge stiffness and is an alternative conceptualization of G(y)[147]. This treatment can also lead to insightful descriptions of the mass transport on and near the step edge itself. Using the linear Langevin equations, it has been argued that the persistence exponent is related to the growth rate of the width of an interface and the dynamic universality class for the step edge model[147, 151, 155, 172, 173].

Dynamic universality classes are defined by exponential and power law exponents that describe the step edge's growth rate and roughness. If the RMS width of an interface of length L is given by:

$$w\left(L_y, y\right) = \sqrt{\frac{1}{L_y}\sum_{y_j=0}^{L_y}\left[x(y_j) - \bar{x}\right]^2} \qquad \text{Eq. 2.9}$$

then it is supposed that the width itself has a universal scaling form:

$$w\left(L_y, t\right) \sim L_y^{\alpha} u\left(t/L^{\alpha/\beta}\right) \text{ where } u(t/L^{\alpha/\beta}) \sim \begin{cases} t^{\beta}/L^{\alpha} & t << 1 \\ 1 & t >> 1 \end{cases} \qquad \text{Eq. 2.10}$$

Where 'u' is a general function dependent on time and the exponents 'α' and 'β', where 'α' and 'β' are the roughening and the growth exponents, respectively. These exponents define a *dynamic universality class* for the interface model[173].

There are other meaningful quantities one can calculate from the x(y,t) data, namely spatial persistence and survival probabilities[152-161, 163, 164, 172, 174-176]. Theoretical studies[145, 157] have shown that persistence probabilities have the general form of a power law decay for the step displacement not to return to its starting position over a distance y,

$$P(y) \sim y^{-\theta} \qquad \text{Eq. 2.11}$$

where θ is the persistence exponent [152, 165] characterizing the model universality class of the system. Fluctuations of step edges on Al/Si(111) display the time correlation function signature of a $t^{1/2}$ dependence at short times[177]. The most straightforward interpretation of this signature is that the fluctuations result from mass exchange randomly from all step-edge positions with the neighboring terraces. Alternative explanations[170, 178, 179] based on diffusion limited kinetics are rendered less tenable in this case by the experimental cross correlation signature[180] and the observation of temporal persistence behavior consistent with z = 2 [161]. If the observations are due to random mass exchange, these dynamics fall within the Edwards-Wilkinson model[151], which can be described by the equation

$$\frac{\partial x(y,t)}{\partial t} = \Gamma \frac{\partial^2 x(y,t)}{\partial y^2} + \eta(y,t) \qquad \text{Eq. 2.12}$$

where Γ is the mobility and η is a noise term. We only consider [181]

$$\langle \eta(x,t)\eta(x',t') \rangle = \delta(x - x')\delta(t - t') \qquad \text{Eq. 2.13}$$

which is uncorrelated Gaussian noise. It has been shown[163] that in the steady state configuration,

$$\begin{aligned} &\theta = 3/2 - n, \quad 1/2 < n < 3/2 \\ &\theta = 0, \qquad\quad n > 3/2 \end{aligned} \qquad \text{Eq. 2.14}$$

where n = (z – d + 1)/2. For this (1+1) dimensional interface, d = 1 and the dynamical exponent of the Edwards-Wilkinson model is z = 2. Therefore, we expect the persistence exponent θ = ½ [165]. In comparison with the persistence probability, the survival probability is related to the autocorrelation function and decays roughly exponentially with decay constants related to the correlation length[157].

The spatial correlation function, i.e. the mean square displacement of a step edge as function of distance parallel to the edge, is defined as

$$G(y) \equiv \left\langle \left[x(y - y_o) - x(y_o) \right]^2 \right\rangle_{y_o} \qquad \text{Eq. 2.15}$$

where the brackets indicate an average over an ensemble of initial step positions y_0. Using this definition, the spatial correlation function can be calculated directly from the measured step edge geometry, x(y). For small step edge distances, y smaller than the correlation length[182], the average of G(y) yields an initially linear behavior:

$$G(y) \equiv kT|y| \Big/ \tilde{\beta} = yb^2/a \qquad \text{Eq. 2.16}$$

where $\tilde{\beta}$ is the step edge stiffness, and b^2/a is the step diffusivity. The experimental correlation function G(y) of every image was used to determine the linear region,

over which persistence and survival probabilities were evaluated. As has been previously reported for the Al/Si(111) system[183], the step edge diffusivity for this data set follows a Boltzmann dependence on temperature, increasing from 0.45Å at 770 K to 1.00 Å at 1020 K.

2.2 Experiment

STM images were measured on Al/Si(111)-($\sqrt{3}\times\sqrt{3}$) R30° surfaces at temperatures ranging from 720 K to 1070 K. Growth parameters were controlled to maintain the surface structure in the ($\sqrt{3}\times\sqrt{3}$) R30° reconstruction induced by the deposition of Al onto the Si(111) surface[177, 183]. The experiments were conducted in a UHV chamber (base pressure ~6x10^{-11} Torr) equipped with a VT STM (Omicron), a rear-view LEED (Physical Electronics Industries), and a mass spectrometer (Pfeiffer Vacuum). The vicinal Si(111) Samples (As-doped, 10mΩ cm) were misoriented by 0.5° towards the $[11\bar{2}]$ direction. The Si surface was cleaned by several 5-s flashes at 1520 K with subsequent cooling at a slow rate (~20°/minute) through the (1x1)-to-(7x7) phase transition.

The Al/Si(111)-($\sqrt{3}\times\sqrt{3}$) R30° reconstructed surface was prepared by evaporation of 0.25-0.33 ML of Al at a deposition rate of 0.5 ML/min on a Si substrate held at 1020 K[184, 185] and was monitored by LEED. The pressure during evaporation was below 3×10^{-11} Torr and the Al flux was measured by a water cooled quartz microbalance (Leybold Inficon). The Si substrate was heated resistively with direct current while the temperature was measured via an infrared pyrometer. About

0.5 h of thermal stabilization was used before STM measurement at elevated temperatures.

The images chosen for this study were of two sizes, ($300nm^2$) and ($500nm^2$) with scan rates 3 μm/s and 15 μm/s. and pixel sizes 0.586 nm and 0.977 nm respectively. Where possible, only images that included enough monatomic steps to facilitate more than eight different step edge samplings were used for this analysis. Only single-layer steps were analyzed. For the analysis, the spatial STM images used must represent a 'snapshot' of the system, e.g. there should not be any significant edge dynamics occurring during the image acquisition [183]. At temperatures below 770 K, fluctuations are absent over time intervals of several minutes, while at 1020 K steps can fluctuate on the order of seconds[177]. Therefore, to obtain viable information above 870 K, samples were prepared at elevated temperatures and were then quenched at an initial cooling rate of over 200 K/s to room temperature in order to capture and preserve the step edge displacements[183].

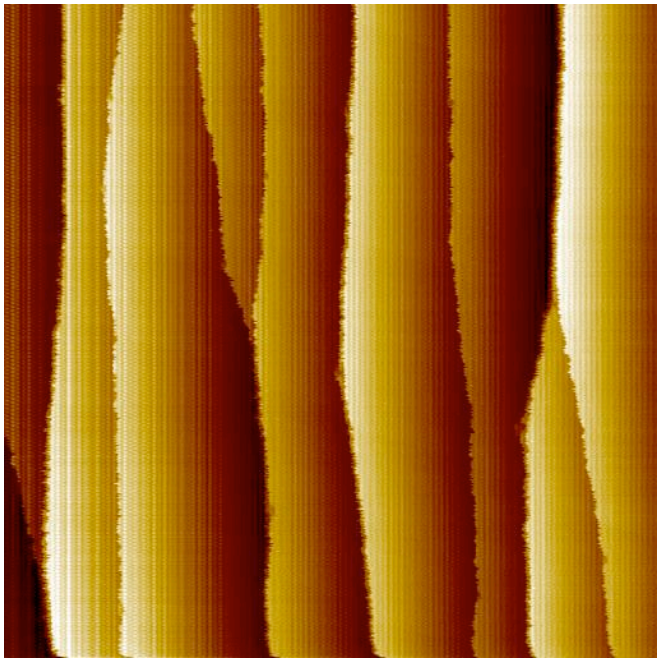

Figure 2.3: **A (500nm x 500nm) STM image of Al/Si(111) with pixel size of 0.977 nm, measured at 970 K. The single step heights are 3.1Å.**

A representative spatial image is presented in Figure 2.3. Step displacements are defined by the x coordinate, as stated earlier[168]. The spatial deviations of each image's step edges x(y) are extracted after cropping the step edge of interest to eliminate any step regions that are marred by defects or pinning sites, and flattening the upper and lower terraces. Each constant-y slice of the step edge image is fit to an analytic step-like hyperbolic tangent function and the extracted inflection point of the function is identified as the position of the step. A linear fit of the step positions is then subtracted from x(y) to account for a possible large-scale wandering or rotation of the step edge. Although the positions of the step edges used for this series of experiments were generated by an automated fitting function, positions were also done by hand in a limited number of cases and were in agreement with the automated software. Partial IDL code is given in Appendix A. x(y) is then used to calculate correlation functions, autocorrelation functions, width distributions, persistence

probabilities and survival probabilities. The indicated error bars are the standard deviations (one sigma) and are obtained from the deviations of repeated measurements.

The length of the step analyzed and the pixel size both are important as numerical simulations and theoretical calculations have shown that the persistence scales as $f(y/\delta y)$ as long as $y<L$[157, 162], and the survival scales as $f(y/L, \delta y/L)$ where L is the variable step length and δy is the image pixel size. Each step image used for this analysis was cropped from a larger original STM image, yielding a distribution of effective system sizes, L but the same value of the pixel size δy. For the entire data set, the range of values of $\delta y/L$ was from 0.003 to 0.015. For the steps analyzed from any given image the smallest and largest values differed by no more than a factor of two.

2.3 Results

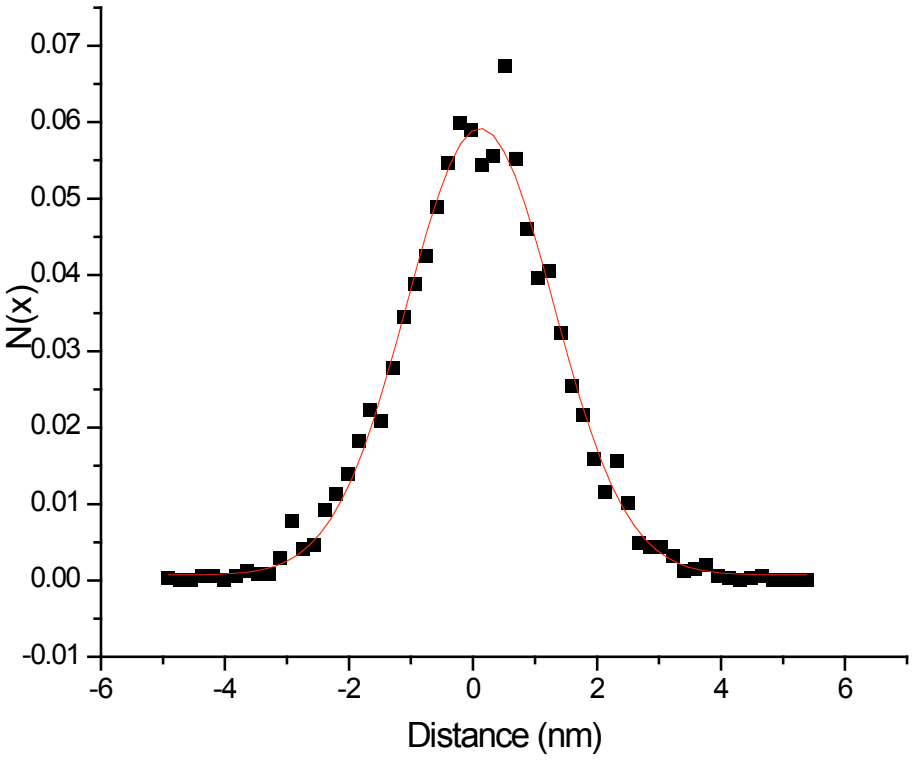

Figure 2.4: Stationary single-site height distribution for all data taken at 920 K. The fitting parameters are x_o = 0.118 ± 0.020 nm and w = 2.37 ± 0.05 nm.

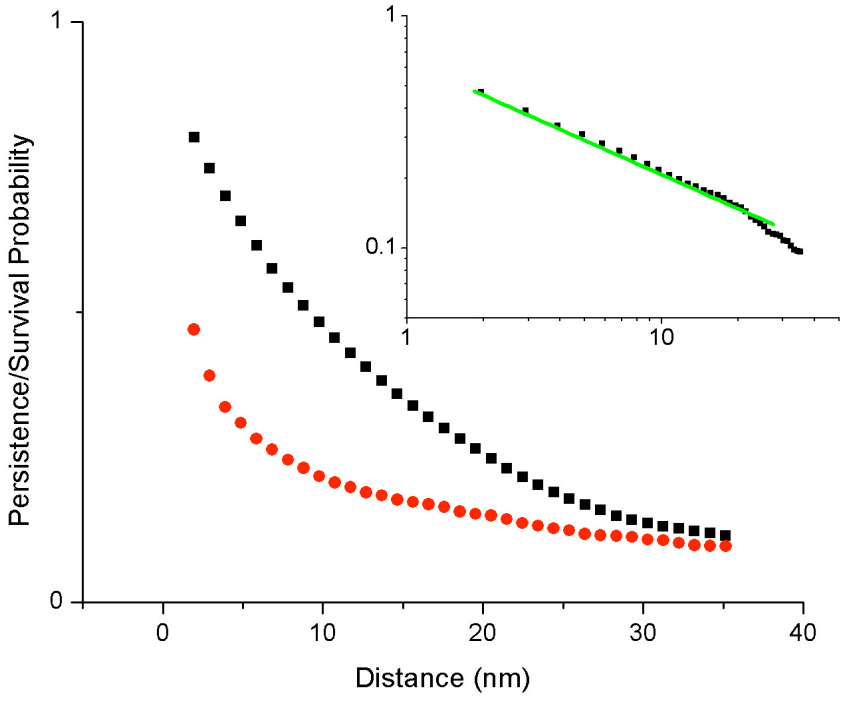

Figure 0.5: **Representative persistence and survival probability data. The data were taken at 970 K, from an STM image with pixel size of 0.977 nm. The persistence and survival curves are represented by squares and circles respectively. The inset is the same persistence curve using logarithmic scales. The solid green line is a power law fit to the data over the linear region of the spatial correlation function with the persistence exponent θ = 0.59. Error bars are 1-sigma values of measurements on seven to ten step segments each measured from the steps in a single STM image. The true standard deviation would be obtained in the limit of a large number of such measurements, and here is estimated by a sampling of several such images.**

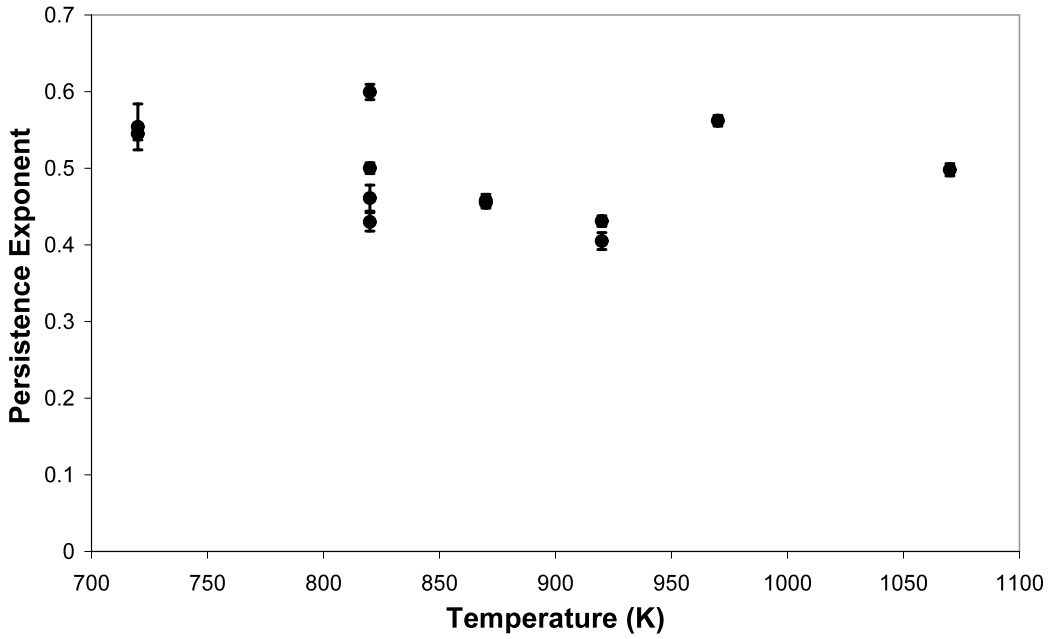

Figure 2.6: Persistence exponents vs. temperature. Error bars are 1-sigma values of measurements on seven to ten step segments each measured from the steps in a single STM image. The true standard deviation would be obtained in the limit of a large number of such measurements, and here is estimated by a sampling of several such images.

Theoretical discussions implicitly assume that the equilibrium step displacements have a Gaussian distribution[165]

$$P(x) = \left(-2\left[\frac{(x - x_o)}{w} \right]^2 \right) \qquad \text{Eq. 2.17}$$

where x_o is the maximum of the distribution and w is the width of the distribution. Using the measured values of x(y), the stationary single site height distributions were calculated and agree with a Gaussian functional form as shown in Figure 2.4 for data measured at 920 K. The fit yields a root-mean-squared width of 2.37 ± 0.05 nm.

The persistence and survival probabilities were calculated as described above over the temperature range 720 K-1070 K. Examples of a linear plot of persistence and survival probabilities versus distance parallel to the step edge, y, are shown in Figure 2.5. The same persistence curve with a power law fit using logarithmic scales

is shown in the inset to more clearly illustrate the date. Deviations from the power law fit occur outside the linear region of the correlation function and therefore do not appreciably effect persistence exponent measurements. The deviations themselves stem from limited statistics at large y as well as possible effects of finite measurement size issues, as discussed below. The average of the persistence curves for all the steps in one image is fit to Eq. 2.11 to extract the persistence exponent θ. Figure 2.6 is a linear plot of the persistence exponent values versus the temperature. No systematic dependence on temperature is observed, and a weighted linear fit of the persistence exponent versus temperature produces a slope close to zero, $(-7.7\text{x}10^{-5} \pm 2.7\text{x}10^{-5})\text{K}^{-1}$. An analysis of the averaged persistence probabilities over all the temperatures results in a persistence exponent of $\theta = 0.498 \pm 0.062$.

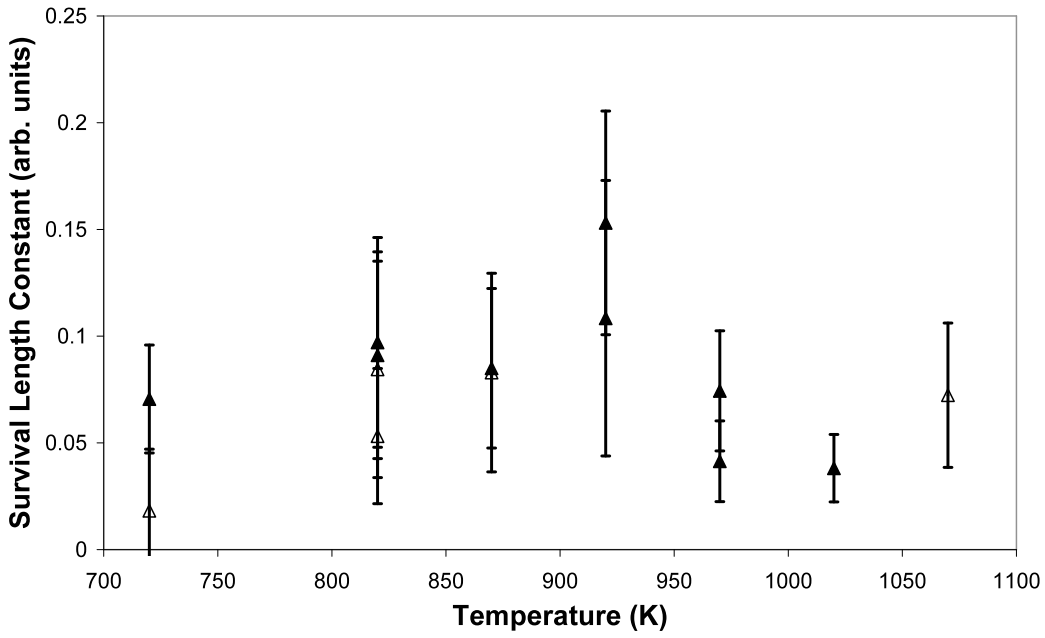

Figure 2.7: Scaled survival decay length vs. temperature. Error bars are 1-sigma values of measurements on eight to ten step segments. Open and solid triangles are from (300nm^2) images and (500nm^2) images respectively. The lengths of the steps analyzed were 37.5-134 nm (720 K), 73–237 nm (820 K), 56–111 nm (870 K), 97–277 nm (920 K), 87–139 nm (970 K), 63–124 nm (1020 K), 118–194 nm (1070 K).

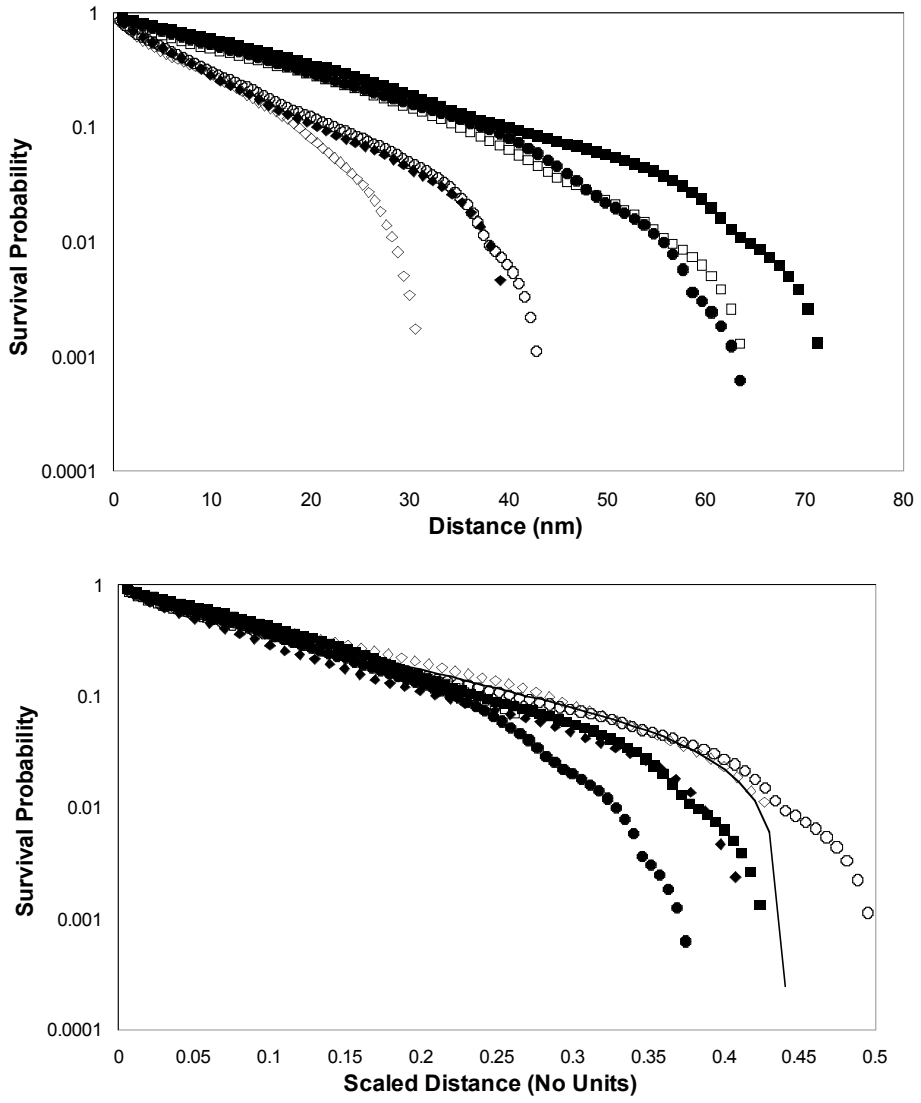

Figure 2.8: Survival probabilities determined from single steps chosen to display measurements at both pixel sizes and a wide range of step lengths. Solid diamonds, squares, and circles are from (500nm^2) images and have system lengths of L = 98.9 nm, 170 nm, and 162 nm respectively. Open diamonds, squares, and circles are from (300nm^2) images and have system lengths of L = 65.8 nm, 154 nm, and 87 nm respectively. a) **Survival probabilities vs. distance, y, parallel to the step edge.** b) **Survival probabilities vs. scaled distance, y/l. The solid line is the theoretical prediction of Eq. 2.20 [165].**

The survival curves are found empirically to follow an exponential decay at small distances:

$$S(y) \sim \exp(-y/y_s) \qquad \text{Eq. 2.18}$$

The measured survival length constant showed a great deal of scatter, with no apparent correlation with changes in temperature. A weighted linear fit of the survival length constant versus temperature produces a slope of $(1.2 \pm 6.6)\times10^{-3}$nm K^{-1}, and an average value of 9.2 ± 5.7 nm. More physical analysis requires correcting for the fact that each measurement was carried out for a step segment of a different length. It is known that survival probability can be described by a scaling function[165]

$$S(y,L,\delta y) = f(y/L,\delta y/L) \qquad \text{Eq. 2.19}$$

where L is the size of the system and δy is the pixel size of the image. Therefore the survival curves for the individual steps in each image were calculated as a function of *y/L*, and then fit as $S(y/L) \sim exp[(y/L/(y_s/L)]$. The individual length constants y_s/L for each of the steps in one image were then averaged to give the average scaled survival length constant for the image. The scaled survival length constants y_s/L are plotted versus temperature in Figure 2.7. The average scaled survival length constant is found to be 0.076 ± 0.033 and a weighted linear fit of the scaled survival length versus temperature produces a slope of $-3.5\times10^{-5} \pm 7.0\times10^{-5}K^{-1}$, e.g. any true temperature variation must be smaller in magnitude than the experimental uncertainty in the data.

To illustrate the effects of step-length scaling, data measured for individual steps with different pixel size and a wide range of step lengths are shown in Figure 2.8a. The collapse of the scaled survival probability curves with scaling as *y/L* is shown in Figure 2.8b. For large distances y, the survival probability statistics significantly decrease and variations between measurements and deviations from the theory are observed. By analogy with the effects of finite measurement times[186],

such deviations of the survival probability may be expected for large distances y due to the finite sample size. No systematic effect of the pixel ratio on the linear region is observed in Figure 2.8. This is confirmed by evaluating of the variation of the scaled decay length y_s/L with pixel ratio, $\delta y/L$, for all the steps analyzed. The result showed no systematic dependence over the measurement range of $0.003 < \delta y/L < 0.015$.

2.4 Discussion

In general, the spatial data obtained in this study is noisier than in previous temporal studies[161, 177, 180, 183]. Nevertheless, the measured persistence exponent value of $\theta = 0.498 \pm 0.062$ is clearly in agreement with the theoretical value of ½. As can be seen in Figure 2.6, there is no apparent temperature dependence of the exponent. This indicates that there is no change in the value of z in Eq. 2.8, and thus no change in the underlying mechanism of the step motion over the temperature range, as observed previously[180]. This lack of temperature dependence is consistent with the previous determination of the temporal persistence exponent for this system[161].

The survival probability curves have been shown to scale with system size as expected, and to follow an exponential decay at small distances. Full theoretical predictions are available for the spatial survival to longer distance scales, which can be written as an expansion[165]:

$$S(u) = 1 - \frac{4\sqrt{3u}}{\pi} + \frac{8\sqrt{u}}{\pi\sqrt{3}}u + \frac{4\sqrt{3u}}{\pi}u^2 - \frac{32\sqrt{3u}(1-a)}{\pi}u^3 \qquad \text{Eq. 2.20}$$

where the parameter a = ½ and the scaled length parameter is y/L = u. This curve is shown as the solid line plotted in Figure 2.8, and reproduces the rapid fall-off of the

survival probability at larger distances. Consistent with the experimental observation, the functional form is indistinguishable from an exponential for $y/L <\sim 0.2$. A fit of the theoretical curve by an exponential over similar length scales provides a scaled survival length constant of $y_s/L = 0.122$, somewhat larger than the average measured value of 0.076 ± 0.033. This empirical survival length constant is a useful experimental rule of thumb. This constant is independent of sample dependent system length, and provides the ratio of the characteristic fluctuation length scales to the system size[165]. Furthermore, an analysis of all the data, illustrated for a subset of the data in Figure 2.8, show that the scaled decay length for the linear exponential region of the fit is robust with respect to changes of a factor of 5 in the pixel size.

2.5 Conclusions & Implications

In summary, spatial first-passage statistics have been used to analyze step fluctuations on Al/Si(111). The temperature-dependent study on a model metal-semiconductor surface was carried out on a variable-temperature STM. The quantitative examination of step fluctuation dynamics was based on analysis of both traditional spatial correlation functions and the statistically based persistence and survival. The stationary displacement distribution of the step deviations is confirmed to have a Gaussian functional form as predicted. The extracted mean squared width provides valuable information concerning the average step edge displacement.

However, when this information is combined with the predictive nature of persistence and survival studies, the experimentally meaningful length scales are easily extracted. The spatial persistence exponent is measured to be 0.498 ± 0.062 in agreement with the theoretical prediction of ½ for the Edwards-Wilkins model. This

is further confirmation that the step fluctuations in this system are governed by random exchange of mass with the terraces over the entire temperature range of observation. An effective exponential form for the survival probabilities is found, with a scaled survival length constant value of 0.076 ± 0.033. The survival probability is observed to scale directly with y/L, where y is the step edge position and L is the step length, and the overall shape of the curve agrees well with theoretical prediction[165]. Both the extracted persistence exponent and survival length constant are observed to be temperature independent over the range 720K-1070K, where the underlying mass transport rates in this system change by three orders of magnitude[177]. This can be traced back to the finite sample size of the measurements. Since the step length is playing the role of the correlation length, the temperature independence of the persistence exponent and of the survival length constant is expected.

Chapter 3: Charge Transport in Ultra-thin Pentacene Films*

The 1/f noise in pentacene thin film transistors has been measured as a function of device thickness from well above the effective conduction channel thickness to only two conducting layers. Over the entire thickness range, the spectral noise form is 1/f, and the noise parameter varies inversely with gate voltage, confirming that the noise is due to mobility fluctuations, or the natural fluctuations in the mean charge carrier path, even in the thinnest films. Hooge's parameter varies as an inverse power-law with conductivity for all film thicknesses. The magnitude and transport characteristics of the spectral noise are well explained in terms of percolative effects arising from the grain boundary structure.

*This chapter is adapted from: Percolative effects on noise in pentacene transistor B. R. Conrad, W. G. Cullen, W. Yan, and E. D. Williams,Appl. Phys. Lett. 91, 242110 (2007) doi:10.1063/1.2823577

3.1 Introduction

Despite significant recent improvements in the performance of organic thin film transistors, transport mechanisms in these devices remain poorly understood. Of particular importance is the issue of conduction channel quality. As organic devices decrease in size, their active conduction channels become thinner and the ratio of signal to noise is expected to increase[187]. However, low frequency conductance noise is generally seen to be more sensitive than the absolute conductance to conduction channel defects [188]. Therefore the importance of understanding noise mechanisms is an increasing concern for industry[189] and associated efforts in noise modeling[190] and prediction[191, 192]. Previous reports show that mobility fluctuations generate noise in organic devices, but reports of the noise magnitude and dependence on transport parameters such as gate voltage V_g and source-drain voltage V_{sd} vary significantly[193-196].

3.2 Organic Device Fabrication

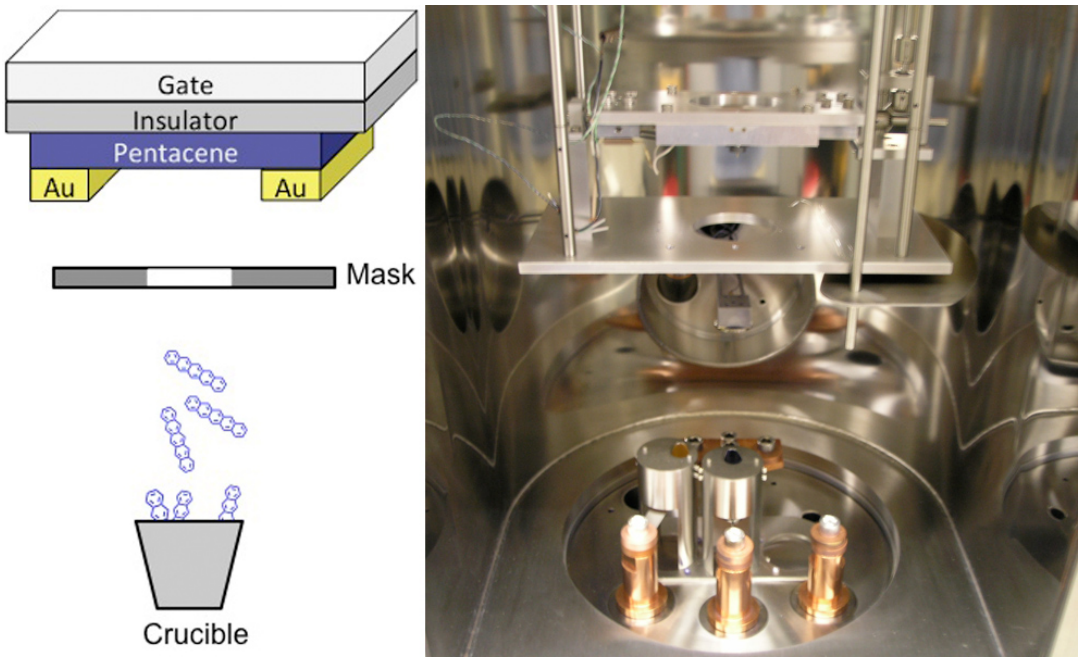

Figure 3.1: a) Illustration of physical vapor deposition (PVD). b) Photograph of the interior of the PVD75 evaporation system.

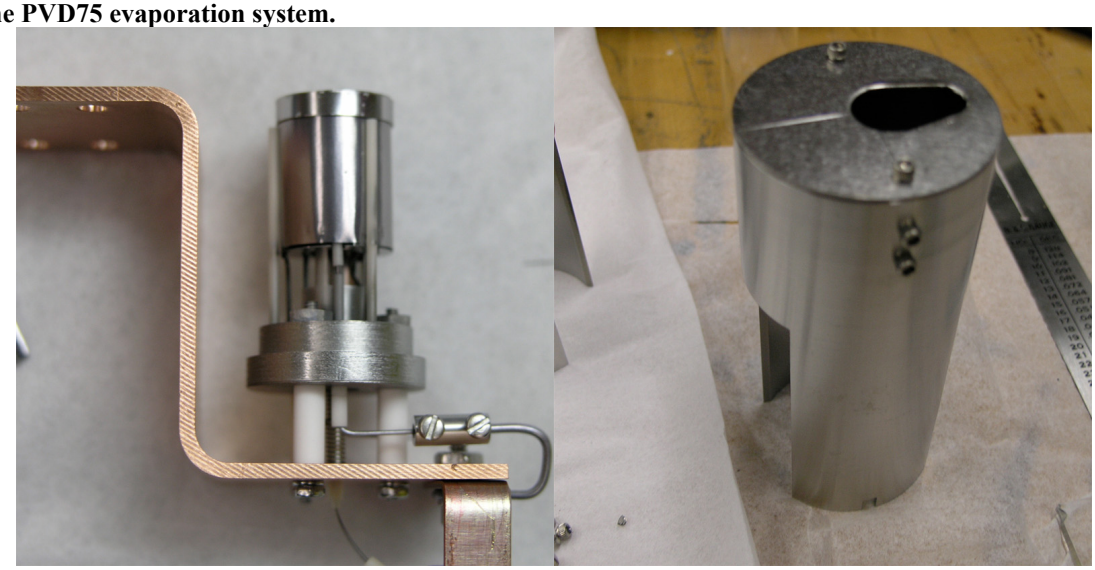

Figure 3.2: a) Image of homemade effusion cell. b) Image of stainless steel cylinders used to focus evaporant.

As described earlier in chapter 1 of this dissertation, organic materials can be deposited using several different techniques. For the transistors fabricated in this and all subsequent chapters, the organic materials composing the conduction channel are

deposited via evaporation in high vacuum (~$1x10^{-7}$ Torr) unless specified otherwise. All fabricated devices were top contact devices, as illustrated in the physical vapor deposition configuration of Figure 3.1a. A substrate, typically 300 nm SiO_2, is cleaned by 5-minute sonication in acetone and isopropanol and dry N_2 drying. The substrate is then placed in a PVD 75 high vacuum chamber, as shown in Figure 3.1b. After vacuum levels reach ~$1x10^{-7}$ Torr, a shutter is closed and the source organic material is heated to induce sublimation. If desired, the pentacene source material can be heated to just below it's evaporation temperature and held there for > 1 hour. This procedure allows for impurities with evaporation temperature below that of pentacene's to sublime, thereby purifying the source material. In order to allow for uniform heating of the pentacene source material, an effusion cell was developed by William Cullen, and is shown in figure 3.2a. Metal shields shown in Figure 3.2b, resembling cylinders with holes in the top, help to collimate the cone of evaporated material. Shadow masks can then pattern the focused plume of source material, as shown in Appendix B. Vacuum is then broken, the evaporation mask changed, and metal electrodes can be deposited on the organic material in a similar process.

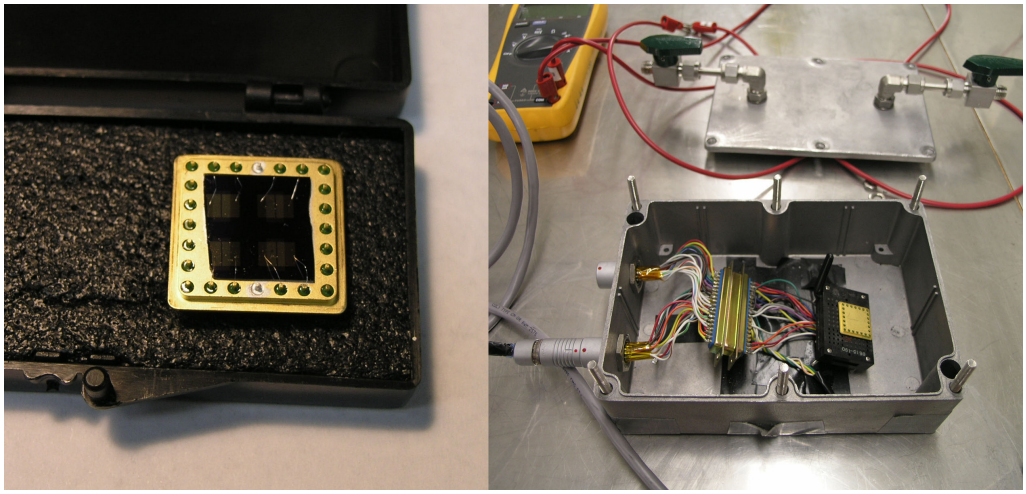

Figure 3.3: **a) Transistor chip carrier with a set of four-pentacene top contact transistors wire bonded. b) Open transistor measurement box with lid.**

Transport measurements of the fabricated transistors are conducted in a dry nitrogen environment, unless otherwise specified. Electrical contacts to the device are made by wire bond to a chip carrier shown in Figure 3.3a, which is housed in an measurement box. A measurement box with electrical feedthroughs, shown in Figure 3.3b, maintains a flow of dry N_2 gas. Samples are left in the N2 environment for at least 12 hours prior to measurement to ensure a steady state configuration and no further gas doping of the device. Devices can be left in the measurement box for up to one week without discernable changes to the electrical characteristics.

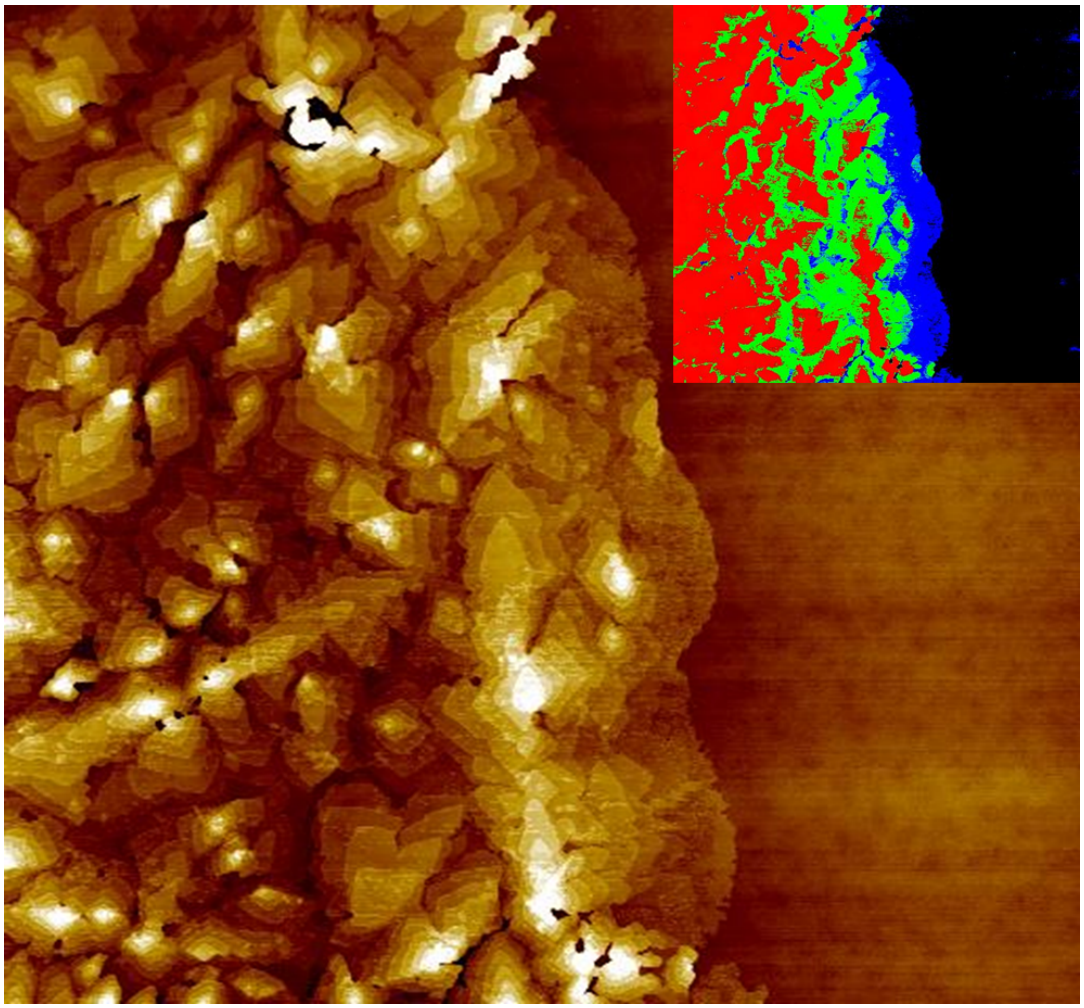

Figure 3.4: A (20 μm x 20 μm) Atomic Force Microscopy image of the conduction channel edge of a 7nm pentacene device. Two complete pentacene layers are mostly covered by increasingly less complete layers. The inset depicts the same image with shading (colors) representing mostly complete pentacene layers where dark gray (blue) is the first pentacene layer, white (green) is the second and third pentacene layers, and medium gray (red) is larger than three layers.

We have measured the spectral drain current noise of Pn-TFTs as a function of the device organic conduction layer thickness, or number of complete pentacene layers, in order to clarify the noise generation mechanism. Device thickness is studied from a thick film regime[197-200] of an electrostatically limited conduction channel to the thin-film regime regime where transport is physically limited to two continuous layers of pentacene as shown in Figure 3.4. It is found that slow-grown

Pn-TFTs display 1/f noise that is independent of conduction channel thickness and that the main mechanism of noise generation is consistent with mobility fluctuations over the entire thickness range. The device mobility decreases and the noise magnitude increases with decreasing conduction channel thickness. It is shown that these dependencies can be quantified in terms of changes in the channel conductance similar to those of percolative systems.

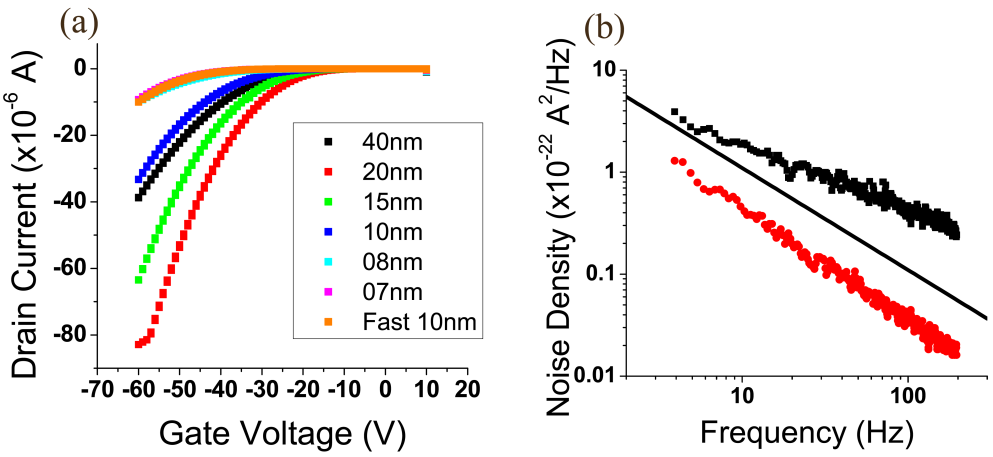

Figure 3.5: (a) **Averaged transfer curves for film thickness 40nm to 7nm and a set of 10nm devices fabricated with a deposition rate 120 times faster** (b) **Spectral noise density S for 10 nm thick devices: open red circles - devices fabricated with slow pentacene growth,** $S \propto f^{-1.05}$**; black squares - devices fabricated with fast pentacene growth,** $S \propto f^{-0.64}$**. The black line represents the theoretical** $S \propto f^{-1}$**.**

Pentacene device I/V characteristics are in general highly sensitive to the substrate surface chemistry and topography, since these properties greatly influence the morphology of the first few layers of the thin film and therefore the majority of the conduction channel[197, 199, 201]. Here, heavily doped silicon (100) wafers with 300 nm (±3%) thermally grown oxide were used as substrates and all devices were made from the same silicon wafer. The substrates were prepared by sonication in acetone and isopropanol (IPA) for 5 minutes each, rinsed in IPA, and then dried

with pure nitrogen. The pentacene was thermally deposited in a vacuum chamber with a base pressure of $<10^{-7}$ Torr, with a substrate growth temperature of 330K and a deposition rate of 0.03Å/s. The devices were top contact devices with 50nm thick Au source-drain electrodes deposited *in-situ*. Transport measurements were conducted in a pure nitrogen atmosphere at room temperature after at least a 12-hour degassing period to minimize atmospheric doping. All reported results are averaged over measurements of at least three separate devices. The averaged transfer curves for films ranging in thickness from 40nm to 7nm and a set of 10nm devices with a deposition rate 120 times faster than the other reported devices are shown in Figure 3.5a. As has been reported previously [202], an optimum mobility is obtained for intermediate thicknesses of 15-25 nm.

3.4 Percolation: Theory & Analysis

Organic thin film transistors (TFT's) typically display flicker (1/f) noise[193, 195] in the linear IV regime, where $|V_{SD}|<<|V_G-V_{TH}|$ and $|V_G|<|V_{TH}|$, for low frequencies of roughly 1Hz-10kHz[188, 203], if prepared under ideal growth conditions. Empirically, we expect the current noise to have the form

$$S = \frac{A \cdot I_{SD}^2}{f^{\alpha}} \qquad \text{Eq. 3.1}$$

where S is the spectral noise density, f is the frequency, the exponent α is a constant, A is the noise magnitude coefficient, and I_{SD} is the device source drain current. For all the devices prepared as described above, the spectral noise density was observed to obey

$$S \propto \frac{I_{SD}^{2.0\pm0.1}}{f^{1.0\pm0.1}} \qquad \text{Eq. 3.2}$$

for the range 3Hz – 10kHz, as shown with the lower curve in Figure 3.5b. Deviations from the typical α =1 behavior for organics usually result from a far from equilibrium growth rate[204, 205] as can be seen in the upper curve in Figure 3.5b.

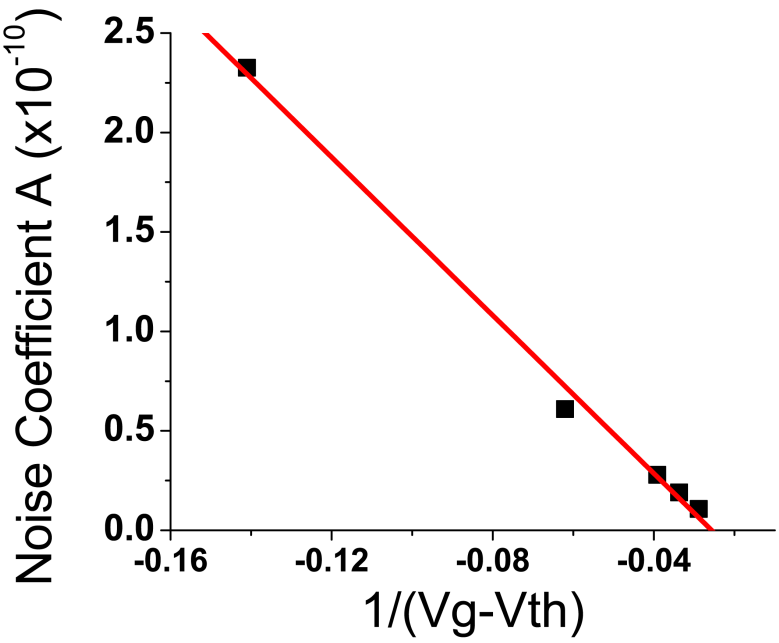

Figure 3.6: Noise constant (Eq. 3.1) as a function of inverse difference between the gate voltage and the threshold voltage. The black squares indicate a typical device while the line indicates dependence $A \propto (V_G - V_{TH})^{-1}$.

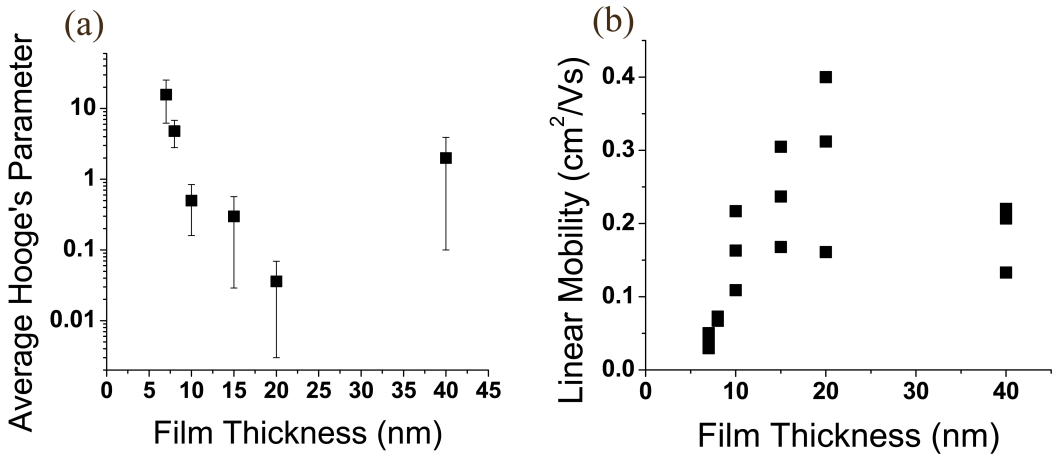

Figure 3.7: (a) Average Hooge's constants (Eq. 3.4) and (b) mobility as a function of the device pentacene film thickness.

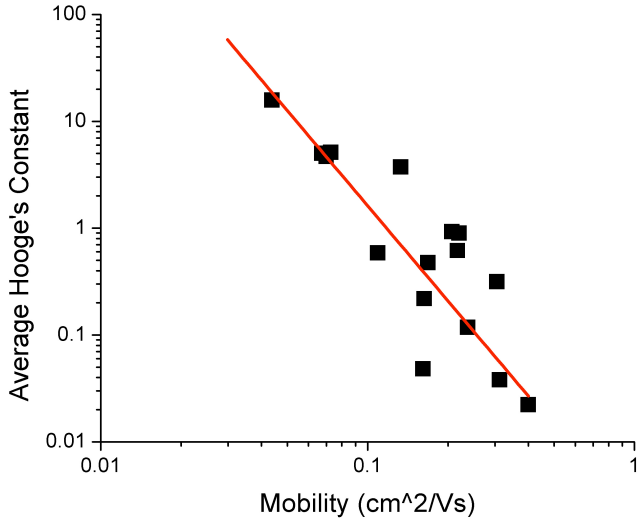

Figure 3.8: Average Hooge's constants (Eq. 3.4) as a function of the device pentacene film mobility. The black squares indicate each device while the line indicates dependence $a_H \propto \mu^{-w}$ where w = 2.9±0.4 .

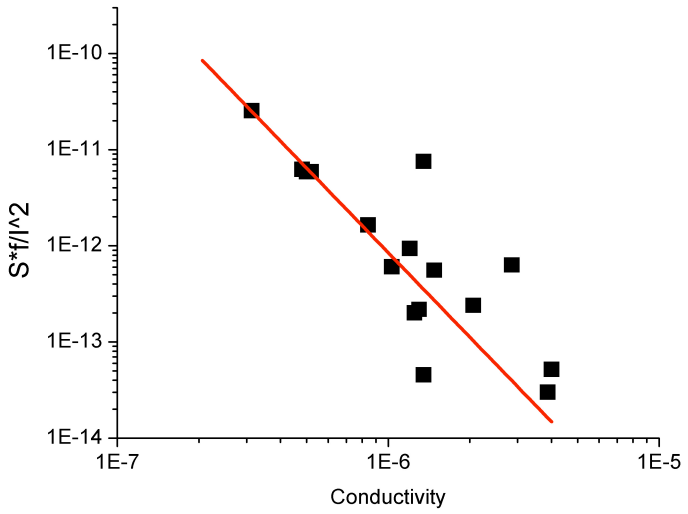

Figure 3.9: Average noise magnitude coefficient A as a function of device conductivity. The black squares indicate each device while the line indicates dependence $S/I^2 \propto \mu^{-w}$ where w = 2.9±0.4.

When the noise is primarily due to mobility fluctuations, the noise coefficient can be written as $A=\alpha_H/N$ for homogeneous conduction channels under homogeneous electric fields, where α_H is Hooge's parameter and N is the total number of carriers in the system[187, 188, 206]. The number of charge carriers is well estimated by treating the device as a parallel plate capacitor:

$$N = \frac{c_g}{e} \cdot \left(V_G - V_{TH} - V_{SD}/2\right) \text{ where } c_G = L \cdot W \left(\frac{\varepsilon_{SiO_2} \cdot \varepsilon_{Pn}}{d_{SiO_2} \cdot \varepsilon_{Pn} + d_{Pn} \cdot \varepsilon_{SiO_2}} \right), \qquad (3.3a,b)$$

where V_{SD} is the source-drain voltage, V_G is the gate voltage, V_{th} is the threshold voltage of the device, c_g is the capacitance of the device, and ε_{SiO2} (d_{SiO2}) and ε_{Pn} (d_{Pn}) are the dielectric constants (thicknesses) of the insulating layer and pentacene, respectively. Within the linear I/V regime, the noise coefficient can then be written as

$$A = \frac{\alpha_H \cdot e}{c_G} \cdot \frac{1}{\left(V_G - V_{TH} - V_{SD}/2\right)} \qquad (3.4)$$

It can be seen in Figure 3.6 that the measured noise coefficient A is inversely proportional to the effective conduction channel voltage (V_G-V_{TH}-V_{SD}/2), thus the behavior of the noise is consistent with expectations for a homogenous semiconductor governed by mobility fluctuations[187, 188, 207]. The value of Hooge's parameter can be determined from the noise coefficient A, using the capacitance calculated as per Eq. 3.3. The result is shown as a function of the pentacene conduction channel thickness in Figure 3.7a. For device thicknesses below 10nm, physical limitations on the conduction channel, and therefore mobility, are expected[197]. The dependence of the mobility on thickness for these devices is shown in Figure 3.7b. Plotting Hooge's constant as a function of mobility in Figure 3.8, Hooge's parameter has a strong dependence on mobility, specifically $a_H \propto 1/\mu^w$ where w=2.9±0.4. The large values of Hooge's parameter at small film thicknesses are consistent with previous observations of large values for inhomogeneous samples[206]. In the following, we will discuss the physical basis for this by evaluating the correlation of the noise with the mobility.

An increase in noise levels in inverse proportion to mobility is expected in the case of semiconductor transport limited by impurity scattering[188], and strong correlations of noise with mobility are often observed in devices with limited mobility[189, 203, 208]. Increased noise in thin films has also been attributed to inhomogeneity in the long-range film structure, which can also be associated with current crowding[206, 209]. For organic semiconductors, it is generally accepted that transport is dominated by hopping and that grain boundaries disrupt transport, although there is still debate as to the detailed mechanism[9]. Therefore, it is not

unreasonable to expect analogies with the behavior of noise in disordered materials. Consider that resistivity ρ is inversely proportional to the number of carriers N as well as the mobility, specifically $\rho \propto 1/(N \cdot \mu)$. If we fix the number of charge carriers N with a gate voltage, the mobility is the determinant of resistivity. For structurally disordered systems, a percolative model can be a useful way to interpret variations in noise. In such a model the sample is treated as a mixture of conducting and insulating components. As the fraction of the conducting component *p* increases beyond some critical fraction p_c, the sample resistivity exhibits a power law decay of the form ρ $\rho \propto (p - p_c)^{-t}$.

In percolative transport, the spectral noise density S is observed to decay as $S/I^2 \propto (p - p_c)^{-\kappa}$, where *p* is the conductive phase fraction and κ is a parameter that depends on the details of the percolation model[210]. Other models, such as bond percolation or random resistor networks, can also be employed, yet the general scaling results still apply. From the expressions for the spectral noise density *S* and the resistivity ρ, the scaled current noise depends on channel resistivity as $S/I^2 \propto \rho^w$, and thus at fixed number density as $S/I^2 \propto \mu^{-w}$, with the exponent $w=k/t$. For the devices described here, Figure 3.9 shows w=2.9±0.4 is in agreement with the value of *w* previously calculated in this work and several different percolation models which predict similar results[190]. It is important to note that these power law behaviors are only universal near percolative threshold p_c even though effective power law behavior is often observed over a wide range of resistivities. The essential insight to be gained from the connection to percolation models is that the noise in the pentacene TFT's is closely correlated with the distribution of the conducting, or insulating, elements,

which could also cause current crowding and concomitant increases in noise[206, 211]. As seen in Figure 3.2 the most prominent random defect in a pentacene thin film is a grain boundary and therefore the most likely mechanism for the mobility dependence of Hooge parameter is transport across these boundaries.

3.5 Conclusions & Implications

Even though the IV characteristics of Pn-TFT's are in general highly sensitive to the surface, the limitation of conduction to only a few layers of pentacene does not change the functional form of the noise behavior, as might have been expected. Therefore, the dielectric interactions in the bottom most layers of Pn-TFT's apparently do not dominate the noise signal, and the primary 1/f noise mechanisms must be similar over the entire conduction channel thickness. The results are consistent with a mechanism of conductivity fluctuations due to charge hopping through the resistive barriers[212] between grains. This mechanism is likely to explain similar noise signatures seen in organic polymers[213] as well. The hopping transport must be similar throughout the film and is effectively not influenced by its proximity to the dielectric. Interlayer transport effects might contribute to the noise but the anisotropic mobility for these types of organic molecules[214, 215] and the layer-dependent measurements reported here suggest that interplanar effects are small in comparison to the planar grain boundary effects.

In conclusion, 1/f noise was measured as a function of pentacene film thickness from two continuous layers to an electrostatically limited conduction channel. Mobility fluctuations dominate the noise spectrum, independent of the conduction channel thickness. Large values of Hooge's parameter are explained by

quantifying their variation as a power-law with the conductivity, similar to the behavior of percolative systems and suggesting the importance of the random spatial distribution of grain boundaries to the noise generation mechanism. Surprisingly, the functional form of the resistive grain boundary-generated noise is independent of proximity to the gate oxide.

Chapter 4: Impurity Doping of Pentacene TFTs*

Pentacenequinone (PnQ) impurities have been introduced into a pentacene source material at number densities from 0.001 to 0.474 to quantify the relative effects of impurity content and grain boundary structure on transport in pentacene thin-film transistors. Atomic force microscopy (AFM) and electrical measurements of top-contact pentacene thin-film transistors have been employed to directly correlate initial structure and final film structures, with the device mobility as a function of added impurity content. The results reveal a factor four decrease in mobility without significant changes in film morphology for source PnQ number fractions below ~0.008. For these low concentrations, the impurity thus directly influences transport, either as homogeneously distributed defects or by concentration at the otherwise-unchanged grain boundaries. For larger impurity concentrations, the continuing strong decrease in mobility is correlated with decreasing grain size, indicating an impurity-induced increase in the nucleation of grains during early stages of film growth.

*This chapter is adapted from: Effect of Impurities on Pentacene Thin Film Growth for Field-Effect Transistors, Elba Gomar-Nadal, Brad R. Conrad, William G. Cullen, Ellen D. Willams, J. Phys. Chem. C. 112(14); 5646-5650 (2008), doi:10.1021/jp711622z

4.1 Introduction

During the last decade, dramatic advances have been made in the performance of organic thin film field-effect transistors (OTFTs), and their field-effect mobilities have exceeded those of transistors based on amorphous silicon[216, 217]. Despite the fast-paced progress, fundamental questions related to the mechanism and limiters of device operation remain unanswered. Both thin film morphology and chemical impurities have been identified as limiting charge carrier mobility. Studies with single crystals have shown the strong effect of small concentrations of impurities[28, 218-220]. Studies of thin-film growth have revealed the mechanisms underlying grain formation in thin films as well as self-driven polycrystallization[221, 222]. However, questions still remain as to the specific roles these impurities play.

Reducing the concentration of quinones, which are the dominant impurity in acenes, has been demonstrated to correlate with improved mobility in single crystals[28, 220]. The quinone impurity content in commercial acenes has been reported to be about 0.7%[28], however there is also a significant enhancement of the quinone concentration in the near surface region of crystalline pentacene[220]. Thus for single crystals, the mechanisms by which impurities reduce mobility may involve both impurities located in the bulk of the crystal and at interface sites and structural defects such as dislocations[201, 223, 224]. Because of their increased size and non-planar structure, quinones may degrade mobility through the creation of structural defects. These defects in turn may affect film stability and moisture sensitivity, and induce local potentials with further effect on transport[225, 226].

In thin film transistors, the growth of the organic semiconductor results in a polycrystalline structure with typically much lower mobilities than that obtained for single-crystal devices[217]. The lower mobility has been attributed to the influence of grain boundaries and dislocations as sites for charge traps[71, 72, 198, 227]. Structural defects in the thin film arise from the growth properties. For pentacene on

SiO_2, growth occurs via nucleation with initial two-dimensional growth[228]. The critical nucleus size is small, on the order of two or three molecules, and the subsequent domain growth varies from compact to ramified depending on growth temperature and flux[205, 229, 230]. Growth of the second layer begins before completion of the first layer, and continuing growth is increasingly three-dimensional due to an Ehrlich-Schwoebel-type barrier that prevents diffusion across terrace edges[221]. This growth behavior is common and has been seen in many other types of systems[228, 231]. Since the majority of charge carriers in a thin film transistor are located at the semiconductor-dielectric interface[197, 232], a detailed knowledge of the morphology of the organic thin film at the interface with the dielectric is crucial to understand charge transport.

4.2 Experiment

The experiments were performed by introducing controlled amounts of one chosen type of chemical impurity – 6,13-pentacenequionene (PnQ) – in pentacene (Pn). PnQ (99%, Ref.246883) is an oxidative form of Pn used as starting material in the chemical reaction to produce Pn and is its main impurity[28]. The solid mixtures were prepared by mechanically mixing PnQ with commercial Pn under a dry nitrogen atmosphere in a glove box. The mixtures were made by consecutive solid dilution, starting with a 50% Pn/PnQ mixture, by adding commercial Pn. The mixture components were ground finely with a glass mortar and pestle with repeated grinding and mixing. The compositions tested covered a range of added PnQ from weight percentage +0.0 to +50%, equivalent to PnQ number fractions ranging from 0.0 to 0.474. The PnQ thin film composition will be different from the PnQ source material composition and decrease across the thin film thickness since PnQ has a slightly lower evaporation temperature than Pn[28]. However, the film composition will be

directly proportional to the percentage of PnQ present in the source material for films deposited under the same experimental conditions.

A series of top-contact Pn OTFTs were prepared using the PnQ/Pn solid admixtures as the source material. Prime grade silicon wafers (p^+-Si) with 300nm (±3%) thermally grown oxide were used as device substrates. The p^+-Si/SiO_2 substrates were cleaned by sonication in acetone and isopropanol (IPA) for 5 minutes rinsed with IPA and dried with nitrogen. Deposition was performed at 0.09 Å/s at 10^{-7} Torr pressure with the substrate at room temperature. The source materials were increased to deposition temperature (~195ºC) over a 15 min. interval. All of the films were prepared under the same deposition conditions. In addition, some OTFTs were prepared using Pn purified by heating it at a temperature slightly lower than its sublimation temperature for one hour *prior* to the thin film deposition. This method reduces impurities, such as PnQ, that have a sublimation temperature lower than pentacene. The results for these samples are noted as "cleaned Pn" in the figures and tables.

The electrical characterization was performed on films with an equivalent of 50 nm of material deposition, under a nitrogen atmosphere. For OTFT device fabrication, top-contact electrodes (100 nm) were deposited by evaporating gold ($<10^6$ Torr) through a shadow mask with channel length L = 100 μm and width W = 3000 μm. The reported field-effect mobilities μ are the average of at least 4 transistors for added PnQ > +0.5% and the average of at least 8 transistors for added PnQ ≤ + 0.5%. Analysis of the transport data to extract the device parameters followed standard procedures[83]. The mobilities reported are based on the linear mobilities measured for gate voltages between -60 V to -40 V. Mobility values are reported as normalized with respect to the measured mobility of the commercial pentacene (0.0% *added* PnQ), which is 0.11 ± 0.02 cm^2/Vs. Error bars are reported as the standard deviation (one sigma) of the repeated measurements. Tapping mode

AFM was conducted using a DI MultiMode with silicon cantilevers on the device conduction channels after electrical measurement. Additional submonolayer films were also grown and imaged to facilitate nucleation and grain size analysis. Additional phase images were recorded for many samples.

4.3 Analysis

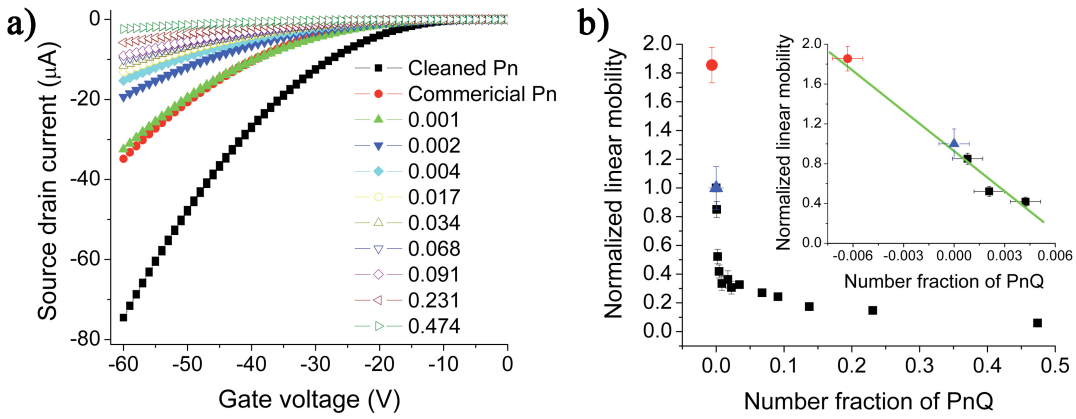

Figure 4.1: (a) Averaged transfer curves of 50 nm film OTFTs prepared: cleaned Pn, commercial Pn, and PnQ/Pn admixtures with a number fraction of added PnQ ranging from 0.000 to 0.474. The gate voltage was swept at a constant V_{s-d} = - 40V. (b) Normalized linear mobility of cleaned Pn (●, full circle), commercial Pn (▲, full triangle) and PnQ/Pn admixtures from 0.006 to 0.474 (■, full squares) *versus* number fraction of added PnQ. The inset is a zoom-in of the lower PnQ concentrations. The solid line is a linear fit to the PnQ/Pn admixture device data.

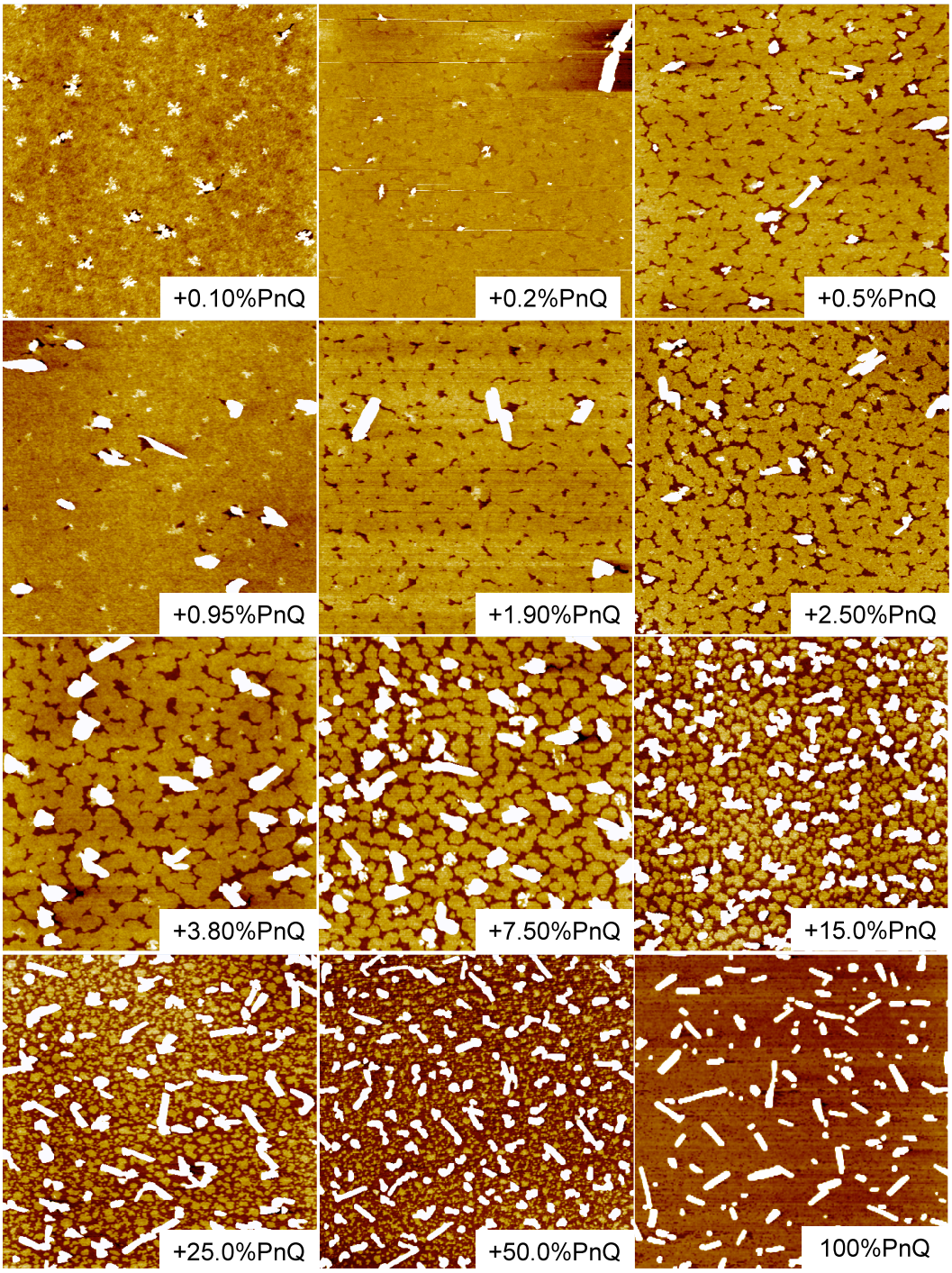

Figure 4.2: **AFM images (10µm x10 µm) of films grown with a deposition time equal to that yielding one monolayer of Pn that were prepared with PnQ/Pn admixture with a percentage of added PnQ from +0.1% to +50% and with 100% PnQ (Care of Elba Gomar-Nadal).**

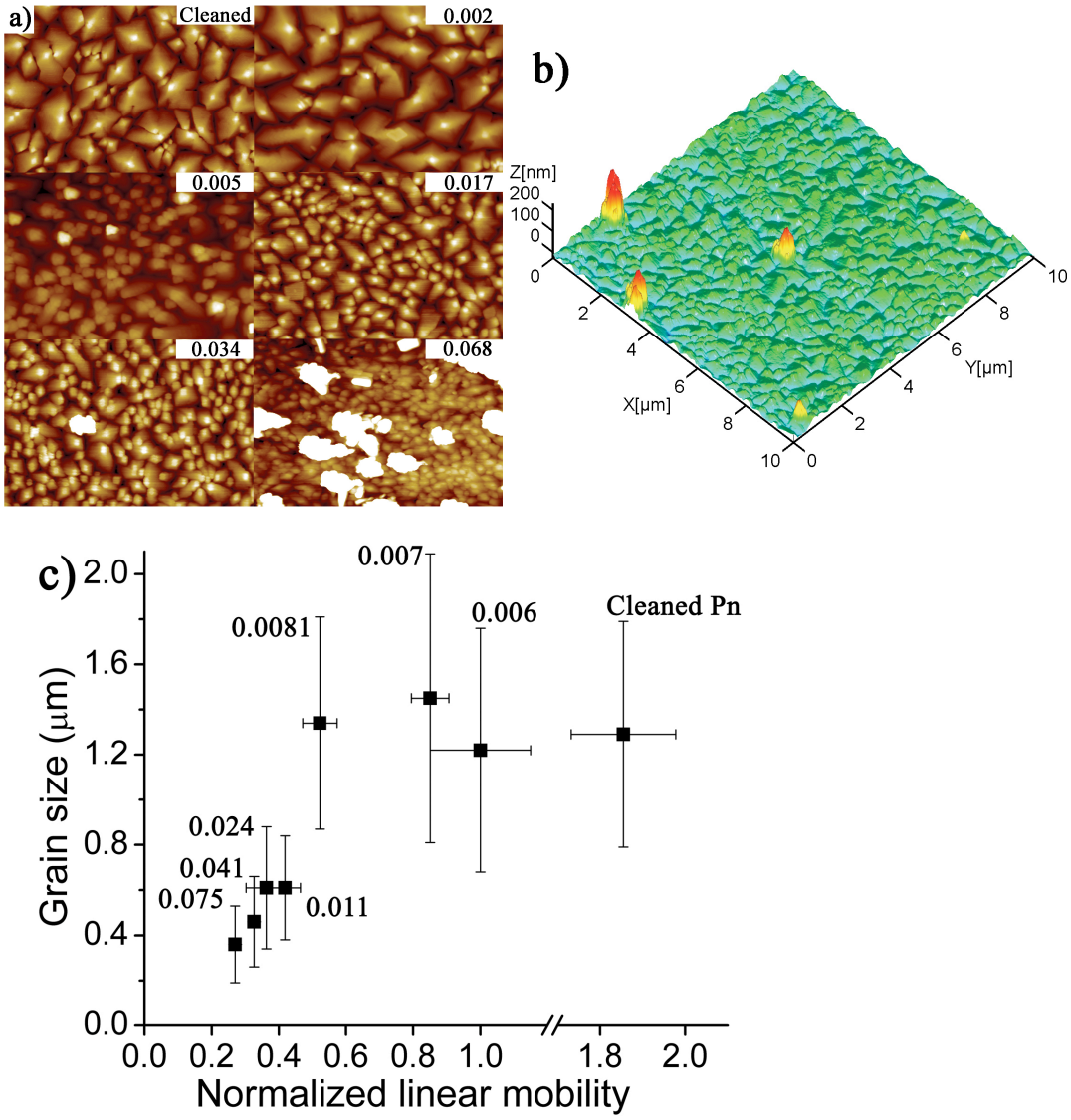

Figure 4.3: **a) 7.5 µm by 5.0 µm AFM images of nominal 50 nm thick films prepared using cleaned Pn, commercial Pn (or +0.0%PnQ) and PnQ/Pn admixtures with a percentage of added PnQ from +0.1 to +7.5% (net number fraction from 0 to 0.068). b) 3D image of a nominal 50nm thick film using 0.034 PnQ number fraction source material. c) Grain size as a function of normalized linear mobility for films presented in Figure 3.2a. Labels on each data point indicate the PnQ number fraction.**

Transfer curves and normalized linear mobility as a function of the number fraction of added PnQ present in the source material for these transistors are shown in Figure 4.1. The threshold voltages and ON/OFF ratios were comparable for transistors fabricated from all the different material compositions, with a V_t average

value of -12 ± 2 V and On/Off ratios of 10^4, as seen in Table 4.1. Beyond an added number density of 0.007 PnQ, the mobility rapidly decreases for low concentrations of PnQ and saturates to low mobility values at high PnQ concentrations as can be seen in Figure 4.1b. The inset of Figure 4.1b focuses on the rapid degradation of the mobility with small amounts of added PnQ. The PnQ/Pn admixture device data is fit to a linear function and plotted in the inset of Figure 4.1b, and can be extrapolated to zero mobility at a number fraction of 0.013 ± 0.004. Also from the inset, we can extrapolate to the reported[28] PnQ content of commercial Pn and see that our data for cleaned and commercial Pn is in good agreement with the expected value of 0.7 ± 0.1% PnQ impurity in the commercial material. To assess the influence of PnQ impurity on the pentacene thin-film morphology, tapping mode AFM images were recorded for these films. The structures resulting from all attempted Pn/PnQ source mixtures are shown in Figure 4.2. Figure 4.2 shows AFM images (10μm x10 μm) of the thin films grown with a deposition time equal to that yielding one monolayer of Pn were prepared with PnQ/Pn admixture with a percentage of added PnQ from +0.1% to +50% and with 100% PnQ.

To simplify the discussion of the experiments, all further PnQ concentrations will be quoted in absolute number fractions in the source, or added PnQ plus the native 0.7% PnQ by mass in commercial Pn. The structures observed for a representative subset of 'low' impurity concentrations are shown in Figure 4.3a. Samples prepared with purified Pn and with a PnQ number fraction of up to 0.008 present similar crystalline grain morphology, with grain sizes (~1μm) significantly larger than those with PnQ number fractions higher than 0.008. As the content of added impurity exceeds number fractions of 0.008, the samples show a drastic change in grain morphology, including a dramatic decrease in grain size. Together with the

small grains, a low density of high-aspect-ratio protruding structures (appearing as white contrast in the AFM images in Figure 4.3a, and shown in 3-d in Figure 4.3b) becomes apparent around a PnQ number fraction of 0.041. These structures are similar in density and shape to those that occur when equivalent amounts of pure PnQ are deposited on clean SiO_2 [233] and the structures seen in the high PnQ concentration AFM images of Figure 4.2, suggesting phase separation of higher concentrations of PnQ from Pn[234, 235].

Added PnQ present in the Pn source material (%)	μ_{Linear} (cm^2/Vs)	$\mu_{Saturation}$ (cm^2/Vs)	V_t (V)	on/off ratio ($x10^4$)
Cleaned Pn*	0.204 ± 0.014	0.168 ± 0.010	-9.38 ± 0.53	4.3 ± 0.7
Commercial Pn (+0.00)	0.110 ± 0.016	0.096 ± 0.012	-14.76 ± 2.15	2.7 ± 0.8
+0.09	0.093 ± 0.006	0.081 ± 0.005	-12.30 ± 0.71	3.2 ± 0.9
+0.23	0.057 ± 0.008	0.045 ± 0.006	-10.60 ± 0.56	1.7 ± 0.2
+0.47	0.046 ± 0.005	0.038 ± 0.004	-11.98 ± 0.44	1.1 ± 0.1
+0.94	0.037 ± 0.005	0.032 ± 0.003	-15.03 ± 0.93	1.1 ± 0.2
+1.90	0.040 ± 0.007	0.034 ± 0.003	-13.35 ± 0.49	1.1 ± 0.1
+2.50	0.034 ± 0.005	0.028 ± 0.003	-13.15 ± 0.41	1.2 ± 0.8
+3.80	0.036 ± 0.002	0.030 ± 0.001	-12.75 ± 0.17	1.2 ± 0.8
+7.50	0.030 ± 0.000	0.024 ± 0.000	-10.40 ± 0.00	0.9 ± 0.1
+10.0	0.027 ± 0.002	0.023 ± 0.001	-12.25 ± 0.21	0.8 ± 0.1
+15.0	0.019 ± 0.002	0.017 ± 0.002	-13.55 ± 0.87	1.5 ± 0.2
+25.0	0.016 ± 0.001	0.014 ± 0.001	-11.83 ± 0.62	0.9 ± 0.1
+50.0	0.007 ± 0.001	0.007 ± 0.001	-13.83 ± 0.79	0.3 ± 0.1
Aldrich PnQ	0.000 ± 0.000	0.000 ± 0.000	-	-

Table 4.1: Summary of performance parameters for pentacene OTFTs prepared using as a source material to deposit the semiconductor thin film cleaned Pn, commercial Pn (+0.0%PnQ) and PnQ/Pn admixtures with a percentage of added PnQ ranging from +0.1 to +50%. All films were ramped from room temperature to deposition temperature in 15 minutes, excluding the cleaned Pn, which was held at 1 hour at 120°C prior to deposition.

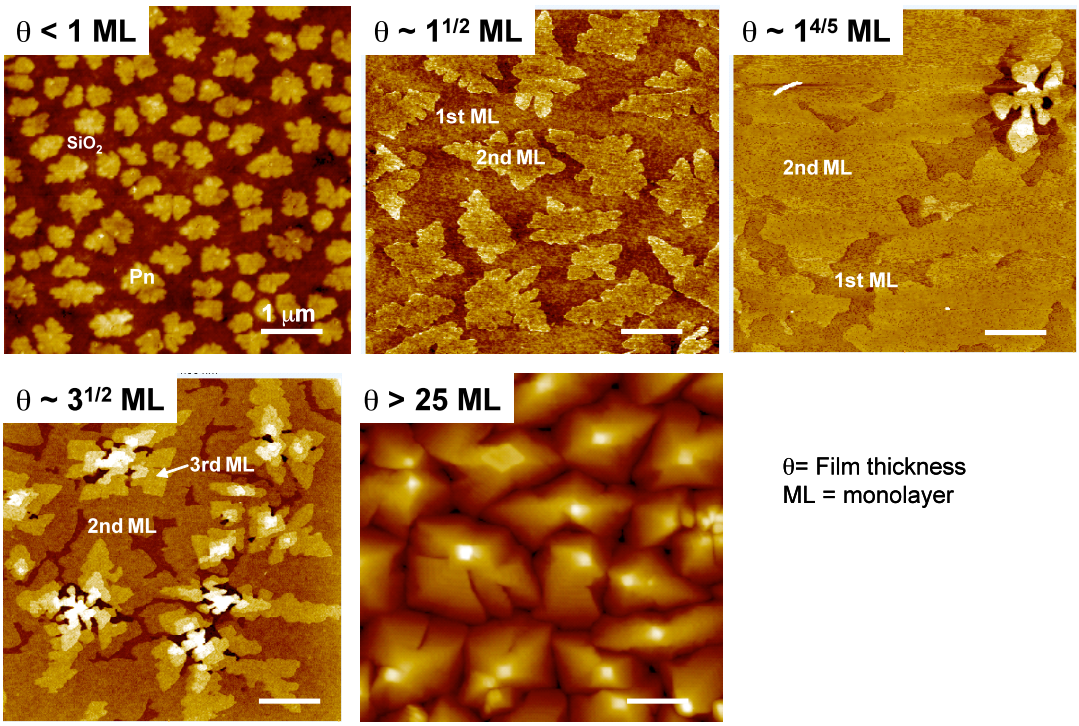

Figure 4.4: AFM images (5 μm x 5 μm) of commercial Pn films with film coverage from less than one monolayer to more than 25 monolayers.

The correlation between the average grain size and the mobility for all the samples measured is shown in Figure 4.3c. The grain sizes are found by using image processing to outline the irregularly shaped grains, finding the areas, and taking the average. The reported grain size is the diameter of an assumed circular grain with the average measured grain size. It is notable that the first rapid decrease in mobility by about a factor of four occurs with no significant change in grain size. Only when the amount of added impurity exceeds a PnQ number fraction of 0.008 does a correlated decrease in grain size also occur. To quantify the effects of the impurity on the growth process and changes in mobility, the thin film structures in the early stages of growth were also measured. In agreement with the literature, the early stages of growth of commercial Pn (a PnQ number fraction of 0.006) occur via layer-by-layer growth, and the first two monolayers are at least 90% completed before the next monolayers start to grow, as seen in Figure 4.4. The structures of films grown with a deposition time equal to that yielding 1 monolayer of Pn/PnQ with a variable PnQ

number fraction are shown in Figure 4.5a. The morphology trends seen in the submonolayer thin film images, such as Figure 4.5a, continue through the growth of the first few complete conduction channel layers, which are responsible for most of the charge transport[197]. Samples prepared with PnQ number fractions at or below 0.008 show the same behavior-formation of an almost complete first monolayer (approximately 15Å thick) and some nucleation sites of the second monolayer. Samples with PnQ number fractions higher than 0.008 display incomplete Pn coverage, and the formation of multi-layer crystallites with both elongated and rounded shapes (10 to 100 nm tall and 10 to few 100 nm long). AFM images of 100% PnQ films (with a deposition time equivalent to 1 Pn monolayer) yield the same type of crystallites with comparable shapes and dimensions covering 20% of the substrate. This confirms that there is substantial material segregation between PnQ and Pn during the film deposition.

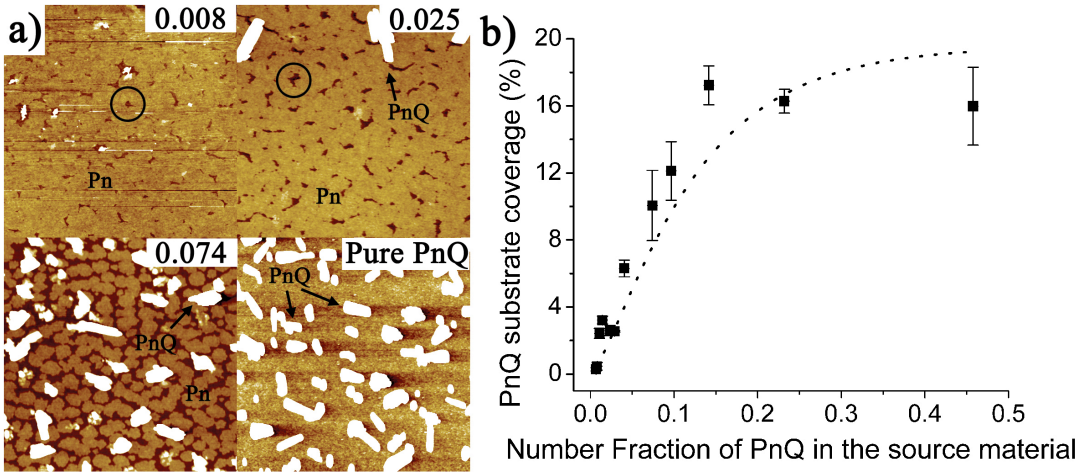

Figure 4.5 a) AFM images of films with a deposition time equivalent to one Pn monolayer, prepared using as a source material PnQ/Pn admixture with a number fraction of PnQ of 0.008, 0.025, 0.074 and with pure PnQ. Regions showing bare SiO_2 are circled. b) Fraction of the substrate covered with PnQ crystallites as a function of number fraction of PnQ. The broken black line is a guide to the eye.

As shown in Figure 4.5b, at a one Pn monolayer deposition time, the fraction of the substrate area covered with PnQ initially increases with a slope slightly greater than one as a function of percentage of added PnQ in the source material, consistent

with PnQ subliming more rapidly than Pn. At approximately 10% areal coverage, the rate of increase of the PnQ areal coverage decreases dramatically, and the areal coverage saturates at about 20%. This is the result of increasing multi-layer growth in the PnQ crystallites, as seen in Figure 4.2. Referring to Figure 4.1b, the mobility drops by a factor of 10 over the PnQ composition range where the areal coverage of PnQ increases only to 10%. Thus the mobility decreases below 10% PnQ impurity cannot be due simply to PnQ-crystallite-induced loss of percolative pathways through the Pn regions.

Absolute PnQ in Source (%)	Number Fraction of PNQ	Nucleation Site Density $(1/\mu m)^2$
0.0 ± 0.1	0.000 ± 0.001	3.9 ± 0.2
0.7 ± 0.1	0.006 ± 0.001	3.8 ± 0.1
0.8 ± 0.1	0.008 ± 0.001	3.1 ± 0.3
1.2 ± 0.1	0.011 ± 0.001	9.7 ± 0.9
2.0 ± 0.1	0.018 ± 0.001	5.1 ± 1.5
3.2 ± 0.1	0.029± 0.001	6.1 ± 1.7
4.5 ± 0.1	0.041 ± 0.001	5.0 ± 0.8

Table 4.2: Island nucleation density as a function of impurity PnQ concentration in source material.

Further information about the impact of the PnQ impurity on the pentacene film growth is provided by evaluating the island nucleation density. This was accomplished by growing films until just before the coalescence of adjacent growing grains begins to measure the size and density of the grains. Nucleation density as a function of PnQ concentration in source material for a deposition time equivalent to 0.3-0.4 ML of Pn is summarized in Table 4.2. In agreement with the observations for bulk thin film morphology (Figure 4.3a), purified samples and samples with PnQ number fractions between 0.006 (commercial Pn) and 0.008 show comparable island number (~3 islands/square micron, of area 0.13-0.14 square micron), as well as shape and spatial distribution[236]. Samples with a PnQ number fraction content above

0.008 have a significantly larger number of nucleation points and correspondingly smaller island areas.

4.4 Conclusions & Implications

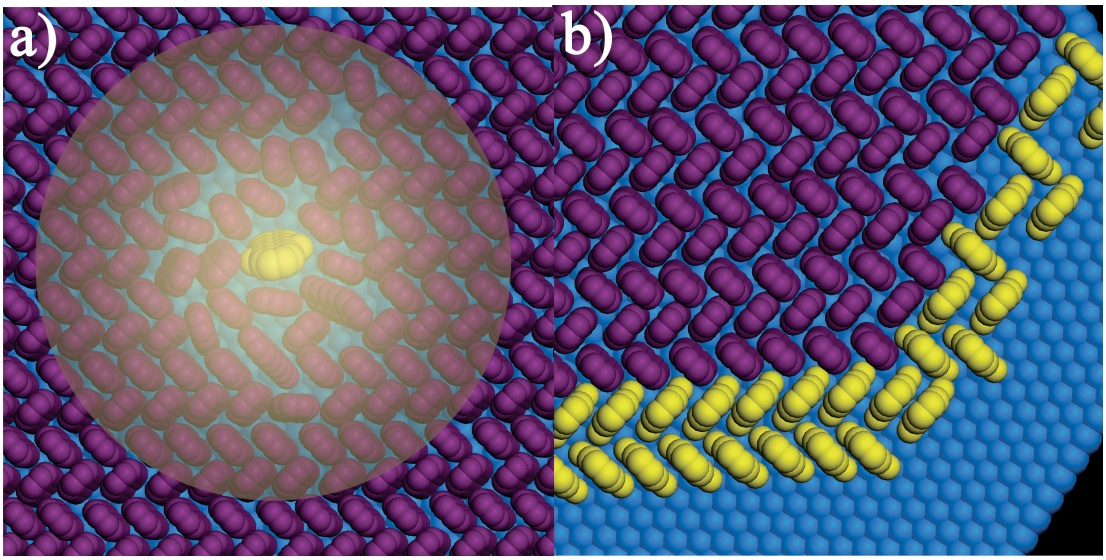

Figure 4.6: a) Illustration of a monolayer of Pn with a single PnQ molecule disrupting the lattice. b) An illustration of a Pn grain boundary surrounded by 2 layers of PnQ.

The evolution of the growth morphology is consistent with a limited solid solubility of PnQ in Pn. If a PnQ number fraction up to about 0.008 can be incorporated in (or at the edges of) growing Pn islands with little disturbance in the long range crystal structure as suggested in Figure 4.6a and 4.6b, then the growing thin film morphology would be undisturbed up to that impurity number fraction. The rapid decrease in mobility with increasing impurity content in this range would then be due to direct increased scattering due to effects of the PnQ defects either within the Pn crystalline lattice or to increased concentration of PnQ at the island boundaries. The latter effect could hinder interconnections between adjacent islands, thus reducing favorable paths for electron conduction[236]. The dramatic increase in the nucleation density of Pn domains above a PnQ number fraction of 0.008 could occur if impurity molecules enhanced critical nucleus formation, e.g. a critical nucleus

might consist of a combination of Pn and PnQ. The increase in nucleation density would occur with increasing probability, as observed, with increasing PnQ content.

Alternatively, the increased nucleation density could be explained as a PnQ-induced reduction in diffusion length for Pn. The mechanism by which this might occur is unclear, however it is known that Pn nucleation is highly sensitive to the surface composition[200, 237, 238]. Finally, increased nucleation could occur if PnQ decoration of growing Pn island edges inhibits incorporation of Pn. This would encourage formation of additional nucleation sites from the unincorporated Pn. The two likely mechanisms for impurity PnQ effects on Pn growth, therefore, will be differentiated by the distribution of PnQ in the film. In one case, PnQ would be distributed relatively uniformly throughout the Pn grains. In the other case, PnQ would be concentrated at the grain boundaries. Phase images revealed no additional information concerning the specific locations of the PnQ molecules. More information, however, can be extracted from detailed analysis of the growth, which will be presented in chapter 5 and elsewhere[233, 239].

In evaluating whether the primary cause of the PnQ induced mobility degradation is due to PnQ effect inside or on the perimeter of grain boundaries, it is useful to evaluate PnQ distributions that would be required for each case. From the inset of Figure 4.1, a linear function can be fit and extrapolated to zero mobility at a number fraction of 0.013 ± 0.004. For the hypothesis that PnQ is uniformly distributed, this would indicate that a single PnQ molecule affects the charge transport of approximately 80 Pn molecules or a circular radius of ~5 Pn molecules, as illustrated in Figure 4.5a. For the alternative hypothesis, where PnQ is located primarily on the grain boundaries, the effect of PnQ will depend on the grain size. A Pn grain area of 0.250 μm^2 corresponds to roughly 5.6×10^5 molecules, with ~3000 molecules at the boundary. A PnQ number fraction of 0.013 then would correspond to a grain surrounded by approximate 2 layers of PnQ, as suggested in Figure 4.6b,

that would effectively no longer transport holes. The real system of course does not reach zero mobility with increasing PnQ, as shown in Figure 4.1b. This may be explained by the result illustrated in Figure 4.3a and Figure 4.3b, that PnQ and Pn effectively separate for high concentrations of PnQ, precluding the complete loss of mobility in either of the limiting-case models discussed. This study cannot differentiate between these two simplistic models but both indicate the relatively large effects of relatively small concentrations of PnQ.

This data reveals three important facts. First, Pn and its primary impurity, PnQ, have phase separated above a PnQ number density ~0.008. The phase-separated materials have very different growth modes (layer-by-layer mode for Pn, *vs*. 3-d growth for PnQ). However, the decrease in Pn mobility with PnQ crystallite volume is more rapid than linear, indicating that chemical segregation cannot be complete at low impurity concentrations. The second fact is that for samples with a small PnQ impurity level, no more than a number fraction of 0.008, Pn thin film growth habits are not measurably affected and similar ultra-thin film and bulk film morphologies are observed for these films. However, strong decreases in mobility are observed in this range, indicating that direct effects of PnQ, rather than changes in grain boundary density, are limiting the mobility. These chemical effects could be in the form of charge traps due to: (i) local potential changes due to individual structural imperfections created by PnQ molecules in the Pn crystalline phase, or (ii) a concentration of PnQ molecules at the natural grain boundaries of Pn thin film structure. The first hypothesis is supported by the recent observation by EFM of charge traps inhomogeneously distributed in Pn films (and not only confined to grain boundaries)[238, 239], and by the observation of strong mobility reductions due to impurities in single crystalline Pn[28]. Finally, strong perturbation of the Pn growth habit is observed above an impurity number fraction of 0.008. In this range, the

continuing strong decreases in mobility reflect some combination of effects of the degraded morphology and impurity scattering.

In summary, we correlated the dependencies of the growth morphology and the field-effect mobility of Pn OTFTs on the percentage of added impurity PnQ present in the source material. The results show that PnQ impurities degrade device performance well before affecting Pn crystal growth habit. Thus improved growth quality alone cannot be used as a predictor of improved device performance.

Chapter 5: Nucleation and Growth of Ultra-thin Pentacene Films*

Pentacenequinone (PnQ) impurities have been introduced into a pentacene source material in a controlled manner to quantify the relative effects of the impurity content on grain boundary structure and thin film nucleation. Atomic force microscopy (AFM) has been employed to directly characterize films grown using 0.0-7.5% PnQ by weight in the source material. Analysis of the distribution of capture zones areas of submonolayer islands as a function of impurity content shows that for large PnQ content the critical nucleus size for forming a Pn island is smaller than for low PnQ content. This result indicates a favorable energy for formation of Pn-PnQ complexes, which in turn suggests that the primary effect of PnQ on Pn mobility may arise from homogeneous distribution of PnQ defects.

* This chapter adapted from: Effect of impurities on pentacene island nucleation
Brad R. Conrad, Elba Gomar-Nadal, William G. Cullen, A. Pimpinelli, T.L. Einstein, Ellen D. Willams, Phys. Rev. B 77, 205328 (2008) doi:10.1103/PhysRevB.77.205328

5.1 Introduction

The study of organic materials, particularly the various roles of morphology and impurity doping, remains an active subject for device physics, materials design, and applied statistical mechanics[201, 240, 241]. Studies of the most promising organic electronic semiconductor, pentacene (Pn), have shown that its transport properties are sensitively dependent on crystalline quality[28, 220] and thin film preparation: for the work here, observations that low concentrations of impurities significantly affect film nucleation and growth, electronic transport, and electronic signal noise are of particular interest [72, 234, 242, 243]. Extensive studies of the initial stages of pentacene film growth [221, 224, 241, 244-247] have shown that it follows the classical picture of nucleation, island growth, aggregation and coalescence that was developed for the growth of inorganic films[248-252]. In later stages of growth, the two-dimensional domains formed from island coalescence serve as the basis for three-dimensional growth due to an Ehrlich-Schwoebel energy barrier that slows diffusion from higher to lower layers of the film [28, 242, 253]. Scaling analysis has proven powerful for evaluating island nucleation and grain boundary formation in such growth systems[249, 251, 252, 254]. In particular, recent investigations using the Wigner surmise, which relates growth processes to universal aspects of fluctuations, have yielded significant improvements in physical understanding[249, 252]. We have measured changes in the capture zone distributions for Pn films grown in the presence of low impurity concentrations, and use the Wigner analysis to demonstrate that the underlying cause is an impurity-induced decrease in the number of molecules required to form a critical nucleus.

5.2 Experiment

The experiments were performed by introducing controlled amounts of the chemical impurity (6,13-pentacenequinone (PnQ)) into pentacene (Pn). The solid

mixtures were prepared by mechanically mixing under a dry nitrogen atmosphere. A series of films were prepared on highly doped Si (100) wafers with 300nm thermally grown oxide pre-cleaned using standard procedures[242] based on many years of experience in preparing atomically cleaned Si samples[255, 256]. The source materials were increased to the deposition temperature (195ºC) over a fifteen minute interval. Deposition was performed at 0.09 Å/s at 10^{-7} Torr pressure, with the substrate at room temperature. The compositions tested covered a range of added PnQ from weight percentage +0.0 to 7.5%, equivalent to added PnQ number fractions ranging from 0.000 to 0.068. The added impurity supplements the natural impurity level of commercial Pn, which is approximately 0.7% by weight or a number fraction of 0.006, as determined previously[28, 242]. To prepare materials with lower impurity content, source material was heated to a temperature slightly lower than its sublimation temperature for at least one hour prior to the thin film deposition.

Previous measurements have shown that this treatment reduces the absolute source PnQ number fraction to less than 0.001 [242] , and yields sample mobilities as high as those obtained with Pn purified using gradient-sublimed material. The source concentration values used to quantify our results are the added number fraction plus the natural impurity level. This represents a readily reproducible quantity, but will not represent the absolute concentration in the thin film, due to the larger sublimation rate of PnQ than Pn at any given source temperature. Two film thicknesses were grown, submonolayer and 50 nm thick, with two different growths for each thickness. The film morphology was characterized using tapping-mode AFM. The islands in the submonolayer thin-films are quantified in image processing

by setting a height threshold to account for substrate height distribution. A limit is also placed on the minimum areal island size to account for image noise. Voronoi polygons (Wigner-Seitz cells) are then calculated from the island nucleation data. For thick films the grain sizes were found by using automated routines to outline the irregularly shaped grains and measure their areas.

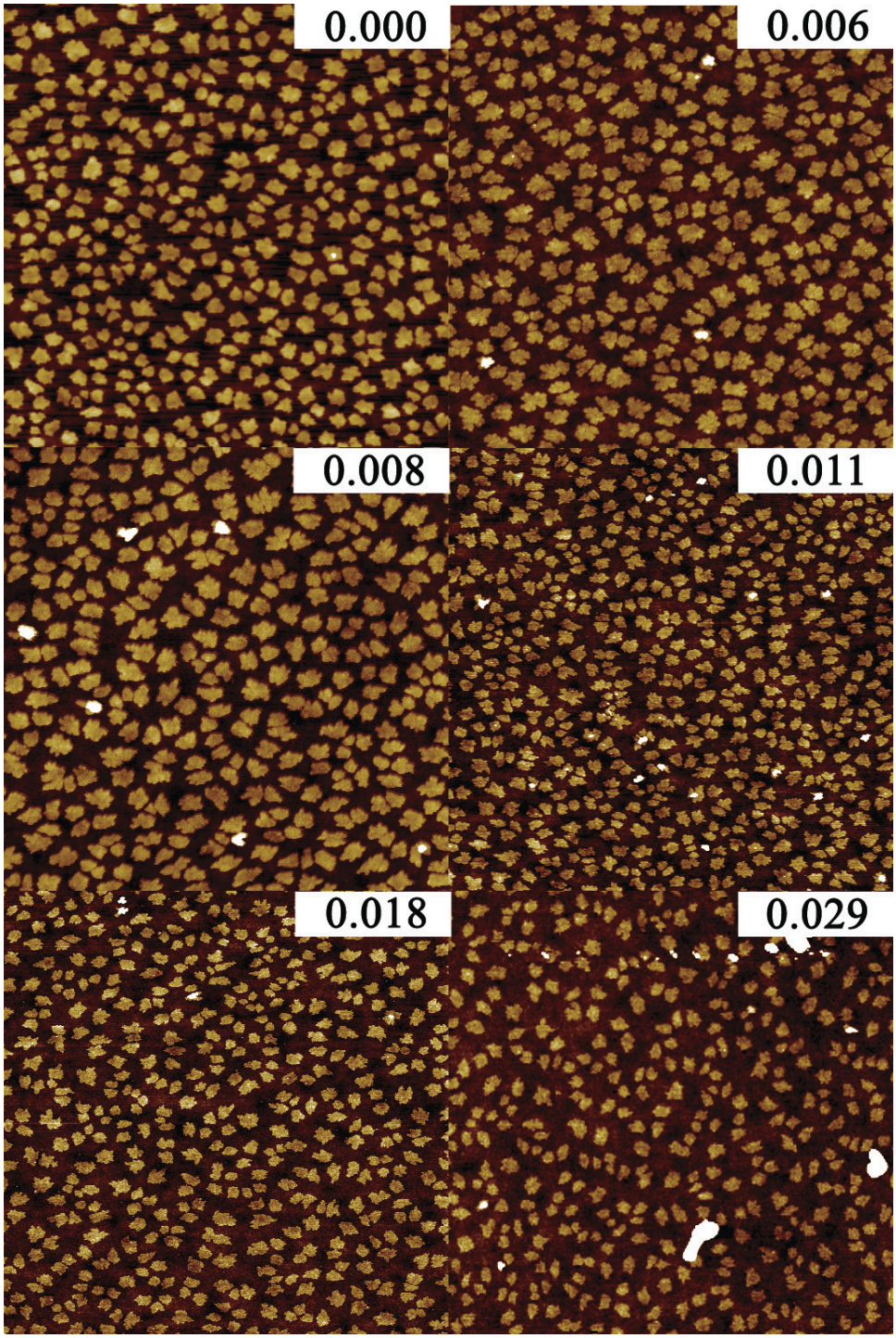

Figure 5.1: AFM images (10 μm x10 μm) of 0.3 ML Pn/PnQ films on SiO_2 with varying source PnQ number fractions.

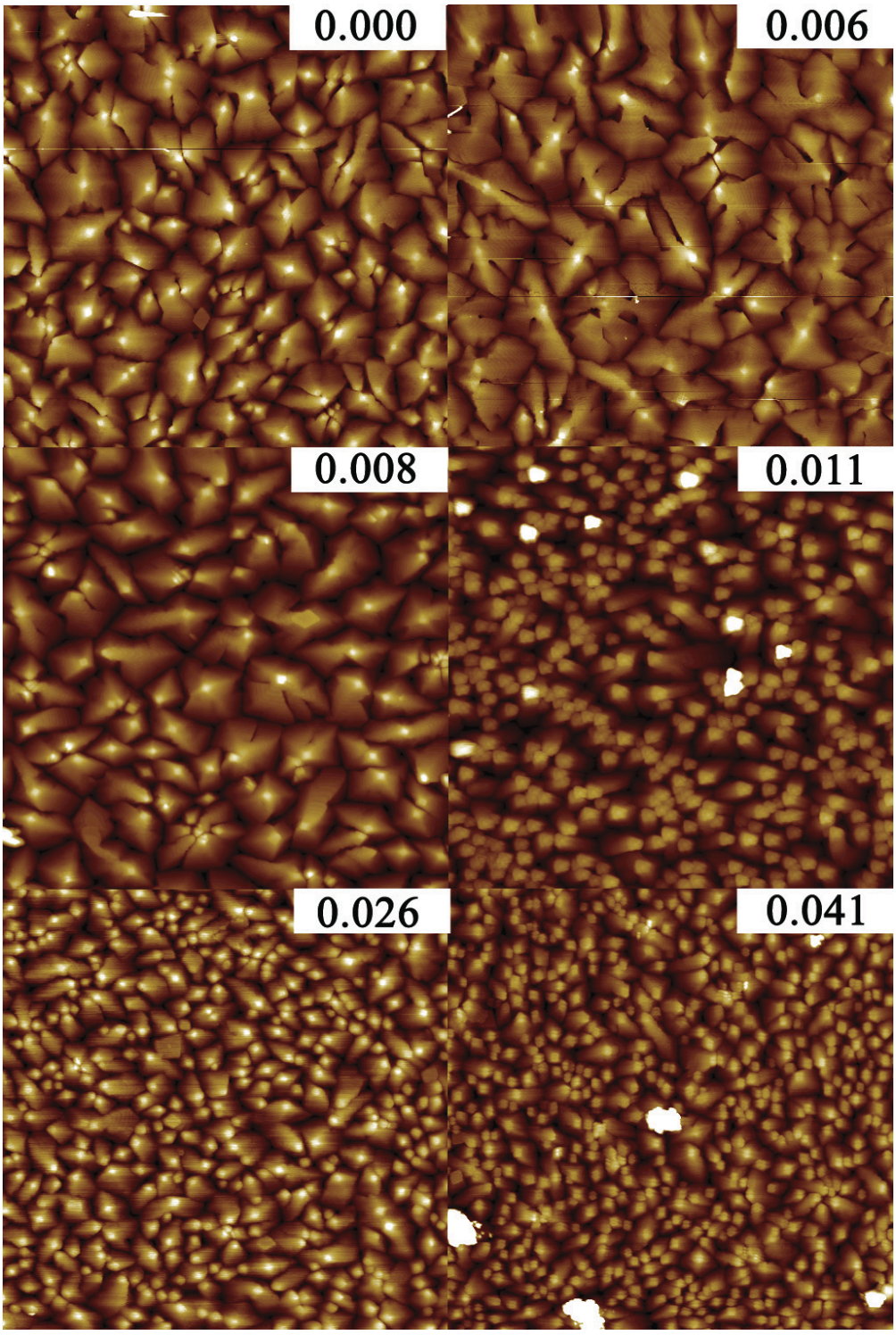

Figure 5.2: AFM images (10 μm x10 μm) of 50 nm Pn/PnQ films on SiO_2 with source materials containing varying PnQ number fractions. Note the varying grain size and morphology.

PnQ Number Fraction	Average Island Area (AIS)	Capture Zone Area (MCZ)	Capture Zone Exponent - β	Island Area Exponent - β	Average Grain Area (AGS)
0.000	0.12±0.06	0.36±0.11	6.8±0.4	3.8±0.2	1.2±0.4
0.006	0.12±0.04	0.30±0.08	6.5±0.4	4.4±0.3	1.2±0.5
0.008	0.12±0.04	0.31±0.09	5.2±0.3	3.6±0.2	1.4±0.5
0.011	0.036±0.016	0.13±0.04	5.3±0.2	3.9±0.2	0.29±0.11
0.018	0.065±0.022	0.22±0.06	4.9±0.2	3.9±0.2	0.29±0.12
0.041	0.068±0.026	0.26±0.08	4.6±0.4	4.1±0.4	0.17±0.07
0.052	0.083±0.029	0.30±0.09	4.9±0.4	4.2±0.4	0.10±0.05

Table 5.1: The average submonolayer island size in μm^2 (AIS), mean capture zone area in μm^2 (MCZ), capture zone distribution Wigner exponent β (CZD-β), the island size distribution Wigner exponent β (ISD-β), and average thick film grain size in μm^2 (AGS) as a function of the number fraction of PnQ.

AFM images of a subset of the prepared submonolayer films as a function of the source number fraction of the PnQ impurity of the source material are shown in Figure 5.1. As the impurity content of the source material is increased, the films display PnQ phase-separation growth, characterized by the appearance of tall islands (that appear as white areas in the AFM images). Previous studies have shown that these tall islands are crystalline PnQ[234, 240, 242, 257]. Sample AFM images of thick films, displayed in Figure 5.2, show that increasing concentration of PnQ during growth causes an abrupt change for PnQ number fractions larger than 0.008 in the ultimate grain sizes and local structure of the bulk film. There is substantial local variation in the shape and sizes of the grains across a sample. The sizes of the pentacene grains were thus measured as averages over three or more images for each deposition and, as Figure 5.4a and Table 5.1 show, both the thick-film average pentacene grain size and the submonolayer average island size decrease abruptly when the impurity concentration reaches a number fraction ~0.008 PnQ. For grain size determination, the tall PnQ growths were excluded. This decrease is concurrent

with large variations in individual grain size as well as the PnQ phase separation shown in Figure 5.2. Substantially decreased electrical transport performance begins well before the observable morphological changes and the region where grain size is decreasing coincides with a further factor-of-four decrease in the material's mobility[242]. Several mechanisms by which impurities could be incorporated into the pentacene film and limit transport have been proposed in the literature, including changes in chemical bonds, disruption of the crystalline structure within a grain, and impurity accumulation at the grain boundaries[224, 225, 242, 258, 259]. In the following, careful analysis of the growth mode changes due to the PnQ is used to help understand where the PnQ resides in the thin films, and thus clarify the mechanism by which PnQ reduces the mobility of the Pn.

5.3 Analysis

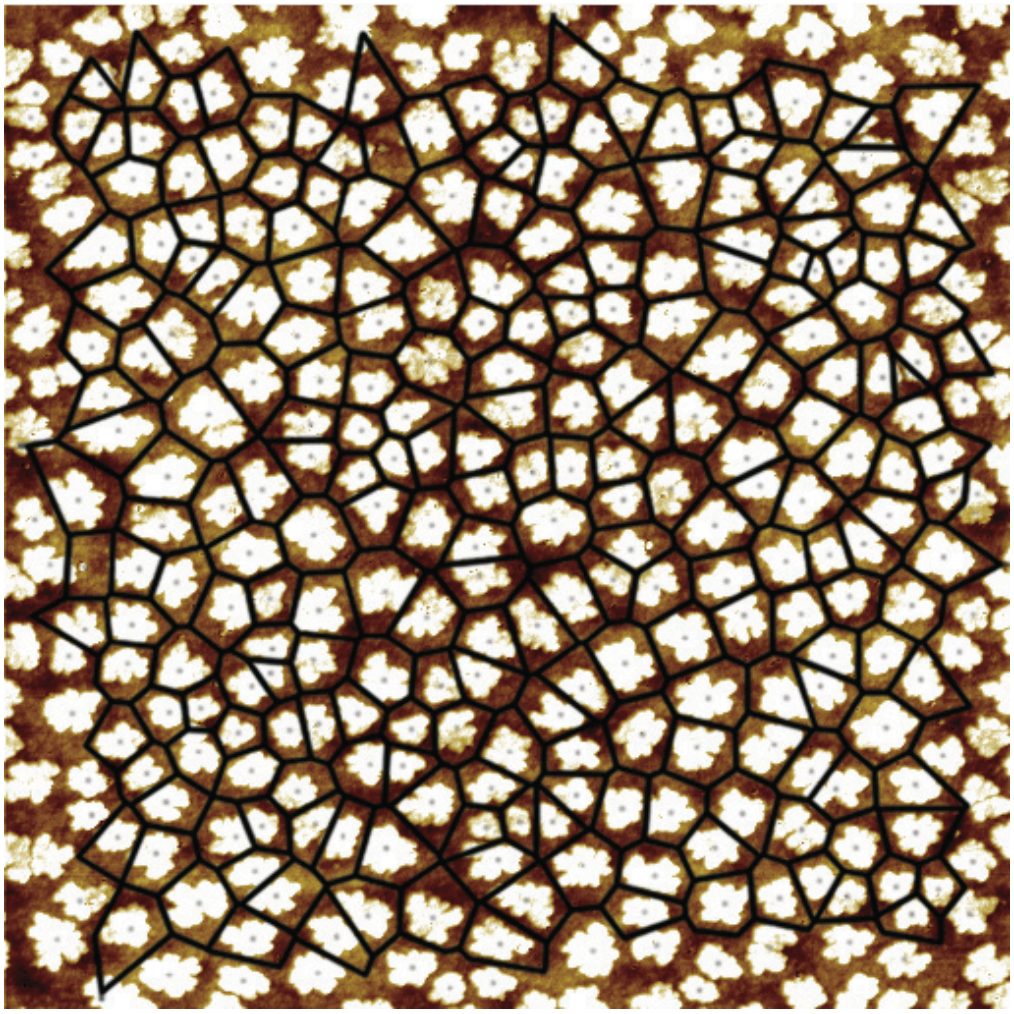

Figure 5.3: An example (10 μm x10 μm) AFM image of commercial Pn. The island centers and Voronoi polygons are indicated by black dots and lines, respectively.

Traditionally, nucleation studies have characterized the evolving submonolayer growth in terms of the island-size distribution (ISD), which under general circumstances has a coverage-insensitive form dependent only on the ratio of the island size to its mean. Another metric monitors the distribution of capture zones (CZ)[240, 249, 260]. These CZs are essentially the proximity (Wigner-Seitz) cells of the islands: the CZ is the number of sites (times the area associated with each) that are closer to the enclosed island than to any other island. Thus, CZs are essentially the areas of Voronoi polygons that are created from the island nucleation points. The

capture zone distribution (CZD) can be similar to the ISD but also may differ even qualitatively, particularly for slow deposition. It was recognized [261-263] over a decade ago that analyzing the CZ distribution (CZD) can be more fruitful than the ISD, which also tends to be more sensitive to deposition rate. Application of the CZ analysis, specified in part in Appendix C, is illustrated in Figure 5.3, which shows a 10 μm x 10 μm AFM image of a 0.3 monolayer commercial pentacene deposition with the centers of the islands and calculated Voronoi polygons indicated by black dots and lines respectively.

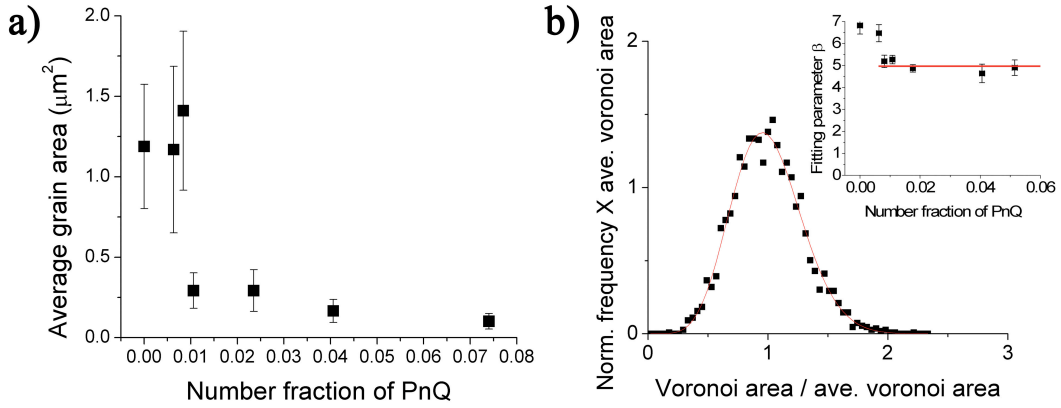

Figure 5.4: a) Average thick film grain area as a function of the number fraction of PnQ content of the source material. b) **An example of the normalized CZ area histogram. The solid line is the generalized Wigner surmise distribution fit with β= 5.27 ± 0.19. The inset is the capture zone fitting parameter ρ as a function of the number fraction of PnQ content of the source material.**

Various formal expressions have been used to characterize the CZD, the simplest of which is a gamma distribution[252, 262-265]. Recently some of us have shown that the generalized Wigner distribution (GWD) accounts for experimental or Monte Carlo data comparably to, if not better than, the gamma distribution and reveals, as described below, fundamentals of the nucleation process[249]. The GWD has the explicit form

$$P_\beta = a_\beta s^\beta \exp\left(-b_\beta s^2\right) \qquad \text{Eq. 5.1}$$

where s is the CZ area normalized by the mean CZ area. The exponent β is the only free parameter, and its value is directly related to the critical nucleus size (see below),

while a_β and b_β are (β-dependent) constants determined by normalization and unit mean, respectively[266]. A representative example of the fit of a CZD by the GWD is shown in Figure 5.4b. The inset of Figure 5.4b and Table 5.1 give the exponent β as a function of the level of source impurity PnQ content. We find β = 4.97 ± 0.26 for the CZD for number fractions between 0.008 and 0.052, indicated by the solid line. The CZDs at lower concentrations of PnQ have exponent β = 6.65 ± 0.26. The width of the distribution[267] $\sigma = \sqrt{(\beta+1)/(2b_\beta)-1}$, follows the opposite trend with σ = 0.260 ± 0.004 for N>0.008 and σ = 0.295 ± 0.007 for N≤0.008. In contrast, if we fit the ISDs with the GWD, the average value of β (and the corresponding width of the distribution) , is insensitive to added impurity content, as summarized in Table 5.1.

In two dimensions the characteristic exponent β = i + 1, where i is the critical nucleus size (i.e., i + 1 is the number of adspecie particles in the smallest stable island). The values of the exponent β, therefore indicate a change in the critical nucleus size, from i ~ 6 when the impurity content is small, to i ~ 4, when the impurity content is large.

In a study of the ISDs of pure Pn films of fractional coverages 0.18 and 0.42, Ruiz et al. found that the ISD of the two overlayer densities collapsed onto a single scaling curve in normalized island size. Using Amar and Family's semiempirical expression[251], they showed that the critical nucleus was decidedly larger than a point island or a dimer. While their distribution was notably noisier than that in our Figure 5.4b, their least-squares fit gave i = 3, to be compared with the value 3.8 ± 0.2 reported in Table 5.1. The comparison is as expected, because the values of i predicted by ISDs are consistently lower than those obtained from CZDs. Both Monte Carlo simulations and experiments, especially those on Pn[245], have shown that the

CZD is more robust than the ISD. Figure 5.3 of Ref. 11 provides a convincing illustration: The CZD is insensitive to the deposition rate (relative to surface diffusion); for rapid deposition of Pn the ISD is comparable to the CZD, but for slower deposition the ISD rises more rapidly to a maximum at smaller normalized size[245]. When fit with the GWD, Eq. 5.1, such behavior corresponds to a smaller value of *i*.

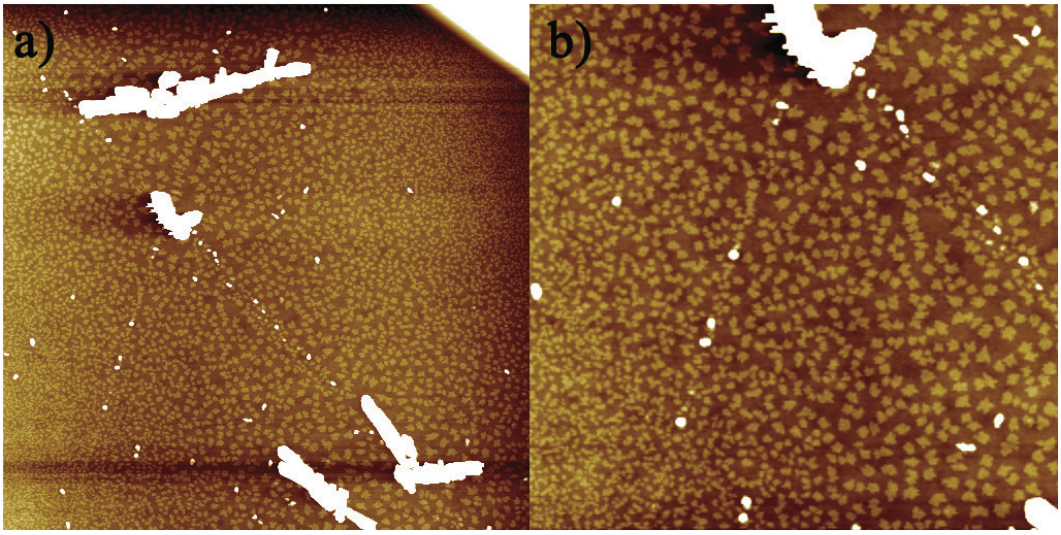

Figure 5.5: a) A (20μm x 20μm) AFM of image of a sample with 3.6Å PnQ deposition followed by a 3.2Å Pn deposition illustrating larger islands near the large topographical features. b) A (10μm x 10μm) zoom-in of Figure 5.5a.

A plausible explanation for the dependence of critical nucleus size on impurity content would be the existence of preferential interaction between PnQ and Pn molecules, allowing small clusters to form with greater stability. This mechanism would be likely to result in the inclusion of a low density of PnQ within the grains of Pn, providing an explanation for the strong decrease in mobility observed at very low number density of PnQ[242], even though the grain boundary distribution has not changed observably. While models for Pn transport have focused on grain boundary defects and impurities[259, 268, 269], impurities within the grain could also cause gap states and thus charge traps[225, 258], or generate hole scattering similar to that

at grain boundaries[259]. Some experimental evidence suggests that trap states are homogeneously distributed in Pn thin films,[270, 271] although no attempt has yet been made to correlate these observations with impurity content.

The stabilization of the critical nucleus size above a PnQ number density of ~0.008 is consistent with the coexistence of a disordered and crystalline phase of PnQ, with an equilibrium density in the disordered phase of ~0.008, as previously reported in chapter 4[242]. The complete absorption of excess PnQ into the crystalline phase would occur when the diffusion length of a PnQ molecule is larger than the separation of PnQ islands. This suggests that sequential, rather than mixed, deposition of Pn and PnQ may directly reveal density-dependent nucleation of islands. Figures 5.5a and 5.5b show a (20μm x 20μm) AFM image and a (10μm x 10μm) enlargement, respectively, of the same image of a film grown by depositing 3.6 Å of PnQ followed by 3.2 Å of Pn. Areas near large PnQ crystallites contain a lower density of larger Pn islands than locations far away from the large PnQ crystallites. This suggests that the nucleation of pure PnQ crystallites lowered the local density of PnQ to the equilibrium density, while areas where PnQ crystallites did not nucleate were left with a local excess of molecular PnQ, which enhanced the nucleation of Pn islands. In addition, it is possible that a preferential interaction between Pn and PnQ would cause Pn near PnQ islands to coat the PnQ crystallites, thus reducing the Pn density available to form islands. It is not possible to differentiate between these two possibilities with the stated series of experiments nor are the effects mutually exclusive.

5.4 Conclusions & Implications

In summary, the morphology of co-deposited submonolayer films has been analyzed in terms of the capture zone and island size distributions. The distributions are well described using the generalized Wigner distribution. The greater sensitivity

of the capture zone distribution to growth processes reveals that the critical nucleus size for Pn island formation decreases for source-PnQ number fractions larger than ~0.006, from $i \sim 6$ (fitting parameter = 5.65 ± 0.25) at lower PnQ density to $i \sim 4$ (fitting parameter = 3.97 ± 0.26), suggesting PnQ enhances the formation of molecular complexes that can serve as nucleation sites. Increased impurity doping primarily results in continued phase-separation with diffusion driven differences in nucleation density.

Chapter 6: Organics on Ultra-thin SiO_2*

Ultra-thin oxide (UTO) films were grown on Si(111) in ultrahigh vacuum at room temperature and characterized by scanning tunneling microscopy. The ultra-thin oxide films were then used as substrates for room temperature growth of pentacene. The apparent height of the first layer is 1.57±0.05 nm, indicating "standing up" pentacene grains in the thin-film phase were formed. Pentacene is molecularly resolved in the second and subsequent molecular layers. The measured in-plane unit cell for the pentacene (001) plane (**ab** plane) is **a**=0.76±0.01 nm, **b**=0.59±0.01 nm, and γ=87.5±0.4º. The films are unperturbed by the UTO's short-range spatial variation in tunneling probability, and reduce its corresponding effective roughness and correlation exponent with increasing thickness. The pentacene surface morphology follows that of the UTO substrate, preserving step structure, the long range surface rms roughness of ~0.1 nm, and the structural correlation exponent of ~1. In addition, C_{60} and sequential C_{60}/pentacene bilayer films are grown on UTOs and characterized with STM.

*This chapter adapted from: Pentacene islands grown on ultra-thin SiO_2, Brad R. Conrad, William G. Cullen, Blake C. Riddick, Ellen D. Willams, Surface Science Letters 603(3); L27-L30 (2009) doi:10.1016/j.susc.2008.12.020

6.1 Introduction

Recent growth in the field of organic semiconductors is indicative of the continued interest in their unique physical and chemical properties [4, 56]. However, limited understanding of electronic transport in these systems, in particular the poorly understood effects of conduction channel morphology at the molecular scale, hinders application development [6, 72, 253]. Due to its robust ordering on a variety of substrates, relatively high mobility, and simple chemical structure, pentacene (Pn) has become the effective benchmark for organic thin film transistors [201] and other applications [272]. For this model organic semiconductor, it is well known that substrate topography, roughness, and trapped charges highly influence growth and morphology, as well as device characteristics [7, 273, 274]. These effects are well documented for the standard substrate used in electronic devices and transport studies, which is SiO_2. Ideally, molecular resolution imaging techniques such as STM would be used to probe the Pn interactions with the SiO_2 substrate, as well as the effects on the Pn crystal structure and morphology. However, tunneling measurements are precluded on dielectric substrates [275]. Here we demonstrate that this problem can be addressed by using ultra-thin layers of SiO_2 on Si as model substrates.

The crystal structure of Pn on an SiO_2 substrate [276-278] is well known. Pn films have also been imaged with molecular resolution on metals [279, 280] and the ultra-thin insulating layers NaCl/Cu(111) [281] and Bi/Si(111) [237, 282]; however, the Pn crystal structure on an insulating oxide surface has not been imaged. To accomplish imaging, we use the approach of current commercial CMOS devices

which utilize an ultra-thin oxide (UTO) approximately as thick as native oxides on the growth substrate [283, 284]. The surfaces of such silicon oxide layers are known to be smooth in comparison with thick SiO_2, because the thin SiO_2 closely follows the morphology of the atomically clean Si substrate precursor [255, 285]. Thus the UTO substrate also allows us to probe the effects of the relative roughness of thin and thick [286] SiO_2 substrate layers on the growth and crystallinity of the Pn films.

6.2 Experiment

The experiments were conducted in an ultrahigh vacuum (UHV) chamber (base pressure ~$4x10^{-11}$ Torr) with a variable temperature Omicron scanning tunneling microscope (STM). The n-doped silicon wafers (<0.1 Ohm-cm) were misoriented by 0.5º toward the [$2\bar{1}\bar{1}$] direction. The Si surface was prepared by several 5s flashes at 1530 K with subsequent cooling at a slow rate (~ 30ºC/min) though the (1x1)-to-(7x7) phase transition. The Si substrate was heated resistively with direct current while the temperature was measured via an infrared pyrometer. The ultra-thin oxide layers were formed by exposing the atomically clean Si(111)-(7x7) to $2.4x10^6$ L of O_2 at room-temperature. The samples were then outgassed at 300ºC in UHV and imaged afterward to confirm oxide quality. The Pn films were grown in an attached chamber at a base pressure <$1x10^{-9}$Torr at a rate of 0.5 ML/min, with flux measured by a water-cooled quartz microbalance (Leybold Inficon). A Pn monolayer is defined by fractional area coverage of a molecular layer of Pn in the thin film phase, with 1 ML in the ordered phase. All STM measurements presented were performed in constant current mode (<40pA) with electrochemically etched tungsten tips and a sample bias of 2.7 to 3.0V.

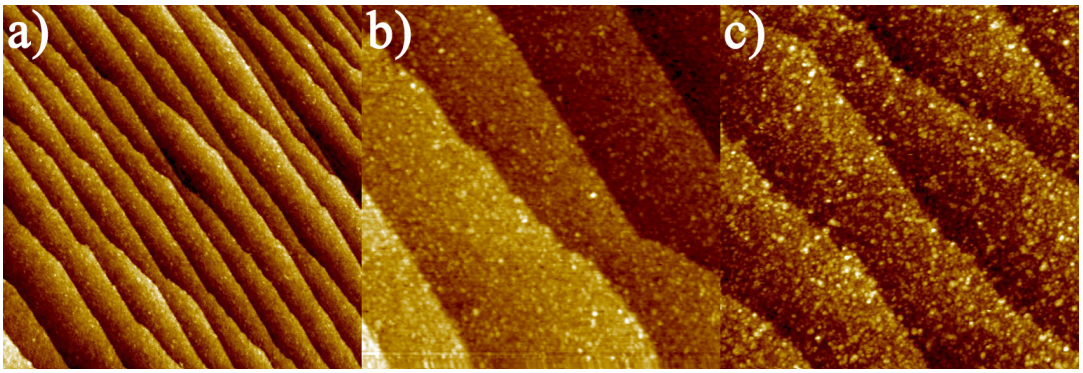

Figure 6.1: a) A $(500nm)^2$ STM image of ultra thin film oxide on a stepped Si(111) surface with a pixel size of 1.25nm measured at room temperature. Single step heights are 0.31 nm. b) A $(100nm)^2$ STM image of ultra thin film oxide on a stepped Si(111) surface with a pixel size of 0.39 nm measured at room temperature. Single step heights are 0.31 nm. c) A $(100nm)^2$ STM image of a continuous pentacene film on a similar ultra thin oxide film.

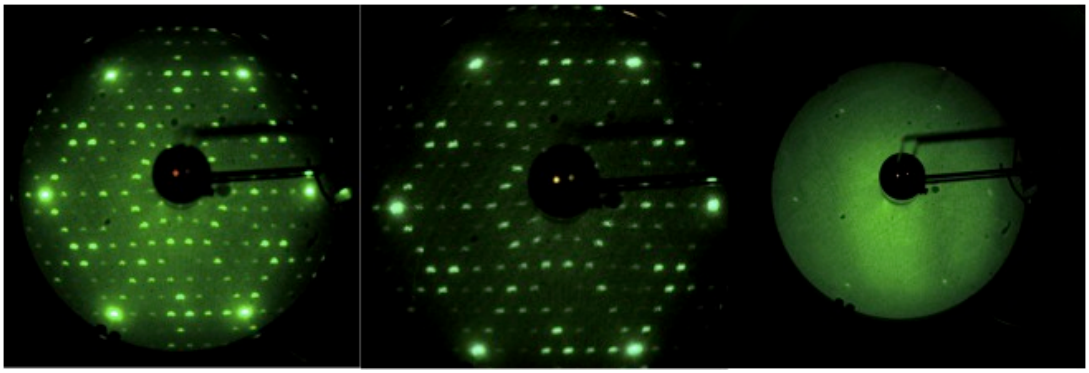

Figure 6.2: Left) Photograph of LEED image of an atomically clean Si(111)-(7x7) sample. The gun voltage was 50meV. Current was 0.3µA. Screen voltage was 4kV. Center) Photograph of LEED image of an partially oxidized Si(111)-(7x7) sample (10seconds at 10^{-1} Torr). Same sample as left image. The gun voltage was 50meV. Current was 0.2µA. Screen voltage was 4kV. Right) Photograph of LEED image of an oxidized Si(111)-(7x7) sample (25seconds at 10^{-1} Torr). Same sample as left and center images. The gun voltage was 76meV. Current was 0.2µA. Screen voltage was 4kV.

Figure 6.1a shows a representative (500nm x 500nm) STM image of the UTO layer. The linear features in the image are single or double atomic silicon steps whose heights, 0.31 nm and 0.63 nm respectively, agree with STM measurements of the clean Si(111). No Si(111)-(7x7) structure can be identified in STM images and low energy electron diffraction (LEED) measurements show no 7x7 reconstruction remaining after exposures larger than $1x10^6$ L of O_2, as seen in the LEED

measurements for progressively larger O_2 exposures in Figure 6.2. This confirms complete oxidation of the surface, and previous work suggests a film up to 1nm thick [287, 288]. Figure 6.1b shows a representative $(500nm)^2$ STM image of the UTO surface. The observed image nonuniformity of the silicon terraces has been reported elsewhere [289, 290], and has been attributed to variations in the interfacial nucleation of the oxide and corresponding variability in the tunnel conductance, rather than variations in surface height [291-293]. This suggests that image nonuniformities are the result of buried oxide islands [293] that represent an increased tunneling barrier thickness. The features always appear as apparent decreases in height, independent of bias voltage, supporting this hypothesis. Furthermore, AFM roughness measurements do not display the topography seen in STM images[294]. When a single layer of Pn is grown on the UTO as shown in the (100nm x 100nm) STM image of Figure 6.1c, the image nonuniformities are similar to those seen on the UTO terraces in Figure 6.1b.

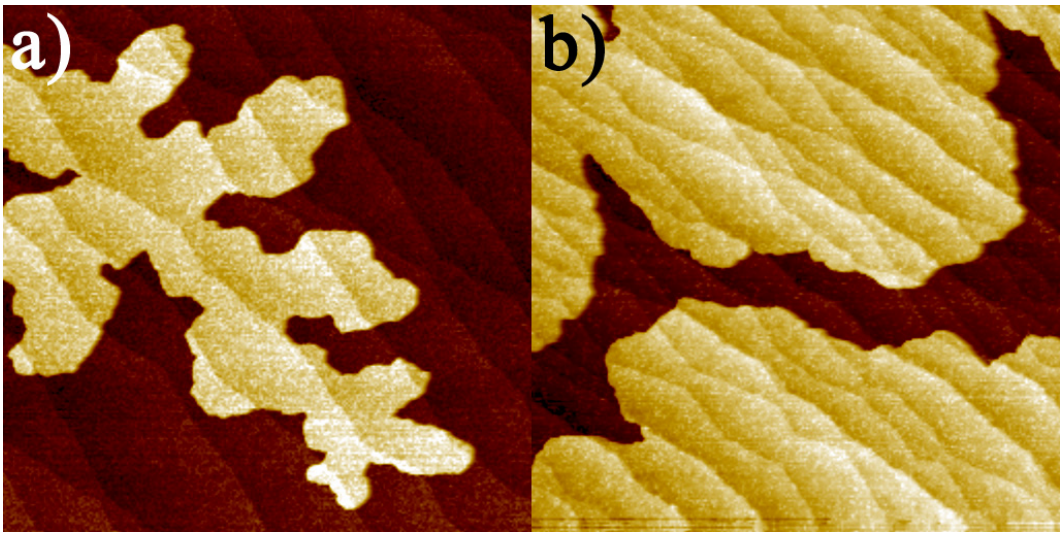

Figure 0.3: a) A (500nm x 500nm) STM image of a pentacene island on an ultra thin film oxide on a stepped Si(111) surface with a pixel size of 1.95 nm measured at room temperature. Single step heights are 0.31 nm on both the oxide and the pentacene island. b) A (500nm x 500nm) STM image of a pentacene grains on a complete pentacene monolayer on a similar ultra thin film oxide with a pixel size of 1.95 nm measured at room temperature. All single step heights are measured to be 0.31 nm.

	Layer height (nm)	a (nm)	b (nm)	γ (°)	Short range RMS roughness (nm)	Short range STM correlation exponent 2H	Long range RMS roughness (nm)*
Oxide	-	-	-	-	0.076 ±0.011	1.60 ±0.03	0.109 ±0.014
Pn 1	1.57 ±0.05	-	-	-	0.060 ±0.001	1.50 ±0.03	-
Pn 2	1.58 ±0.05	0.76 ±0.01	0.59 ±0.01	87.5 ±0.4	0.050 ±0.001	1.38 ±0.03	0.099 ±0.008
Pn 3	1.58 ±0.05	0.76 ±0.01	0.59 ±0.01	87.5 ±0.4	0.050 ±0.002	-	-

Table 6.1: The measured Pn layer height, Pn lattice constants a, b and γ, short scale RMS roughness (L < 30 nm), long scale RMS roughness(L > 300 nm), and 2D correlation exponent 2H for the oxide layer (oxide) as well as the first, second, and third Pn layers (Pn 1, Pn 2, Pn 3). * The long range height roughness exponent is 2H~1.

The initial stage of Pn growth on a UTO film is illustrated in Figure 6.3a, which is an *in situ* (500nm x 500nm) STM image of a thermally grown pentacene island. The height of the first layer pentacene islands is measured to be 1.57±0.05 nm, confirming a "standing-up" configuration mostly normal to the surface, in agreement with Pn thin film phase measurements [7, 273, 295], as shown in Table 6.1. As Figure 6.3a illustrates, the Pn islands exhibit dendritic growth characteristics, which are similar to growth on thicker and rougher SiO_2 substrates [201, 274, 286]. The underlying structure of the stepped Si surface can be seen in the figure as the diagonal linear features and we observe Pn growth to be independent of the steps despite their 0.31 nm height. Figure 6.3b shows a $(500nm)^2$ STM image of an incomplete second layer of Pn. Similar growth structures are observed for second and subsequent Pn layers with increasing three-dimensional growth due to an Ehrlich-Schwoebel-type barrier [201, 274] common in many organic systems [27]. The height of the second and third Pn layers is measured with STM to be 1.58±0.05 nm, equal to that of the first layer as shown in Table 6.1.

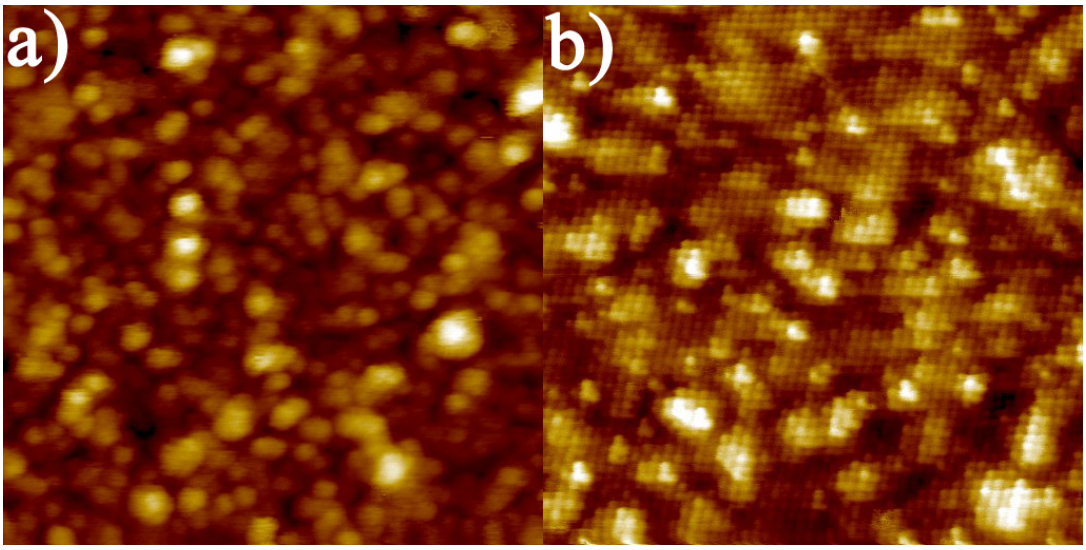

Figure 6.4: a) A (20nm)^2 STM image of a pentacene island on an ultra thin film oxide terrace with a pixel size of 0.04 nm and a height range of 530 pm measured at room temperature. b) A (20nm)^2 STM image of a second monolayer pentacene island on a completed pentacene first layer on a similar ultra thin film oxide terrace with a pixel size of 0.04 nm and a height range of 380 pm measured at room temperature. The peak-to-peak modulation amplitude due to the periodic structure of the pentacene is ~20 pm.

Figure 6.4a shows a higher resolution STM image (20nm x 20nm) of the first layer of Pn showing nonuniformities similar to those seen in Figure 6.1c. Molecular resolution cannot be achieved in the Pn layer in immediate contact with the UTO, independent of tunneling or scanning parameters. The cause could be a disordered first Pn layer or some unidentified electronic coupling between Si/SiO_2 and Pn. However, Figure 6.4b shows a higher resolution STM image (20nm x 20nm) of the second layer of pentacene. A periodic molecular-scale structure can be seen, overlaid with a longer scale light/dark variation similar to the nonuniformity seen in Figures 6.1b, 6.1c and 6.4a. The lattice parameters of the periodic structure were measured from the molecular resolution images such as the (20nm x 20nm) STM image seen in Figure 6.4b. The in-plane unit cell values obtained from several STM measurements are **a**=0.76±0.01 nm, **b**=0.59±0.01 nm, and γ=87.5±0.4º. These measurements confirm that the second layer structure is the Pn(001) plane (**ab** plane) in the thin

film phase, or Pn polymorph IV [7], as is commonly observed in Pn films on thick SiO_2 systems [253, 277, 278].

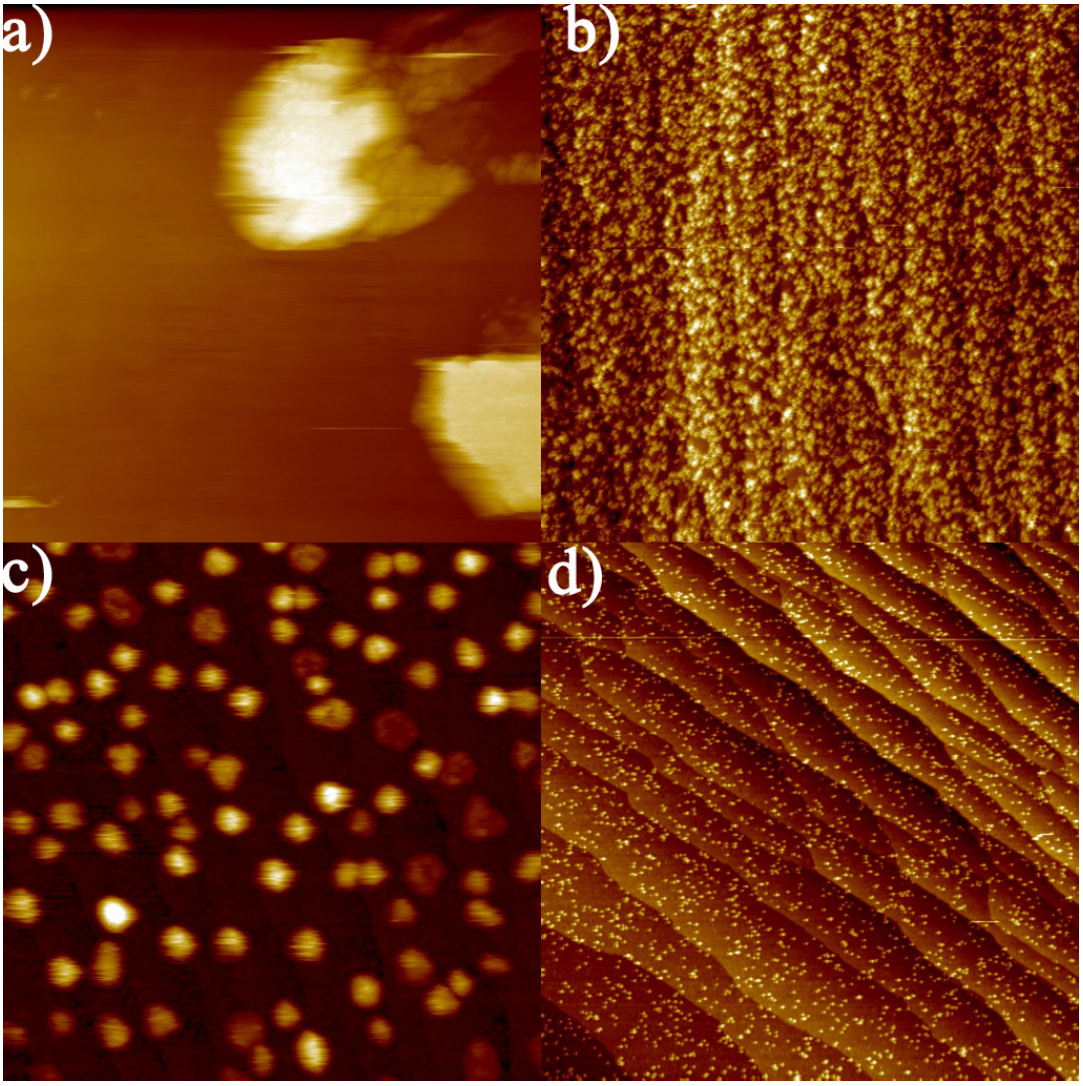

Figure 6.5: a) A (400 nm x 400 nm) STM image of C_{60} islands grown from a 0.9 ML deposition on an ultra thin film oxide, with a pixel size of 0.78 nm and a height range of 13 nm. b) A (400 nm x 400nm) STM image of the film shown in image a) annealed for 15 minutes at 350°C, resulting in an incomplete, disordered single layer C_{60} film. c) A (500 nm x 500nm) STM image of a 0.9 ML C60 deposition on a UTO at 150°C, with a height range ~7 nm. d) A (500 nm x 500nm) STM image of a 0.9 ML C60 deposition on a UTO at 250°C, with a height range ~1.5 nm.

The room temperature growth of C_{60} on UTO films results in the formation of 3D C_{60} crystallites, as shown in the (400 nm x 400 nm) STM image of a 0.9 ML C_{60} deposition at a rate of 0.3ML/min on an ultra thin film oxide of Figure 6.5a. The

deposited C_{60} forms crystallites, shown in Figure 6.5a as amorphous structures ~13 C_{60} high, indicating a strong preference for initial Volmer Weber growth on the bare UTO substrate, similar to C_{60} studies on mica[296]. If the substrate temperature of the film shown in Figure 6.5a is then increased to 350°C for 15 minutes, C_{60} forms an incomplete, disordered single layer C_{60} film shown in the (400 nm x 400 nm) STM image of Figure 6.5b. The virtical lines in the image are single atomic steps of the SiO_2 substrate. Lower annealing temperatures result in the presence of crystallites several molecules high intermixed with regions of an incomplete, disordered single layer of C_{60}. Annealing temperatures between 350°C - 500°C result in smaller density regions of the disordered C_{60} film, indicating material sublimation. For similar 0.9 ML C_{60} depositions at a substrate temperature of 150°C, crystallites with a range of heights form (between 7 and 2 molecules high), as shown in the (500 nm x 500 nm) STM image of Figure 6.5c. If the temperature of the substrate is increased to 250°C for a 0.9 ML deposition a sparse, disordered C_{60} film forms. By comparison, the (500nm x 500nm) STM image of Figure 6.5d with Figure 6.2b shows that substantial C_{60} material has desorbed from the UTO surface.

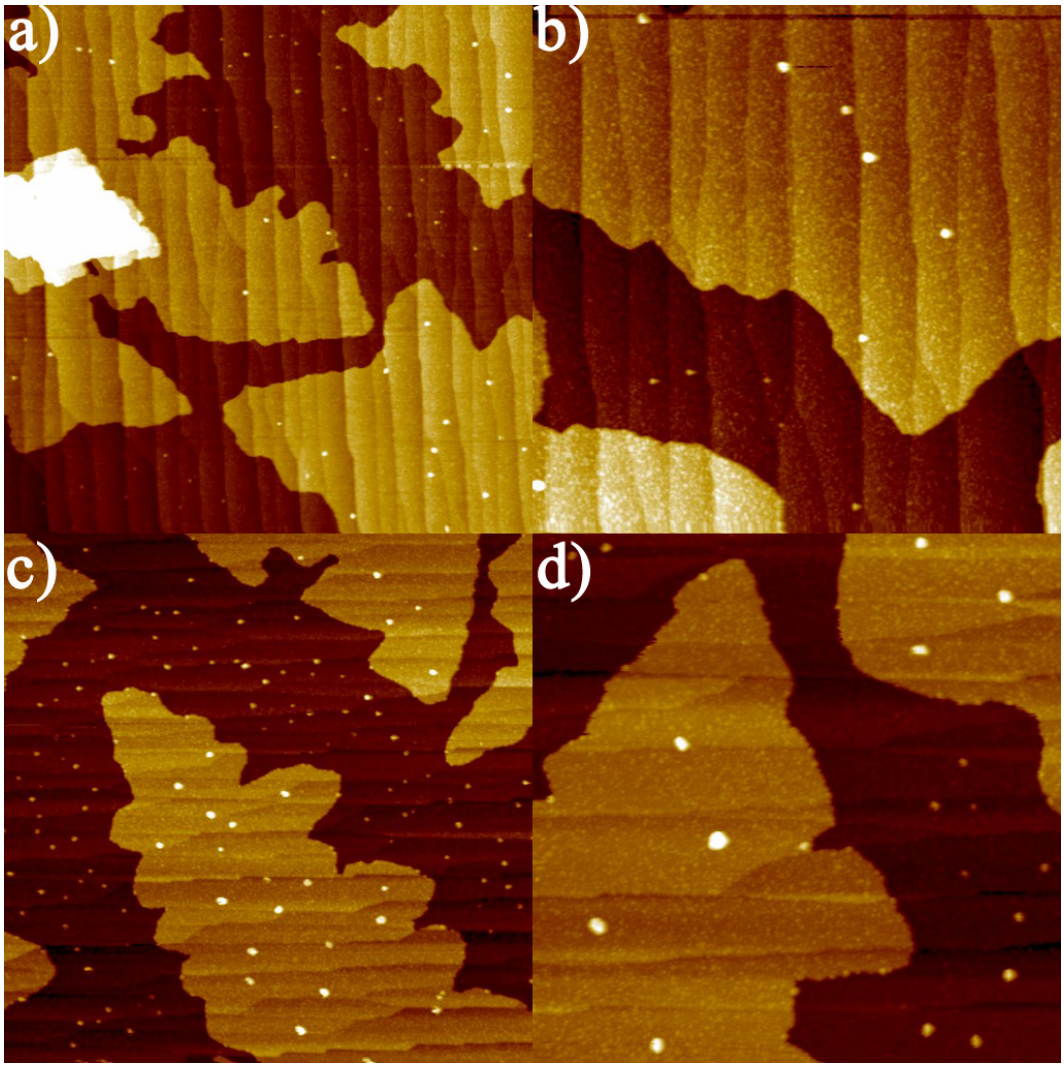

Figure 6.6: a) A (1000nm x 1000nm) STM image of a 0.025 ML C_{60} on 1.6 ML pentacene deposition on a UTO. b) A (500nm x 500nm) STM image of a 0.025 ML C_{60} on 1.6 ML pentacene deposition on a UTO. c) A (1000nm x 1000nm) STM image of a 0.05 ML C_{60} on 1.6 ML pentacene deposition on a UTO. d) A (500nm x 500nm) STM image of a 0.05 ML C_{60} on 1.6 ML pentacene deposition on a UTO.

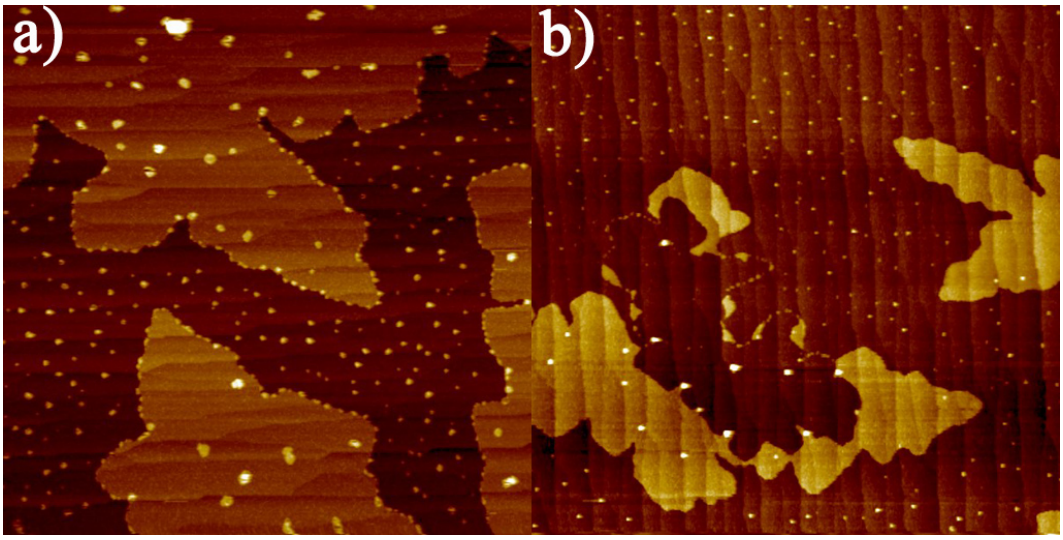

Figure 6.7: a) A (1500nm x 1500nm) STM image of 0.25 ML C_{60} on 1.6 ML pentacene deposition on a UTO. b) A (1000nm x 1000nm) STM image of a 0.044 ML C_{60} on 1.6 ML pentacene deposition on a UTO, annealed at ~130°C for 25 seconds.

In an effort to begin to understand how to model photovoltaic heterojunctions, C_{60} was sequentially deposited on a 1.5ML deposition of pentacene. Figure 6.6a and 6.6b show a (1000nm x 1000nm) and a (500nm x 500nm) STM image of a $1/40^{th}$ ML deposition of C_{60} on 1.6 ML of pentacene on UTO at room temperature. It is observed that C_{60} nucleation begins far from pentacene step edges, forming small 3D crystallites one and two C_{60} high at this coverage for this deposition rate. A larger C_{60} deposition ($1/20^{th}$ ML of C_{60}) on the same pentacene film can be seen in the (1000nm x 1000nm) and (500nm x 500nm) STM images of Figures 6.6c and 6.6d. In contrast to the $1/40^{th}$ ML deposition, for this deposition rate (0.3ML/min) and coverage, C_{60} are observed to decorate the pentacene step edges. It is also observed that the C_{60} crystallites forming on the second layer of pentacene are fewer in number and larger in volume by a factor of 2-4. These trends continue in the 0.25ML C60 deposition on 1.6 ML pentacene on UTO (1500nm x 1500nm) STM image of Figure 6.7a.

Step decoration is observed at higher coverages indicating one possible explanation that step-up pentacene steps effectively act as an extended nucleation site, causing the discrepancy in C_{60} crystallite size. However, since C_{60} crystallites are observed to be fewer in number and larger on bilayer pentacene films far from pentacene step edges (>100nm) in comparison to C_{60} crystallites on single pentacene layers far from step edges (>200nm), it is possible that different diffusion lengths exist for different pentacene layers. Annealing of 0.044 ML C_{60} on 1.6 ML pentacene on UTO films for 25 seconds at 130°C, as seen in the (1000nm x 1000nm) STM image of Figure 6.7b, shows the C_{60} acting as pinning sites for the pentacene step edges as second layer material becomes mobile. No measurable amount of Pn desorption occurs during this annealing process, as Pn coverage over the same remains constant. This C_{60} pinning suggests that cofacial interactions between C_{60}/pentacene are stronger than the Pn-Pn interactions.

6.3 Analysis

The morphology observed by STM can be attributed to variations conductance variations for length scales smaller than a single terrace, and to the density of Si steps for length scales larger than a single terrace. To compare the short and long-range roughness characteristics [297-299], the 2D STM height-height correlation function, $g(r) = \left\langle \left(z(r_o + r) - z(r_o) \right)^2 \right\rangle$, was determined using the STM height measurements z(r) for the atomically clean and Pn-covered UTO surfaces. The correlation functions are observed to behave as $g(r) \sim r^{2H}$ with two separate signatures at large and small length scales. For length scales larger than L = 5 nm, e.g. for image sizes larger than the

average step-step separation, we observe a correlation exponent 2H~1 with a correlation length of ξ=22 ± 2 nm, similar to the long range morphology of Si(111) and thick SiO_2 films [298-301]. Another measure of the surface roughness is the root mean square (RMS) roughness. For images larger than 300nm, which include many terraces, the RMS roughness is 0.109±0.014 nm for the UTO layer and 0.099±0.007 nm for the second layer of Pn, compared with a typical RMS roughness of 0.3 nm for thick SiO_2. This indicates that on the UTO, the long-range roughness is dominated by the Si step density and the over-layers do not develop independent roughness beyond that of the growth substrate.

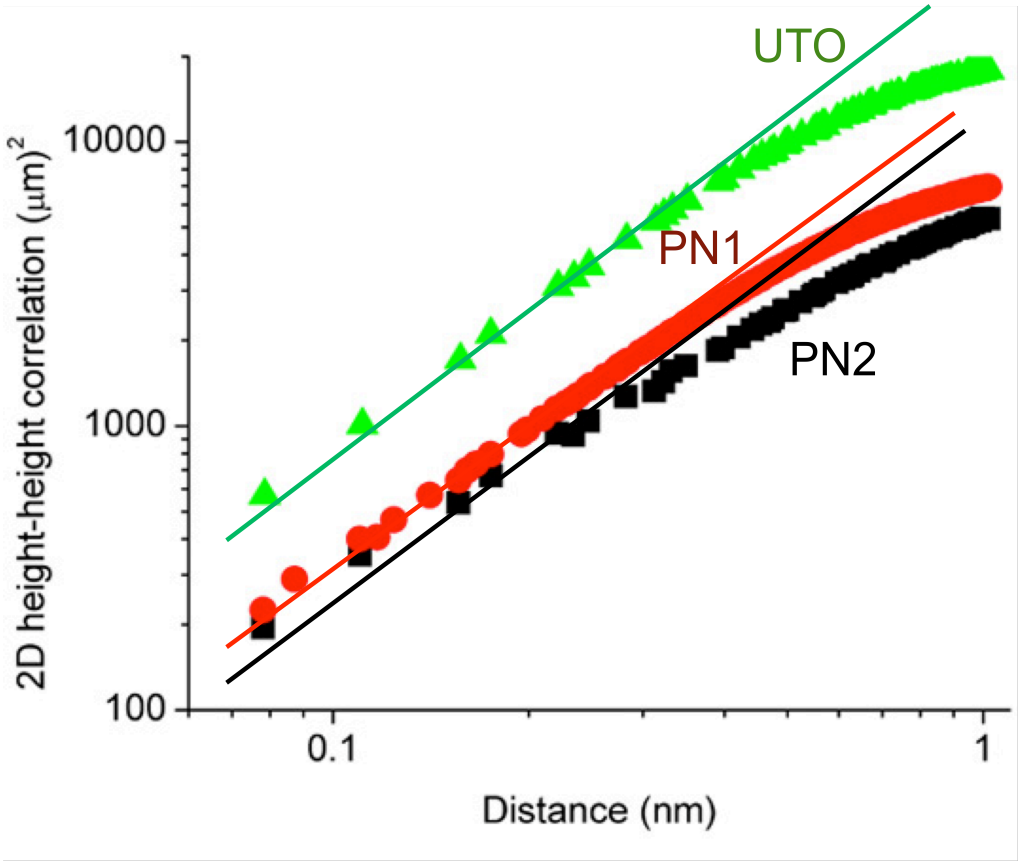

Figure 6.8: **Short range 2D STM correlation functions of a representative UTO, a singly pentacene-covered UTO, and a doubly pentacene-covered UTO. Fits of correlation functions to the functional form $g(r)\sim r^{2H}$ yield short-range STM correlation exponents 2H=1.60±0.03 for the UTO (green triangles), 2H=1.50±0.03 for the first pentacene layer (red circles), and 2H=1.38±0.03 for the second pentacene layer (black squares).**

In contrast to the large-scale analysis, Figure 6.8 shows short-scale (analysis area 40 nm x 40 nm) representative radially averaged 2D STM height-height correlation functions for the UTO terraces, continuous Pn layers on the UTO terraces, and two continuous Pn layers on UTO terraces. At these short length scales the measured 2D STM height-height correlation exponent for individual terraces, as shown in Table 6.1, is larger than at long length scales because measurements are dominated by the apparent height differences due to the short length scale conductance variations on the terraces. The correlation length $\xi = 5.0 \pm 0.5$ nm, for small length scales does not change with Pn thickness, as is expected since the length scale of the nonuniformities does not change with Pn thickness. The short-range STM correlation exponent, $2H = 1.60 \pm 0.03$, is much larger than the long range exponent ($2H \sim 1$), or of the short-range exponent measured using AFM [294]. The apparent decrease of the correlation exponent from $2H = 1.60 \pm 0.03$ for the UTO to $2H = 1.38 \pm 0.03$ for the second layer Pn grain suggests that the Pn over-layers are partially smoothing the conductance variations due to the oxide. The measured short scale, or terrace, RMS roughnesses in Table 6.1 also show a continuous decrease in apparent terrace roughness from 0.076±0.011 nm for the UTO to 0.050±0.002 nm for the third Pn layer despite the observed molecular order, of amplitude ~20 pm, of the second and subsequent Pn films. The conformal growth of the Pn and its ability to shield conductance variations suggests its usefulness as an interlayer on an oxide gate dielectric or electrodes [272].

6.4 Conclusions & Implications

In conclusion, we have imaged and characterized pentacene grown on an ultra-thin silicon oxide film with STM. Pentacene's growth on UTO is qualitatively similar to that on thicker oxides, which indicates that UTO is a useful substrate for studying pentacene as well as other organic semiconductors under conditions relevant to devices. Molecular resolution STM imaging is achieved for a pentacene film on SiO_2 for the first time and the thin film phase crystal structure of the pentacene grains appears at the second layer of growth. C_{60} growth on UTO is investigated as a function of substrate temperature and annealing is examined. The STM-image roughness of the ultra-thin SiO_2 layer is shown to have distinctly different character for long and short length scales. The long scale STM surface roughness is about three times smaller than that of thick oxides, and does not increase with growth of pentacene over-layers, which is conformal. On individual terraces, *e.g.* at short length scales, the apparent surface roughness diminishes as a function of the number of Pn over layers indicating damping of the conduction variation, in contrast to the rigid, conformal growth over substrate steps.

Appendix A: STM Persistence & Survival Analysis

```
pro tanhfn, X, A, F, pder
  z = TANH((X-A[1])/A[2])
; g is used to compute the derivatives
  g = 1/ COSH((X-A[1])/A[2])
  F = A[0]*z+A[3]
;If the procedure is called with four parameters, calculate the
;partial derivatives.
  IF N_PARAMS() GE 4 THEN $
  pder = [[z],[-1*A[0]*g*g/(A[2])], [-1*A[0]*g*g*(-1*X+A[1])/(A[2]*A[2])],
[replicate(1.0, N_ELEMENTS(X))]]
End


pro ExtractEdges, Event
COMMON SHARE1
COMMON SHARE4
WIDGET_CONTROL,Event.top, GET_UVALUE=ImageArr, /NO_COPY
;These must be double since very small numbers are handled
;Define variables initially
;!PIXELX & !PIXELY are pixel sizes in nanometers
X = double(INDGEN(!PIXELX))
XLine = DBLARR(!PIXELX)
```

```
steppos = DBLARR(!PIXELY)

ytmp = FINDGEN(!PIXELX)

;This puts all length scales that get printed in terms of nm

SizeCoefficientX = double(!INCRX)

SizeCoefficientY = double(!INCRY)

;Define v

height = double(0.1)

maxheight = double(0.1)

minheight = double(0.0)

w = DINDGEN(!PIXELX)

maxheight = double(1)

minheight = double(0)

midpoint2 = double(0)

A = double([1, 1, 0.1, 0.1])

oldA1 = double(0.0)

Awander = double(0.0)

;fia: if a variable can be varied, 0=no, 1=yes

fia = [1,1,1,1]

;Open file for printing

OPENW, 17, 'temp_data.txt'

;Calculate the slope of the step estimate

y1 = DOUBLE(!POINT1Y)

x1 = DOUBLE(!POINT1X)
```

```
y2 = DOUBLE(!POINT2Y)

x2 = DOUBLE(!POINT2X

yslope = y2 - y1

; determine slope of two points

If(x1 NE x2) THEN BEGIN

  xslope = x2 - x1

  ENDIF ELSE BEGIN

  xslope = 0.001

Endelse

;Pick the proper slope and round it, figure out xintercept

slope = yslope/xslope

b1 = y1 - x1*slope

xintercept = (-1*b1/slope)

linexpos = FIX(xintercept)

intslope = FIX(slope)

;Make arrays consisting of the values within each horizontal

For j=0, (!PIXELY - 1) Do Begin

  Printf, 17, 'j = ',j, '      '

;  New estimation of Midpoint/ linepos: estimate step position

  linexpos = ROUND((j-y1+x1*(slope))/slope)

;  Line Pre-Processing

  xsub = FINDGEN(linexpos)

  ysub = ImageArr[0:linexpos-1,j]
```

```
   coeffs = LINFIT(xsub,ysub)
   yfit = coeffs[1]*ytmp
   ImageArr[*,j] = ImageArr[*,j] - yfit
;  Get values across one line
   For m = 0, (!PIXELX - 1) Do Begin
         XLine[m] = ImageArr[m,j]
   EndFor
;  Calculate approximate values of A
   maxheight = MAX(XLine)
   minheight = MIN(XLine)
   length = double(N_ELEMENTS(XLine))/2
   height = double(ABS(maxheight - minheight))
   midpoint = double((maxheight - minheight))/2
   midpoint2 = Mean(XLine,/DOUBLE)
;  Define A, note: A[2] is currently just set
   A = double([height, linexpos, 5.0, midpoint2])
;  Fit each line to the curve, get the step position from functional form
;  Define A vector that is initial values of fit function
;  The fn is A0*tanh((x-A1)/A2)-A3
;  A[1] is the center of the fnct and is there by the step edge
;  Leave 'weights' undefined
   Line = CurveFit(X, XLine, weights, A, CHISQ = v, FITA = fia,
Function_Name='tanhfn', ITER = w, ITMAX = 50, /NODERIVATIVE, tol=1e-5)
```

```
   Printf, 17, 'Line = ', Line, '      '
   Print, 'A[1]: ', A[1]
   Printf, 17, "Number of Curvefit Iterations:", w
   Printf, 17, 'The CHISQ was:', v
   Printf, 17, 'Final A = ', A
;  Add an if statement to fix the abrupt change
;  in slope, say 20 units
   IF (j ne 0) THEN BEGIN
     var1 = double(A[1])
     var2 = double(steppos[j-1])
     Awander = ABS( var1 - var2 )
     IF (Awander GT 20) THEN BEGIN
       print, 'There was a step jump of >20'
       steppos[j] = steppos[j-1]
       ENDIF ELSE BEGIN
       steppos[j] = A[1]
     EndELSE
   EndIF ELSE BEGIN
   steppos[j] = A[1]
   EndELSE
   oldA1 = A[1]
   yy = ImageArr[*,j]
```

```
   WINDOW, 29,RETAIN = 2 , XPOS =725 , YPOS =250 , XSIZE = 350, YSIZE =
280, TITLE = 'Fitting Routine'
   plot, ytmp, yy
   oplot, ytmp, Line
   wait, 0.02
;     Assign new values to the original image
      For n = 0, (!PIXELX - 1) Do Begin
        StepImage = BYTSCL(ImageArr)
;       Loop to make the step edge image
        IF (n LT steppos[j]) THEN BEGIN
        ImageArr[n,j] = 0
        ENDIF ELSE BEGIN
        ImageArr[n,j] = 255
        EndELSE
      EndFor
      Printf, 17, 'ImageArr[*,j] = ', ImageArr[*,j]
EndFor
```

Appendix persistence:

```
pro Persistence, Event
;Calculate the persistence probablity
COMMON SHARE4
COMMON SHARE13, CorrCurveP
```

```
;Define variables
nseg=IntArr(cropy)
p=IntArr(cropy)
CorrCurveP=FltArr(cropy)
For i=1, cropy-1 Do Begin
   For j=1, cropy-i-1  Do Begin
      nseg[j]=nseg[j]+1
      n=i
      Repeat Begin
        p[j]=1
        If StepArr[n] GT StepArr[i] Then p[j]=0
        n=n+1
      EndRep Until ((p[j] EQ 0) or (n EQ j+i))
       CorrCurveP[j]=CorrCurveP[j]+p[j]
   EndFor
EndFor
For i=1, cropy-1 Do Begin
  CorrCurveP[i]=CorrCurveP[i]/nseg[i]
EndFor
WINDOW, 6, RETAIN = 2, XPOS=550, YPOS=50, XSIZE = 350, YSIZE = 280,
TITLE = 'Persistence Probablity P'
PLOT, XArr, CorrCurveP, TITLE = 'Persistence Probablity P'
end
```

Appendix Survival:

```
pro Survival, Event
COMMON SHARE4
COMMON SHARE14, CorrCurveS
NStepArr = FLTARR(cropy)
CorrCurveS = FLTARR(cropy)
AvrgX = MEAN(StepArr)
NStepArr = StepArr - AvrgX
For i=1,cropy-1 DO BEGIN
   PointAmount = 0.0
   For j=0, cropy-i-1 DO BEGIN
      JudgeNumber=0
      For k=0, i-1 DO BEGIN
        IF ((NStepArr[j+k] * NStepArr[j+k+1]) LE 0) Then Begin
        JudgeNumber = 1
        GOTO, Jump
        EndIf
      Endfor
      If (JudgeNumber EQ 0) Then PointAmount = PointAmount + 1.0
      Jump:
   Endfor
   CorrCurveS[i] = PointAmount/(cropy-i)
```

```
Endfor
WINDOW, 7,RETAIN = 2 , XPOS=350, YPOS=700, XSIZE = 350, YSIZE = 280,
TITLE = 'Survival Curve S'
PLOT, XArr, CorrCurveS, TITLE = 'Survival Ccurve S'
end
```

Appendix CorrelationFunction:

```
pro CorrelationFunction, Event
COMMON SHARE4
COMMON SHARE10, CorrCurveG
incrx = double(!INCRX)
incry = double(!INCRY)
;Calculate the correlation curve G
;Print, 'cropy', cropy
CorrCurveG=FLTARR(cropy)
For i=1,cropy-1 DO BEGIN
   For j=0, cropy-i-1 DO BEGIN
      CorrCurveG[i] = CorrCurveG[i] + (StepArr[j+i] - StepArr[j])^2
   Endfor
      CorrCurveG[i] = CorrCurveG[i]/(cropy-i)
Endfor
WINDOW, 3,RETAIN = 2 , XPOS=550, YPOS=350, XSIZE = 350, YSIZE = 280,
TITLE = 'Correlation curven G'
```

```
PLOT, XArr, CorrCurveG, TITLE = 'Correlation curve G'
End
```

Appendix DefineLine:

```
pro DefineLine, Event
COMMON SHARE1
COMMON SHARE2
COMMON SHARE3
COMMON SHARE4
;Define 2 point system variables
DEFSYSV, '!POINT1X', '1'
DEFSYSV, '!POINT1Y', '1'
DEFSYSV, '!POINT2X', '1'
DEFSYSV, '!POINT2Y', '1'
WIDGET_CONTROL,Event.top, GET_UVALUE=Rescaled_RoEdgesImage,
/NO_COPY
CURSOR, POINT1X, POINT1Y, 3, /DEVICE
CURSOR, POINT2X, POINT2Y, 4, /DEVICE
;Make point one the lower point and two the upper
If (POINT2Y LT POINT1Y) THEN BEGIN
   PLHDR1 = POINT2Y
   POINT2Y = POINT1Y
   POINT1Y= PLHDR1
```

```
   PLHDR2 = POINT2X
   POINT2X = POINT1X
   POINT1X= PLHDR2
Endif
;Set the System variables
!POINT1X = POINT1X
!POINT1Y = POINT1Y
!POINT2X = POINT2X
!POINT2Y = POINT2Y
Print, '!POINT1X', !POINT1X
Print, '!POINT1Y', !POINT1Y
Print, '!POINT2X', !POINT2X
Print, '!POINT2Y', !POINT2Y
WIDGET_CONTROL, Event.top, SET_UVALUE=Rescaled_RoEdgesImage,
/NO_COPY
end
```

Appendix AreaFlatImage:

```
pro AreaFlatImage, Event
COMMON SHARE1
WIDGET_CONTROL,Event.top, GET_UVALUE=ImageArr, /NO_COPY
CURSOR, LeftLowX, LeftLowY, 3, /DEVICE
CURSOR, RightTopX, RightTopY, 4, /DEVICE
```

```
   If (RightTopX LT LeftLowX) THEN BEGIN
   x = RightTopX
   RightTopX = LeftLowX
   LeftLowX=x
   Endif
   If (RightTopY LT LeftLowY) THEN BEGIN
   y = RightTopY
   RightTopY = LeftLowY
   LeftLowY=y
   Endif
CroppedImg = ImageArr[LeftLowX:RightTopX, LeftLowY:RightTopY]
NewCroppedImg = CONGRID(CroppedImg, pixelx, pixely)
NewFlatImage =ImageArr - SFIT(NewCroppedImg, 1)
TVSCL, NewFlatImage
WIDGET_CONTROL, Event.top, SET_UVALUE=NewFlatImage, /NO_COPY
end
```

Appendix Line Profile:

```
pro Lprofiles, Event
WIDGET_CONTROL,Event.top, GET_UVALUE=ImageArr, /NO_COPY
Profiles, ImageArr
WIDGET_CONTROL, Event.top, SET_UVALUE=ImageArr, /NO_COPY
end
```

Appendix FlatImage:

```
pro FlatImage, Event

WIDGET_CONTROL,Event.top, GET_UVALUE=ImageArr, /NO_COPY

FlImage = ImageArr - SFIT(ImageArr, 1)

TVSCL, FlImage

WIDGET_CONTROL, Event.top, SET_UVALUE=FlImage, /NO_COPY

End
```

Appendix B: Organic Transistor Mask drawings

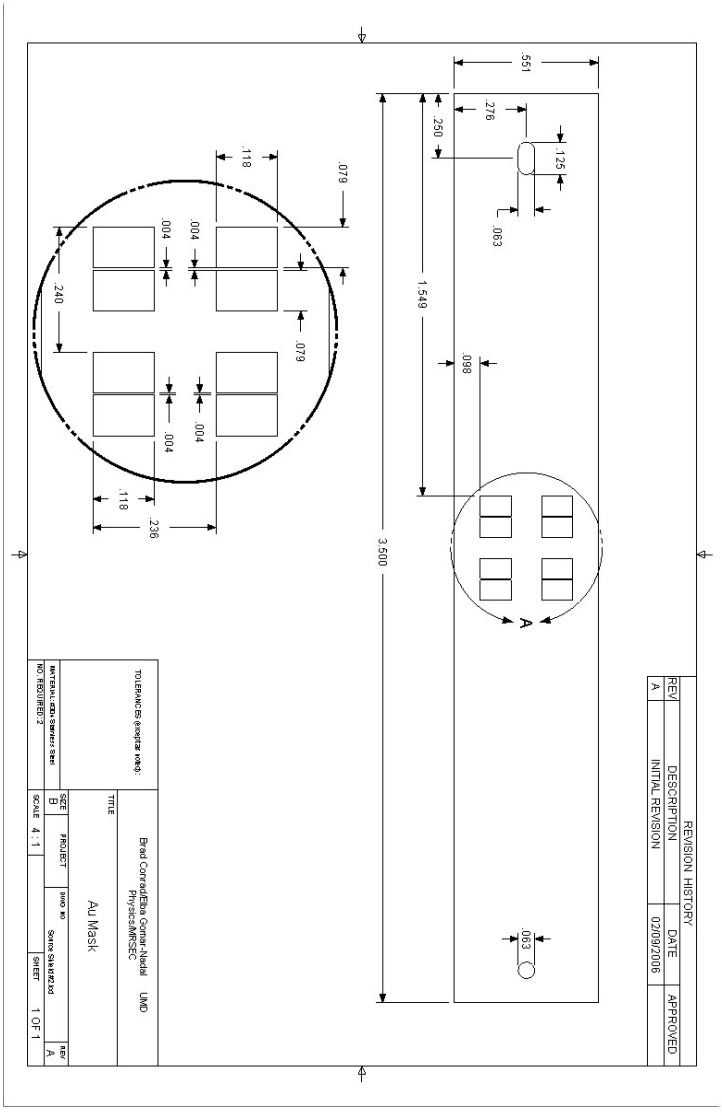

Figure B1: Gold Electrode mask made of 0.006’’ Invar.

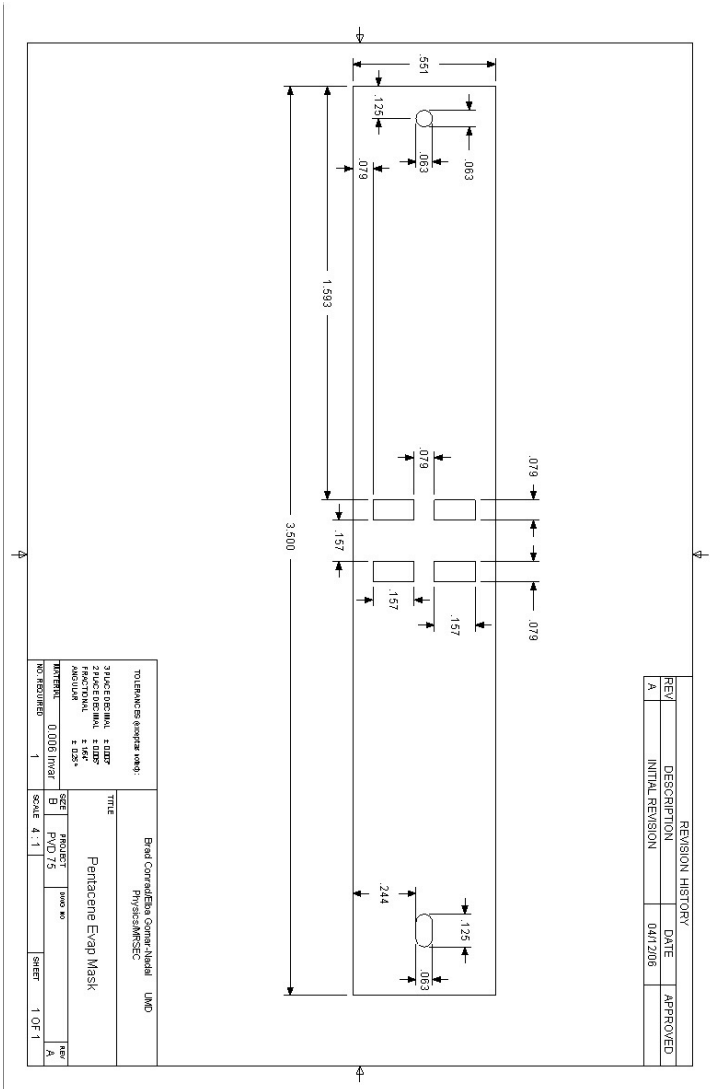

Figure B2: Pentacene conduction channel mask, made of 0.006" Invar.

Appendix C: Island Analysis: Voronoi cells IDL code

```
pro vor, isize

; This program will take a set of 2D points and output capture zone areas and

;images

;isize is the size of the image in um

;ex: 20umx20um image would be enetered vor, 20

; last modified 1/2/08


;Define the data directory

DEFSYSV, '!DATA_DIR', '/home/bconrad/PN/'


;Define variables

Total_Area = 0.00

ext = 0

isizenm = isize*1000


;Create SaveName variable

LongSaveName = DIALOG_PICKFILE(PATH=!DATA_DIR, /READ)

Print, 'data=', LongSaveName

pos1 = STRPOS(LongSaveName, '/PN/')

rawfilename = STRMID(LongSaveName, pos1+4)


Print, "rawfilename=",rawfilename
```

```
;Save data in Spread format
savefolder = '/home/bconrad/PN/saveddata/'
savename = STRCOMPRESS(savefolder + rawfilename + '.txt')
Print,'savename = ', savename

;use this window first, please
SET_PLOT, 'X'
Window, 4, retain = 2, XSIZE = 512, YSIZE = 512
;nevermind, save this one instead
SET_PLOT, 'PS'
vorsavename = STRCOMPRESS(savefolder + rawfilename + '.vor' +'.ps')
;DEVICE, FILENAME=vorsavename, /inches, xsize = 6.0, ysize = 6.0
;plot, [0,isizenm], [0,isizenm], /nodata, XTITLE="Distance (nm)",
YTITLE="Distance (nm)", TITLE = "Voronoi Plot"
DEVICE, FILENAME=vorsavename,  /inches, xsize = 8.0, ysize = 8.0
plot, [0,isizenm], [0,isizenm], /nodata, XSTYLE=4, YSTYLE =4

;read in file
data = READ_ASCII(LongSaveName)

;Print, "X1=", data.field01[25,0]
;Print, "Y1=", data.field01[26,0]
```

```
;Print, "n1=", data.field01[0,0]

;Print, "a1=", data.field01[3,0]

;W = data.field1[0,*]

;X = data.field1[1,*]

;Y = data.field1[2,*]


tIarea = data.field01[2,*]

W = data.field01[0,*]

W = UINT(W)

X = data.field01[32,*]

Y = data.field01[33,*]

Iarea = ABS(TRANSPOSE(tIarea))


;put x and y in terms of a origin of 0,0 system

X = X + isizenm/2

Y = Y + isizenm/2


;sort data, delete duplicate points

GRID_INPUT, X, Y, W, X_Sorted, Y_Sorted, tw_sorted

w_sorted = TRANSPOSE(tw_sorted)


; Triangulate the points:

TRIANGULATE, X_Sorted, Y_Sorted, tr, CONN=C
```

```
N = N_ELEMENTS(X_Sorted)
CZarea = DBLARR(N)
sorted_Iarea = DBLARR(N)
ext_list = INTARR(N)

;Voronoi loop
  FOR I0=0, N-1 DO BEGIN
    VORONOI_B, X_Sorted, Y_Sorted, I0, C, Xp, Yp, rec, ext
    ;capture ext...remember if points are interrior or exterior
    ext_list[I0] = ext
    ;Extra interior/exterior conditions since voronoi does a poor job of it
    N2 = N_ELEMENTS(Xp)
    FOR I1 = 0, N2-1 DO BEGIN
      ;Print, "I1=", I1
      IF Xp[I1] le 0 THEN BEGIN
        ext_list[I0] = UINT(1)
        ;Print, "Xp[",I1,"] is le 0"
      ENDIF
      IF Xp[I1] ge isizenm THEN BEGIN
        ext_list[I0] = UINT(1)
        ;Print, "Xp[",I1,"] is ge isizenm"
      ENDIF
      IF Yp[I1] le 0 THEN BEGIN
```

```
            ext_list[I0] = UINT(1)
            ;Print, "Yp[",I1,"] is le 0"
          ENDIF
          IF Yp[I1] ge isizenm THEN BEGIN
            ext_list[I0] = UINT(1)
            ;Print, "Yp[",I1,"] is ge isizenm"
          ENDIF
        ENDFOR
        ext = ext_list[I0]
        ; Find the Areas:
        A = POLY_AREA(Xp,Yp)
        ;Save the areas in an array
        CZarea[I0] = A
        ; Draw it:
        ;IF EXT eq 0 THEN POLYFILL, Xp, Yp, CLIP=[0,0,isizenm,isizenm], COLOR
= 70+I0*8, THICK=2, /data, NOCLIP=0
        IF EXT eq 0 THEN BEGIN
            PLOTS, Xp, Yp, /data
            PLOTS, Xp, Yp, /data, THICK=6.0, /CONTINUE
        ENDIF
      ENDFOR

;Plot the centers of masses on polyfill graph
```

```
oplot, X_Sorted, Y_Sorted, Psym=3, SYMSIZE=4.0
Device, /CLOSE_FILE
SET_PLOT, 'x'


  FOR I0=0, N-1 DO BEGIN
    ;Find value of zone index in sorted data in position I0
    I1 = w_Sorted[I0]
    ;where is I1 in the unsorted data?
    I2 = WHERE(W EQ I1)
    ;Make a sorted array for Iarea
    ;using the same mapping as GRID_INPUT uses
    sorted_Iarea[I0] = Iarea[I2]
  ENDFOR


;make list of positions, area, etc of interior locations only
M = UINT(Total(ext_list))
P = N-M
Interior_ext = INTARR(P)
Interior_CZarea = DBLARR(P)
N1 = 0
Interior_X = DBLARR(P)
Interior_Y = DBLARR(P)
Interior_I_size = DBLARR(P)
```

```
  FOR I0=0, N-1 DO BEGIN
    IF ext_list[I0] eq 0 THEN BEGIN
      Interior_CZarea[N1] = CZarea[I0]
      Interior_X[N1] = X_Sorted[I0]
      Interior_Y[N1] = Y_Sorted[I0]
      Interior_I_Size[N1] = sorted_Iarea[I0]
      N1 = N1 + 1
    ENDIF
  ENDFOR


Window, 4, retain = 2, XSIZE = 512, YSIZE = 512, title="Interior Voronoi Plot"
plot, [0,isizenm], [0,isizenm], /nodata
plot, X_Sorted, Y_Sorted, Psym=5
Wait, 1
oplot, Interior_X, Interior_Y, Psym = 5, color = 120

;Plot a Histogram in a different window (2):
Window, 2, Retain=2, title="Interior CZ Area Histogram"

;Define an area bin size
binsize = 100000
```

```
;give me the smallest area in long form:
start = long(min(Interior_CZarea)/binsize) * binsize
histog = histogram(Interior_CZarea,binsize=binsize,min=start,max=1000000)

;Find how many elements in density
number_unique = n_elements(histog)

;pad with zeros
vis_histog = fltarr(number_unique+2)
vis_histog(1:number_unique) = histog
xaxis = (findgen(number_unique+2)-.5)*binsize
plot,xaxis,vis_histog,psym=10, XTITLE="Interior CZArea", YTITLE="Frequency
(No units)", /data, title="CZArea Histogram"

;save histogram
SET_PLOT, 'PS'
hsavename = STRCOMPRESS(savefolder + rawfilename + '.hist' +'.ps')
DEVICE, FILENAME=hsavename
plot,xaxis,vis_histog,psym=10, XTITLE="Interior CZArea", YTITLE="Frequency
(No units)", /data, title="CZArea Histogram"
Device, /CLOSE_FILE
SET_PLOT, 'x'
```

```
;Plot Capture Zone Area Vs Island Size
Window, 3, retain = 2, XSIZE = 512, YSIZE = 512, title="Interior Capture Zone
Area Vs. Island Area"
plot, [0,isizenm], [0,isizenm], /nodata
Plot, Interior_I_size, Interior_CZArea, Psym=5, YRANGE=[0,1000000],
XTITLE="Island_Area", YTITLE="CZ_Area", title="Interior Capture Zone Area Vs.
Island Area"

;save capture zone vs island size plot
SET_PLOT, 'PS'
czsavename = STRCOMPRESS(savefolder + rawfilename + '.cz' +'.ps')
DEVICE, FILENAME=czsavename
Plot, Interior_I_size, Interior_CZArea, Psym=5, YRANGE=[0,10000000],
XTITLE="Island_Area", YTITLE="CZ_Area", title="Interior Capture Zone Area Vs.
Island Area"
Device, /CLOSE_FILE
SET_PLOT, 'x'

;save all the data
OpenW, /APPEND, 10, savename
```

```
printf, 10, SYSTIME(0)
;Units: Xpos(nm), Ypos(nm), Interior_I_size(nm^2), Interior_CZArea(nm^2)
printf, 10, '   Xposition   ','   Yposition   ','Island_Size', 'CaptureZoneArea'
  For i = 0, P-1 Do Begin
    printf, 10, Interior_X[i], Interior_Y[i], Interior_I_Size[i], Interior_CZarea[i]
  EndFor
Close, 10
End
```

Bibliography

1. Kelley, T.W., P.F. Baude, C. Gerlach, D.E. Ender, D. Muyres, M.A. Haase, D.E. Vogel, and S.D. Theiss, *Recent Progress in Organic Electronics: Materials, Devices, and Processes.* Chemistry of Materials, 2004. **16**(23): p. 4413-4422.
2. Oliver, M. and T. Jackson, *Energy and economic evaluation of building-integrated photovoltaics.* Energy, 2001. **26**(4): p. 431-439.
3. Gundlach, D.J., *Organic electronics: Low power, high impact.* Nat Mater, 2007. **6**(3): p. 173-174.
4. Gundlach, D.J., J.E. Royer, S.K. Park, S. Subramanian, O.D. Jurchescu, B.H. Hamadani, A.J. Moad, R.J. Kline, L.C. Teague, O. Kirillov, C.A. Richter, J.G. Kushmerick, L.J. Richter, S.R. Parkin, T.N. Jackson, and J.E. Anthony, *Contact-induced crystallinity for high-performance soluble acene-based transistors and circuits.* Nature Materials, 2008. **7**(3): p. 216-221.
5. Conrad, B.R., W.G. Cullen, B.C. Riddick, and E.D. Williams, *Pentacene islands grown on ultra-thin SiO2.* Surface Science, 2009. **603**(3): p. L27-L30.
6. Jurchescu, O.D., B.H. Hamadani, H.D. Xiong, S.K. Park, S. Subramanian, N.M. Zimmerman, J.E. Anthony, T.N. Jackson, and D.J. Gundlach, *Correlation between microstructure, electronic properties and flicker noise in organic thin film transistors.* Applied Physics Letters, 2008. **92**(13): p. 132103.
7. Kitamura, M. and Y. Arakawa, *Pentacene-based organic field-effect transistors.* Journal of Physics-Condensed Matter, 2008. **20**(18): p. 184011
8. Chua, L.-L., J. Zaumseil, J.-F. Chang, E.C.W. Ou, P.K.H. Ho, H. Sirringhaus, and R.H. Friend, *General observation of n-type field-effect behaviour in organic semiconductors.* Nature, 2005. **434**(7030): p. 194-199.
9. Dimitrakopoulos, C.D. and D.J. Mascaro, *Organic thin-film transistors: A review of recent advances.* IBM Journal of Research and Development, 2001. **45**(1): p. 11-27.
10. Kitamura, M. and Y. Arakawa, *Pentacene-based organic field-effect transistors.* Journal of Physics-Condensed Matter, 2008. **20**(18): p. 184011.
11. Gundlach, D.J., J.E. Royer, S.K. Park, S. Subramanian, O.D. Jurchescu, B.H. Hamadani, A.J. Moad, R.J. Kline, L.C. Teague, O. Kirillov, C.A. Richter, J.G. Kushmerick, L.J. Richter, S.R. Parkin, T.N. Jackson, and J.E. Anthony, *Contact-induced crystallinity for high-performance soluble acene-based transistors and circuits.* Nat Mater, 2008. **7**(3): p. 216-221.
12. Buurma, A.J.C., O.D. Jurchescu, I. Shokaryev, J. Baas, A. Meetsma, G.A. de Wijs, R.A. de Groot, and T.T.M. Palstra, *Crystal Growth, Structure, and Electronic Band Structure of Tetracene;TCNQ.* The Journal of Physical Chemistry C, 2007. **111**(8): p. 3486-3489.
13. Chan, C.K., W. Zhao, S. Barlow, S. Marder, and A. Kahn, *Decamethylcobaltocene as an efficient n-dopant in organic electronic materials and devices.* Organic Electronics, 2008. **9**(5): p. 575-581.

14. Pope, M. and C.E. Swenberg, *Processes in Organic Crystals and Polymers*. 1999, New York: Oxford.
15. Katz, H.E., *Recent advances in semiconductor performance and printing processes for organic transistor-based electronics.* Chemistry of Materials, 2004. **16**(23): p. 4748-4756.
16. Klauk, H. and B. Gnade, *An introduction to Organic Semiconductors*, in *Printed Organic and Molecular Electronics*, D. Gamota, et al., Editors. 2004, Kluwer Academic Publishers: Boston.
17. Josowicz, M. and J. Janata, *Suspended gate field effect transistors modified with polypyrrole as alcohol sensor.* Analytical Chemistry, 1986. **58**(3): p. 514-517.
18. Assadi, A., C. Svensson, M. Willander, and O. Inganas, *Field-effect mobility of poly(3-hexylthiophene).* Applied Physics Letters, 1988. **53**(3): p. 195-197.
19. Kepler, R.G., P.E. Bierstedt, and R.E. Merrifield, *Electronic Conduction and Exchange Interaction in a New Class of Conductive Organic Solids.* Physical Review Letters, 1960. **5**(11): p. 503.
20. Helfrich, W. and W.G. Schneider, *Recombination Radiation in Anthracene Crystals.* Physical Review Letters, 1965. **14**(7): p. 229.
21. Kepler, R.G., *Charge Carrier Production and Mobility in Anthracene Crystals.* Physical Review, 1960. **119**(4): p. 1226.
22. Chiang, C.K., C.R. Fincher, Y.W. Park, A.J. Heeger, H. Shirakawa, E.J. Louis, S.C. Gau, and A.G. Macdiarmid, *Electrical-conductivity in DOPED Polyacetylene.* Physical Review Letters, 1977. **39**(17): p. 1098-1101.
23. http://www.sonystyle.com/webapp/wcs/stores/servlet/ProductDisplay?catalogId=10551&storeId=10151&productId=8198552921665327724
24. http://www.physorg.com/news144599565.html
25. Facchetti, A., T. Marks, H.E. Katz, and J. Veinot, *An introduction to Organic Semiconductors*, in *Printed Organic and Molecular Electronics*, D. Gamota, et al., Editors. 2004, Kluwer Academic Publishers: Boston.
26. Carswell, D.J., J. Ferguson, and L.E. Lyons, *Photo-conductance and semi-conductance in molecular single crystals.* Nature, 1954. **173**(4407): p. 736-736.
27. Hlawacek, G., P. Puschnig, P. Frank, A. Winkler, C. Ambrosch-Draxl, and C. Teichert, *Characterization of step-edge barriers in organic thin-film growth.* Science, 2008. **321**(5885): p. 108-111.
28. Jurchescu, O.D., J. Baas, and T.T.M. Palstra, *Effect of impurities on the mobility of single crystal pentacene.* Applied Physics Letters, 2004. **84**(16): p. 3061-3063.
29. Park, S.K., T.N. Jackson, J.E. Anthony, and D.A. Mourey, *High mobility solution processed 6,13-bis(triisopropyl-silylethynyl) pentacene organic thin film transistors.* Applied Physics Letters, 2007. **91**(6): p. 063514.
30. Sakamoto, Y., T. Suzuki, M. Kobayashi, Y. Gao, Y. Fukai, Y. Inoue, F. Sato, and S. Tokito, *Perfluoropentacene: High-performance p-n junctions and complementary circuits with pentacene.* Journal of the American Chemical Society, 2004. **126**(26): p. 8138-8140.

31. Dimitrakopoulos, C.D., A.R. Brown, and A. Pomp, *Molecular beam deposited thin films of pentacene for organic field effect transistor applications.* Journal of Applied Physics, 1996. **80**(4): p. 2501-2508.
32. Anthony, J.E., J.S. Brooks, D.L. Eaton, and S.R. Parkin, *Functionalized Pentacene: Improved Electronic Properties from Control of Solid-State Order.* Journal of the American Chemical Society, 2001. **123**(38): p. 9482-9483.
33. Kroto, H.W., J.R. Heath, S.C. Obrien, R.F. Curl, and R.E. Smalley, *C-60 - Buckminsterfullerene.* Nature, 1985. **318**(6042): p. 162-163.
34. Dresselhaus, M., G. Dresselhaus, and P. Eklund, *Science of Fullerenes and Carbon Nanotubes: Their Properties and Applications*. 1996, New York: Academic Press: Wiley Scientific.
35. Paloheimo, J., H. Isotalo, J. Kastner, and H. Kuzmany, *Conduction mechanisms in undoped thin films of C60 and C60/70.* Synthetic Metals, 1993. **56**(2-3): p. 3185-3190.
36. Park, H., J. Park, A.K.L. Lim, E.H. Anderson, A.P. Alivisatos, and P.L. McEuen, *Nanomechanical oscillations in a single-C60 transistor.* Nature, 2000. **407**(6800): p. 57-60.
37. K. Itaka, M.Y., J. Yamaguchi, M. Haemori, S. Yaginuma, Y. Matsumoto, M. Kondo, H. Koinuma,, *High-Mobility C_{60} Field-Effect Transistors Fabricated on Molecular- Wetting Controlled Substrates.* Advanced Materials, 2006. **18**(13): p. 1713-1716.
38. Varma, C.M., J. Zaanen, and K. Raghavachari, *Superconductivity in the Fullerenes.* Science, 1991. **254**(5034): p. 989-992.
39. Iijima, S., *Helical microtubules of graphitic carbon.* Nature, 1991. **354**(6348): p. 56-58.
40. Li, G., J.M. Liao, G.Q. Hu, N.Z. Ma, and P.J. Wu, *Study of carbon nanotube modified biosensor for monitoring total cholesterol in blood.* Biosensors and Bioelectronics, 2005. **20**(10): p. 2140-2144.
41. Collins, P.G. and P. Avouris, *Nanotubes FOR Electronics.* Scientific American, 2000. **283**(6): p. 62.
42. Yu, M.-F., O. Lourie, M.J. Dyer, K. Moloni, T.F. Kelly, and R.S. Ruoff, *Strength and Breaking Mechanism of Multiwalled Carbon Nanotubes Under Tensile Load.* Science, 2000. **287**(5453): p. 637-640.
43. MacDonald, R.A., C.M. Voge, M. Kariolis, and J.P. Stegemann, *Carbon nanotubes increase the electrical conductivity of fibroblast-seeded collagen hydrogels.* Acta Biomaterialia, 2008. **4**(6): p. 1583-1592.
44. http://news.nationalgeographic.com/news/2006/11/061116-nanotech-swords.html
45. Ayutsede, J., M. Gandhi, S. Sukigara, H. Ye, C.-m. Hsu, Y. Gogotsi, and F. Ko, *Carbon Nanotube Reinforced Bombyx mori Silk Nanofibers by the Electrospinning Process.* Biomacromolecules, 2006. **7**(1): p. 208-214.
46. Dai, H., *Carbon Nanotubes: Synthesis, Integration, and Properties.* Accounts of Chemical Research, 2002. **35**(12): p. 1035-1044.
47. Tans, S.J., A.R.M. Verschueren, and C. Dekker, *Room-temperature transistor based on a single carbon nanotube.* Nature, 1998. **393**(6680): p. 49-52.

48. Novoselov, K.S., A.K. Geim, S.V. Morozov, D. Jiang, Y. Zhang, S.V. Dubonos, I.V. Grigorieva, and A.A. Firsov, *Electric Field Effect in Atomically Thin Carbon Films.* Science, 2004. **306**(5696): p. 666-669.
49. Chen, J.H., C. Jang, S. Adam, M.S. Fuhrer, E.D. Williams, and M. Ishigami, *Charged-impurity scattering in graphene.* Nature Physics, 2008. **4**(5): p. 377-381.
50. Dikin, D.A., S. Stankovich, E.J. Zimney, R.D. Piner, G.H.B. Dommett, G. Evmenenko, S.T. Nguyen, and R.S. Ruoff, *Preparation and characterization of graphene oxide paper.* Nature, 2007. **448**(7152): p. 457-460.
51. Chen, J.H., M. Ishigami, C. Jang, D.R. Hines, M.S. Fuhrer, and E.D. Williams, *Printed graphene circuits.* Advanced Materials, 2007. **19**(21): p. 3623.
52. van den Brink, J., *Graphene: From strength to strength.* Nat Nano, 2007. **2**(4): p. 199-201.
53. Katsnelson, M.I., K.S. Novoselov, and A.K. Geim, *Chiral tunnelling and the Klein paradox in graphene.* Nat Phys, 2006. **2**(9): p. 620-625.
54. Ebisawa, F., T. Kurokawa, and S. Nara, *Electrical properties of polyacetylene/polysiloxane interface.* Journal of Applied Physics, 1983. **54**(6): p. 3255-3259.
55. Pingree, L.S.C., O.G. Reid, and D.S. Ginger, *Electrical Scanning Probe Microscopy on Active Organic Electronic Devices.* Advanced Materials, 2009. **21**(1): p. 19-28.
56. Malliaras, G. and R. Friend, *An organic electronics primer.* Physics Today, 2005. **58**(5): p. 53-58.
57. Pron, A. and P. Rannou, *Processible conjugated polymers: from organic semiconductors to organic metals and superconductors.* Progress in Polymer Science, 2002. **27**(1): p. 135-190.
58. Richard D. McCullough, *The Chemistry of Conducting Polythiophenes.* Advanced Materials, 1998. **10**(2): p. 93-116.
59. Sze, S.M., *Semiconductor Devices: Physics and Technolology*. 1985, New York: John Wiley and Sons.
60. Ashcroft, N. and A. Mermin, *Solid State Physics*. 1976, Ithaca: Brooke/Cole.
61. Redner, S., *A Guide to First-Passage Processes*. 2001, Cambridge: Cambridge University Press.
62. Hajlaoui, R., D. Fichou, G. Horowitz, B. Nessakh, M. Constant, and F. Garnier, *Organic transistors using alpha-octithiophene and alpha,omega-dihexyl-alpha-octithiophene: Influence of oligomer length versus molecular ordering on mobility.* Advanced Materials, 1997. **9**(7): p. 557.
63. Kim, J.Y., K. Lee, N.E. Coates, D. Moses, T.-Q. Nguyen, M. Dante, and A.J. Heeger, *Efficient Tandem Polymer Solar Cells Fabricated by All-Solution Processing.* Science, 2007. **317**(5835): p. 222-225.
64. Shaheen, S.E., D.S. Ginley, and G.E. Jabbour, *Organic-based photovoltaics. toward lowm-cost power generation.* Mrs Bulletin, 2005. **30**(1): p. 10-19.
65. R. J. Tseng, *Anisotropy in Organic Single-Crystal Photovoltaic Characteristics.* Advanced Materials, 2008. **20**(3): p. 435-438.

66. Takeya, J., T. Nishikawa, T. Takenobu, S. Kobayashi, Y. Iwasa, T. Mitani, C. Goldmann, C. Krellner, and B. Batlogg, *Effects of polarized organosilane self-assembled monolayers on organic single-crystal field-effect transistors.* Applied Physics Letters, 2004. **85**(21): p. 5078-5080.
67. Kobayashi, S., T. Nishikawa, T. Takenobu, S. Mori, T. Shimoda, T. Mitani, H. Shimotani, N. Yoshimoto, S. Ogawa, and Y. Iwasa, *Control of carrier density by self-assembled monolayers in organic field-effect transistors.* Nature Materials, 2004. **3**(5): p. 317-322.
68. Walzer, K., B. Maennig, M. Pfeiffer, and K. Leo, *Highly Efficient Organic Devices Based on Electrically Doped Transport Layers.* Chemical Reviews, 2007. **107**(4): p. 1233-1271.
69. Calvin, K.C., K. Antoine, Z. Qing, B. Stephen, and R.M. Seth, *Incorporation of cobaltocene as an n-dopant in organic molecular films.* Journal of Applied Physics, 2007. **102**(1): p. 014906.
70. Jurchescu, O.D., S. Subramanian, R.J. Kline, S.D. Hudson, J.E. Anthony, T.N. Jackson, and D.J. Gundlach, *Organic Single-Crystal Field-Effect Transistors of a Soluble Anthradithiophene.* Chemistry of Materials, 2008. **20**(21): p. 6733-6737.
71. Kelley, T.W. and C.D. Frisbie, *Gate voltage dependent resistance of a single organic semiconductor grain boundary.* Journal of Physical Chemistry B, 2001. **105**(20): p. 4538-4540.
72. Conrad, B.R., W. Yan, W.G. Cullen, and E.D. Williams, *Percolative effects on noise in pentacene transistors.* Applied Physics Letters, 2007. **91**(24): p. 242110.
73. Shockley, W. and G.L. Pearson, *Modulation of Conductance of Thin Films of Semi-Conductors by Surface Charges.* Physical Review, 1948. **74**(2): p. 232.
74. Bardeen, J. and W.H. Brattain, *The Transistor, A Semi-Conductor Triode.* Physical Review, 1948. **74**(2): p. 230.
75. Wang, Y. and M. Lieberman, *Growth of Ultrasmooth Octadecyltrichlorosilane Self-Assembled Monolayers on SiO2.* Langmuir, 2003. **19**(4): p. 1159-1167.
76. Gershenson, M.E., V. Podzorov, and A.F. Morpurgo, *Colloquium: Electronic transport in single-crystal organic transistors.* Reviews of Modern Physics, 2006. **78**(3): p. 973-989.
77. Veres, J., S. Ogier, G. Lloyd, and D. de Leeuw, *Gate insulators in organic field-effect transistors.* Chemistry of Materials, 2004. **16**(23): p. 4543-4555.
78. Lin, Y.Y., D.J. Gundlach, S.F. Nelson, and T.N. Jackson, *Stacked pentacene layer organic thin-film transistors with improved characteristics.* Ieee Electron Device Letters, 1997. **18**(12): p. 606-608.
79. Gundlach, D.J., J.A. Nichols, L. Zhou, and T.N. Jackson, *Thin-film transistors based on well-ordered thermally evaporated naphthacene films.* Applied Physics Letters, 2002. **80**(16): p. 2925-2927.
80. Chang, J.-F., B. Sun, D.W. Breiby, M.M. Nielsen, T.I. Solling, M. Giles, I. McCulloch, and H. Sirringhaus, *Enhanced Mobility of Poly(3-hexylthiophene) Transistors by Spin-Coating from High-Boiling-Point Solvents.* Chemistry of Materials, 2004. **16**(23): p. 4772-4776.

81. Goldmann, C., S. Haas, C. Krellner, K.P. Pernstich, D.J. Gundlach, and B. Batlogg, *Hole mobility in organic single crystals measured by a `flip-crystal'' field-effect technique.* Journal of Applied Physics, 2004. **96**(4): p. 2080-2086.
82. Lawrence, D., J. Kohler, B. Brollier, T. Claypole, and T. Burgin, *Manufacturing Platforms for Printing Organic Circuits*, in *Printed Organic and Molecular Electronics*, D. Gamota, et al., Editors. 2004, Kluwer Academic Publishers: Boston.
83. Hines, D.R., V.W. Ballarotto, E.D. Williams, Y. Shao, and S.A. Solin, *Transfer printing methods for the fabrication of flexible organic electronics.* Journal of Applied Physics, 2007. **101**(2): p. 024503.
84. Laudise, R.A., C. Kloc, P.G. Simpkins, and T. Siegrist, *Physical vapor growth of organic semiconductors.* Journal of Crystal Growth, 1998. **187**(3-4): p. 449-454.
85. Takeya, J., C. Goldmann, S. Haas, K.P. Pernstich, B. Ketterer, and B. Batlogg, *Field-induced charge transport at the surface of pentacene single crystals: A method to study charge dynamics of two-dimensional electron systems in organic crystals.* Journal of Applied Physics, 2003. **94**(9): p. 5800-5804.
86. de Boer, R.W.I., T.M. Klapwijk, and A.F. Morpurgo, *Field-effect transistors on tetracene single crystals.* Applied Physics Letters, 2003. **83**(21): p. 4345-4347.
87. Gundlach, D.J., M.S. Shur, T. Jackson, J. Kanicki, S. Martin, A. Dodabalapur, and B. Crone, *Electrical Behavior of Organic Transistors and Curcuits*, in *Printed Organic and Molecular Electronics*, D. Gamota, et al., Editors. 2004, Kluwer Academic Publishers: Boston.
88. Gundlach, D.J., L. Zhou, J.A. Nichols, T.N. Jackson, P.V. Necliudov, and M.S. Shur, *An experimental study of contact effects in organic thin film transistors.* Journal of Applied Physics, 2006. **100**(2): p. 024509.
89. Crispin, X., V. Geskin, A. Crispin, J. Cornil, R. Lazzaroni, W.R. Salaneck, and J.L. Bredas, *Characterization of the interface dipole at organic/metal interfaces.* Journal of the American Chemical Society, 2002. **124**(27): p. 8131-8141.
90. Salaneck, W.R., S. Stafstrom, and J.L. Bredas, *Conjugated Polymer Surfaces and Interfaces*. 1996, Cambridge: Cambridge University Press.
91. Baldo, M.A. and S.R. Forrest, *Interface-limited injection in amorphous organic semiconductors.* Physical Review B, 2001. **64**(8): p. 17.
92. Cowley, A.M. and S.M. Sze, *Surface States and Barrier Height of Metal-Semiconductor Systems.* Journal of Applied Physics, 1965. **36**(10): p. 3212-3220.
93. Scott, J.C. and G.G. Malliaras, *Charge injection and recombination at the metal-organic interface.* Chemical Physics Letters, 1999. **299**(2): p. 115-119.
94. Scott, J.C., *Metal-organic interface and charge injection in organic electronic devices.* Journal of Vacuum Science & Technology A, 2003. **21**(3): p. 521-531.
95. Koch, N., A. Elschner, J. Schwartz, and A. Kahn, *Organic molecular films on gold versus conducting polymer: Influence of injection barrier height and*

morphology on current--voltage characteristics. Applied Physics Letters, 2003. **82**(14): p. 2281-2283.
96. Kymissis, I., C.D. Dimitrakopoulos, and S. Purushothaman, *High-performance bottom electrode organic thin-film transistors.* Electron Devices, IEEE Transactions on, 2001. **48**(6): p. 1060-1064.
97. Watkins, N.J., L. Yan, and Y. Gao, *Electronic structure symmetry of interfaces between pentacene and metals.* Applied Physics Letters, 2002. **80**(23): p. 4384-4386.
98. Gowrisanker, S., Y. Ai, M.A. Quevedo-Lopez, H. Jia, H.N. Alshareef, E. Vogel, and B. Gnade, *Impact of semiconductor/contact metal thickness ratio on organic thin-film transistor performance.* Applied Physics Letters, 2008. **92**(15): p. 153305-3.
99. de Boer, R.W.I., M. Jochemsen, T.M. Klapwijk, A.F. Morpurgo, J. Niemax, A.K. Tripathi, and J. Pflaum, *Space charge limited transport and time of flight measurements in tetracene single crystals: A comparative study.* Journal of Applied Physics, 2004. **95**(3): p. 1196-1202.
100. de Boer, R.W.I. and A.F. Morpurgo, *Influence of surface traps on space-charge limited current.* Physical Review B, 2005. **72**(7): p. 073207.
101. Hill, I.G., A. Rajagopal, A. Kahn, and Y. Hu, *Molecular level alignment at organic semiconductor-metal interfaces.* Applied Physics Letters, 1998. **73**(5): p. 662-664.
102. Veres, J., S.D. Ogier, S.W. Leeming, D.C. Cupertino, and S.M. Khaffaf, *Low-k insulators as the choice of dielectrics in organic field-effect transistors.* Advanced Functional Materials, 2003. **13**(3): p. 199-204.
103. Hamadani, B.H., C.A. Richter, J.S. Suehle, and D.J. Gundlach, *Insights into the characterization of polymer-based organic thin-film transistors using capacitance-voltage analysis.* Applied Physics Letters, 2008. **92**(20): p. 203303-3.
104. Torsi, L., A. Dodabalapur, and H.E. Katz, *An analytical model for short-channel organic thin-film transistors.* Journal of Applied Physics, 1995. **78**(2): p. 1088-1093.
105. Junk, A. and F. Riess, *From an idea to a vision: There's plenty of room at the bottom.* American Journal of Physics, 2006. **74**(9): p. 825-830.
106. Davisson, C. and L. Germer, *The Scattering of Electrons by a Single Crystal of Nickel.* Nature, 1927. **119**: p. 558-560.
107. Ertl, G., M. Weiss, and S.B. Lee, *Role of Potassium in the Catalytic Synthesis of Ammonia.* Chemical Physics Letters, 1979. **60**(3): p. 391-394.
108. Weiss, M., G. Ertl, and F. Nitschke, *Adsortpion and Decomposition of Ammonia on Fe(110).* Applied Surface Science, 1979. **2**(4): p. 614-635.
109. Grunze, M., F. Bozso, G. Ertl, and M. Weiss, *Interaction of Ammonia with Fe(111) and Fe(100) Surfaces.* Applied Surface Science, 1978. **1**(2): p. 241-265.
110. Rayment, T., R. Schlogl, J.M. Thomas, and G. Ertl, *Structure of the Ammonia-Synthesis Catalyst.* Nature, 1985. **315**(6017): p. 311-313.
111. Ertl, G., D. Prigge, R. Schloegl, and M. Weiss, *Surface characterization of Ammonia-Synthesis Catalysts.* Journal of Catalysis, 1983. **79**(2): p. 359-377.

112. Ertl, G., *primary steps in catalytic synthesis of Ammonia.* Journal of Vacuum Science & Technology a-Vacuum Surfaces and Films, 1983. **1**(2): p. 1247-1253.
113. Ertl, G. and M. Huber, *Mechanism and kentics of ammonia decomposition on Iron.* Journal of Catalysis, 1980. **61**(2): p. 537-539.
114. Ertl, G., *Oscillatory kinetics and spatiotemporal self-organization in reactions at solid-surfaces.* Science, 1991. **254**(5039): p. 1750-1755.
115. Rotermund, H.H., W. Engel, M. Kordesch, and G. Ertl, *Imaging of spatiotemporal pattern evolution during Carbon-monoxide oxidation on Platinum.* Nature, 1990. **343**(6256): p. 355-357.
116. Ertl, G., P.R. Norton, and J. Rustig, *Kinetic Oscillations in the platinum-catalyzed oxidation of CO.* Physical Review Letters, 1982. **49**(2): p. 177-180.
117. Ertl, G., Untersuchung *von Oberflachenreaktionen mittels beugung Lansamer Elktronen (LEED) .I. Wechselwirkung von O_2 und N_2O mit (110)-(111)-und (100)-kupfer-oberflachen.* Surface Science, 1967. **6**(2): p. 208.
118. Brune, H., J. Wintterlin, J. Trost, G. Ertl, J. Wiechers, and R.J. Behm, *Interaction of oxygen with Al(111) studied by scanning tunneling microscopy.* Journal of Chemical Physics, 1993. **99**(3): p. 2128-2148.
119. Bao, X., J.V. Barth, G. Lehmpfuhl, R. Schuster, Y. Uchida, R. Schlogl, and G. Ertl, *oxygen-induced restructuring og Ag(111).* Surface Science, 1993. **284**(1-2): p. 14-22.
120. Binning, G., H. Rohrer, C. Gerber, and E. Weibel, *surfaces Studied by scanning tunneling microscopy.* Physical Review Letters, 1982. **49**(1): p. 57-61.
121. Binnig, G., H. Rohrer, C. Gerber, and E. Weibel, *7x7 Reconstruction on Si(111) Resolved in Real Space.* Physical Review Letters, 1983. **50**(2): p. 120.
122. Takayanagi, K., Y. Tanishiro, S. Takahashi, and M. Takahashi, *Structure analysis of Si(111)-7 ◊ 7 reconstructed surface by transmission electron diffraction.* Surface Science, 1985. **164**(2-3): p. 367-392.
123. Vanderbilt, D., *Absence of large compressive stress on Si(111).* Physical Review Letters, 1987. **59**(13): p. 1456.
124. Eastman, D.E., *Geometrical and electronic structure of Si(001) and Si(111) surfaces: A status report.* Journal of Vacuum Science and Technology, 1980. **17**(1): p. 492-500.
125. Miller, D.J. and D. Haneman, *Evaluation of recent Si(111)-(7 x 7) surface models.* Surface Science, 1981. **104**(2-3): p. L237-L244.
126. Phillips, J.C., *New Model for Reconstructed Si(111)- 7x7 Surface Superlattices.* Physical Review Letters, 1980. **45**(11): p. 905.
127. Lagally, M.G., *Transition from reciprocal-space to real-space surface science---advent of the scanning tunneling microscope.* Journal of Vacuum Science & Technology A: Vacuum, Surfaces, and Films, 2003. **21**(5): p. S54-S63.
128. Sakurai, J.J., *Modern Quantum Mechanics Revised Edition*, ed. S. Tuan. 1994, New York: Addison Wesley Publishing.
129. Bardeen, J., *Tunnelling from a Many-Particle Point of View.* Physical Review Letters, 1961. **6**(2): p. 57.

130. Chen, C.J., *Introduction to Scanning Tunneling Microscopy*. 1993.
131. Tersoff, J. and D.R. Hamann, *Theory of the scanning tunneling microscope.* Physical Review B, 1985. **31**(2): p. 805.
132. Giaever, I., *Energy Gap in Superconductors Measured by Electron Tunneling.* Physical Review Letters, 1960. **5**(4): p. 147.
133. Tersoff, J. and D. Lang, eds. *Theory of Scanning Tunneling Microscopy*. Scanning Tunneling Microscopy, ed. J. Stroscio and W. Kaiser. Vol. 1. 1994, Academic Press: New York.
134. Maksymovych, P., D.B. Dougherty, X.Y. Zhu, and J.J.T. Yates, *Nonlocal Dissociative Chemistry of Adsorbed Molecules Induced by Localized Electron Injection into Metal Surfaces.* Physical Review Letters, 2007. **99**(1): p. 016101-4.
135. Burton, W.K., N. Cabrera, and F.C. Frank, *The Growth of Crystals and the Equilibrium Structure of Their Surfaces.* Philosophical Transactions of the Royal Society of London Series a-Mathematical and Physical Sciences, 1951. **243**(866): p. 299-358.
136. Chernov, A.A., *Layer-Spiral Growth of Crystals.* Uspekhi Fizicheskikh Nauk, 1961. **73**(2): p. 277-331.
137. Gruber, E.E. and W.W. Mullins, *On Theory of Anisotropy of Crystalline Surface Tension.* Journal of Physics and Chemistry of Solids, 1967. **28**(5): p. 875-&.
138. Pimpinelli, A. and J. Villain, *Physics of Crystal Growth*. 1998, Cambridge: Cambridge University Press.
139. Giesen, M., *Step and island dynamics at solid/vacuum and solid/liquid interfaces.* Progress in Surface Science, 2001. **68**(1-3): p. 1-153.
140. Merikoski, J., J. Maunuksela, M. Myllys, J. Timonen, and M.J. Alava, *Temporal and spatial persistence of combustion fronts in paper.* Physical Review Letters, 2003. **90**(2).
141. Rapapa, N.P. and A.J. Bray, *Effect of shear on persistence in coarsening systems.* Physical Review E, 2006. **73**(4).
142. Tam, W.Y., R. Zeitak, K.Y. Szeto, and J. Stavans, *First-passage exponent in two-dimensional soap froth.* Physical Review Letters, 1997. **78**(8): p. 1588-1591.
143. Biham, O., J. Krug, A. Lipshtat, and T. Michely, *Reaction kinetics in a tight spot.* Small, 2005. **1**(5): p. 502-504.
144. Lipshtat, A. and O. Biham, *Efficient simulations of gas-grain chemistry in interstellar clouds.* Physical Review Letters, 2004. **93**(17).
145. Zhirnov, V.V. and R.K. Cavin, *Molecular Electronics: Chemistry of molecules or physics of contacts?* Nature Materials, 2006. **5**: p. 11-12.
146. Hwang, C.O. and J.A. Given, *Last-passage Monte Carlo algorithm for mutal capacitance.* Physical Review E, 2006. **74**(1): p. 027701
147. Dougherty, D.B., *Experimental studies of fluctuations and transport at solid surfaces* in *Physics*. 2004, University of Maryland: College Park, Maryland. p. 264.

148. Einstein, A., *On the movement of small particles suspended in stationary liquids required by the molecular-kinetic theory of heat.* Annalen der Physik, 1905(17): p. 549-560.
149. Smoluchowski, S.V., Ann. Phys. (Leipzig), 1906(21): p. 765.
150. Langevin, P., Comptes Rend Acad. Sci. Paris, 1908(146): p. 530.
151. Jeong, H.C. and E.D. Williams, *Steps on surfaces: experiment and theory.* Surface Science Reports, 1999. **34**(6-8): p. 175-294.
152. Majumdar, S.N., A.J. Bray, and G. Ehrhardt, *Persistence of a continuous stochastic process with discrete-time sampling.* Physical Review E, 2001. **6401**(1).
153. Wong, G.P., R.W. Mair, R.L. Walsworth, and D.G. Cory, *Measurement of persistence in 1D diffusion.* Physical Review Letters, 2001. **86**(18): p. 4156-4159.
154. Yurke, B., A.N. Pargellis, S.N. Majumdar, and C. Sire, *Experimental measurement of the persistence exponent of the planar Ising model.* Physical Review E, 1997. **56**(1): p. R40-R42.
155. Constantin, M., *Persistence and survival aspects of fluctuation phenomena in surfaces, in Physics. 2005,* University of Maryland: College Park, Maryland. p. 183.
156. Constantin, M. and S. Das Sarma, *Generalized survival in equilibrium step fluctuations.* Physical Review E, 2004. **69**(5).
157. Constantin, M., S. Das Sarma, and C. Dasgupta, *Spatial persistence and survival probabilities for fluctuating interfaces.* Physical Review E, 2004. **69**(5).
158. Constantin, M., C. Dasgupta, P.P. Chatraphorn, S.N. Majumdar, and S. Das Sarma, *Persistence in nonequilibrium surface growth.* Physical Review E, 2004. **69**(6).
159. Dasgupta, C., M. Constantin, S. Das Sarma, and S.N. Majumdar, *Survival in equilibrium step fluctuations.* Physical Review E, 2004. **69**(2).
160. Dougherty, D.B., O. Bondarchuk, M. Degawa, and E.D. Williams, *Persistence exponents for step edge diffusion.* Surface Science, 2003. **527**(1-3): p. L213-L218.
161. Dougherty, D.B., I. Lyubinetsky, E.D. Williams, M. Constantin, C. Dasgupta, and S.D. Sarma, *Experimental persistence probability for fluctuating steps.* Physical Review Letters, 2002. **89**(13).
162. Dougherty, D.B., C. Tao, O. Bondarchuk, W.G. Cullen, E.D. Williams, M. Constantin, C. Dasgupta, and S. Das Sarma, *Sampling-time effects for persistence and survival in step structural fluctuations.* Physical Review E, 2005. **71**(2).
163. Majumdar, S.N. and A.J. Bray, *Spatial persistence of fluctuating interfaces.* Physical Review Letters, 2001. **86**(17): p. 3700-3703.
164. Majumdar, S.N., A.J. Bray, S.J. Cornell, and C. Sire, *Global persistence exponent for nonequilibrium critical dynamics.* Physical Review Letters, 1996. **77**(18): p. 3704-3707.

165. Majumdar, S.N. and C. Dasgupta, *Spatial survival probability for one-dimensional fluctuating interfaces in the steady state.* Physical Review E, 2006. **73**(1).
166. Pathria, R.K., *Statistical Mechanics*. 2 ed. 1999, Oxford: Butterworth-Heinemann.
167. Bantu, H.G., *Terrace Width Distribution and First Passage Probabilities for Interacting Steps*, in *Physics*. 2005, University of Maryland: College Park, Maryland. p. 89.
168. Pimpinelli, A., J. Villain, D.E. Wolf, J.J. Metois, J.C. Heyraud, I. Elkinani, and G. Uimin, *Equilibrium Step Dynamics on Vicinal Surfaces.* Surface Science, 1993. **295**(1-2): p. 143-153.
169. Williams, E.D., R.J. Phaneuf, J. Wei, N.C. Bartelt, and T.L. Einstein, *Thermodynamics and Statistical-Mechanics of the Faceting of Stepped Si(111).* Surface Science, 1993. **294**(3): p. 219-242.
170. Ihle, T., C. Misbah, and O. Pierre-Louis, *Equilibrium step dynamics on vicinal surfaces revisited.* Physical Review B, 1998. **58**(4): p. 2289-2309.
171. Khare, S.V. and T.L. Einstein, *Unified view of step-edge kinetics and fluctuations.* Physical Review B, 1998. **57**(8): p. 4782-4797.
172. Krug, J., H. Kallabis, S.N. Majumdar, S.J. Cornell, A.J. Bray, and C. Sire, *Persistence exponents for fluctuating interfaces.* Physical Review E, 1997. **56**(3): p. 2702-2712.
173. Stanley, A.-L.B.a.H.E., *Fractal Concepts in Surface Growth*. 1995, Cambridge: Cambridge University Press.
174. Constantin, M., S. Das Sarma, C. Dasgupta, O. Bondarchuk, D.B. Dougherty, and E.D. Williams, *Infinite family of persistence exponents for interface fluctuations.* Physical Review Letters, 2003. **91**(8).
175. Kallabis, H. and J. Krug, *Persistence of Kardar-Parisi-Zhang interfaces.* Europhysics Letters, 1999. **45**(1): p. 20-25.
176. Majumdar, S.N., *Persistence in nonequilibrium systems.* Current Science, 1999. **77**(3): p. 370-375.
177. Lyubinetsky, I., D.B. Dougherty, T.L. Einstein, and E.D. Williams, *Dynamics of step fluctuations on a chemically heterogeneous surface of Al/Si(111)-(root 3x root 3).* Physical Review B, 2002. **66**(8).
178. Blagojevic, B. and P.M. Duxbury, *Atomic diffusion, step relaxation, and step fluctuations.* Physical Review E, 1999. **60**(2): p. 1279-1291.
179. Flynn, C.P., *Step-edge fluctuations on crystal surfaces.* Physical Review B, 2002. **66**(15).
180. Dougherty, D.B., I. Lyubinetsky, T.L. Einstein, and E.D. Williams, *Distinguishing step relaxation mechanisms via pair correlation functions.* Physical Review B, 2004. **70**(23).
181. Pang, N.N., Y.K. Yu, and T. Halpinhealy, *Interfacial Kinetic Roughening with Correlated Noise.* Physical Review E, 1995. **52**(3): p. 3224-3227.
182. Bartelt, N.C., T.L. Einstein, and E.D. Williams, *The influence of step-step interactions on step wandering.* Surface Science Letters, 1990. **240**(3): p. L591.

183. Lyubinetsky, I., D.B. Dougherty, H.L. Richards, T.L. Einstein, and E.D. Williams, *Step wandering on Al/Si(111)-(root 3 x root 3) surface at high temperatures.* Surface Science, 2001. **492**(1-2): p. L671-L676.
184. Michely, T., M.C. Reuter, and R.M. Tromp, *Al on Si(111): Phase diagram and atomic mechanisms.* Physical Review B, 1996. **53**(7): p. 4105-4108.
185. Kramtsova, E.A., A.V. Zotov, A.A. Saranin, S.V. Ryzhkov, and A.B. Liftshits, Appl. Surf. Sci., 1994. **82/83**: p. 576.
186. Bondarchuk, O., D.B. Dougherty, M. Degawa, E.D. Williams, M. Constantin, C. Dasgupta, and S. Das Sarma, *Correlation time for step structural fluctuations.* Physical Review B, 2005. **71**(4).
187. Hooge, F.N., *1/F Noise Is No Surface Effect.* Physics Letters, 1969. **A 29**(3): p. 139-140.
188. Hooge, F.N., *1/F Noise Sources.* IEEE Transactions on Electron Devices, 1994. **41**(11): p. 1926-1935.
189. Marinov, O., M.J. Deen, and B. Iniguez, *Charge transport in organic and polymer thin-film transistors: recent issues.* IEE Proceedings-Circuits Devices and Systems, 2005. **152**(3): p. 189-209.
190. Planes, J. and A. Francois, *Percolation scaling, inhomogeneity, and defects in polyaniline blends: A 1/f noise diagnosis.* Physical Review B, 2004. **70**(18).
191. Ferrari, G., D. Natali, M. Sampietro, F.P. Wenzl, U. Scherf, C. Schmitt, R. Guntner, and G. Leising, *Current noise spectroscopy on mLPPP based organic light emitting diodes.* Organic Electronics, 2002. **3**(1): p. 33-42.
192. Sampietro, M., G. Ferrari, D. Natali, U. Scherf, K.O. Annan, F.P. Wenzl, and G. Leising, *Tracking of conduction phenomena and degradation in organic light emitting diodes by current noise measurements.* Applied Physics Letters, 2001. **78**(21): p. 3262-3264.
193. Necliudov, P.V., S.L. Rumyantsev, M.S. Shur, D.J. Gundlach, and T.N. Jackson, *1/f noise in pentacene organic thin film transistors.* Journal of Applied Physics, 2000. **88**(9): p. 5395-5399.
194. Vandamme, L.K.J., R. Feyaerts, G. Trefan, and C. Detcheverry, *1/f noise in pentacene and poly-thienylene vinylene thin film transistors.* Journal of Applied Physics, 2002. **91**(2): p. 719-723.
195. Martin, S., A. Dodabalapur, Z. Bao, B. Crone, H.E. Katz, W. Li, A. Passner, and J.A. Rogers, *Flicker noise properties of organic thin-film transistors.* Journal of Applied Physics, 2000. **87**(7): p. 3381-3385.
196. Ke, L., X.Y. Zhao, R.S. Kumar, and S.J. Chua, *Low-frequency noise measurement and analysis in organic light-emitting diodes.* IEEE Electron Device Letters, 2006. **27**(7): p. 555-557.
197. Ruiz, R., A. Papadimitratos, A.C. Mayer, and G.G. Malliaras, *Thickness dependence of mobility in pentacene thin-film transistors.* Advanced Materials, 2005. **17**(14): p. 1795.
198. Horowitz, G., *Organic thin film transistors: From theory to real devices.* Journal of Materials Research, 2004. **19**(7): p. 1946-1962.
199. Mayer, A.C., R. Ruiz, R.L. Headrick, A. Kazimirov, and G.G. Malliaras, *Early stages of pentacene film growth on silicon oxide.* Organic Electronics, 2004. **5**(5): p. 257-263.

200. Heringdorf, F., M.C. Reuter, and R.M. Tromp, *Growth dynamics of pentacene thin films.* Nature, 2001. **412**(6846): p. 517-520.
201. Ruiz, R., D. Choudhary, B. Nickel, T. Toccoli, K.C. Chang, A.C. Mayer, P. Clancy, J.M. Blakely, R.L. Headrick, S. Iannotta, and G.G. Malliaras, *Pentacene thin film growth.* Chemistry of Materials, 2004. **16**(23): p. 4497-4508.
202. Guo, D., T. Miyadera, S. Ikeda, T. Shimada, and K. Saiki, *Analysis of charge transport in a polycrystalline pentacene thin film transistor by temperature and gate bias dependent mobility and conductance.* Journal of Applied Physics, 2007. **102**(2): p. 023706
203. Deen, M.J., O. Marinov, J.F. Yu, S. Holdcroft, and W. Woods, *Low-frequency noise in polymer transistors.* IEEE Transactions on Electron Devices, 2001. **48**(8): p. 1688-1695.
204. Pratontep, S., M. Brinkmann, F. Nuesch, and L. Zuppiroli, *Nucleation and growth of ultrathin pentacene films on silicon dioxide: effect of deposition rate and substrate temperature.* Synthetic Metals, 2004. **146**(3): p. 387-391.
205. Pratontep, S., M. Brinkmann, F. Nuesch, and L. Zuppiroli, *Correlated growth in ultrathin pentacene films on silicon oxide: Effect of deposition rate.* Physical Review B, 2004. **69**(16): p. 165201.
206. Vandamme, L.K.J. and G. Trefan, *1/f noise in homogeneous and inhomogeneous media.* Iee Proceedings-Circuits Devices and Systems, 2002. **149**(1): p. 3-12.
207. Ishigami, M., J.H. Chen, E.D. Williams, D. Tobias, Y.F. Chen, and M.S. Fuhrer, *Hooge's constant for carbon nanotube field effect transistors.* Applied Physics Letters, 2006. **88**(20).
208. Berntgen, J., K. Heime, W. Daumann, U. Auer, F.J. Tegude, and A. Matulionis, *The 1/f noise of InP based 2DEG devices and its dependence on mobility.* IEEE Transactions on Electron Devices, 1999. **46**(1): p. 194-203.
209. Vandamme, L.K.J. *Is the 1/f noise parameter a a constant?* in *Seventh International Conference on "Noise in Physical Systems" and third International Conference on "1/f Noise"*. 1983. Montpellier, France: Elsevier Science Publ. B. V.
210. Kogan, S., *Electronic Noise and Fluctuations in Solids*. 1996, New York: Cambridge University Press.
211. Vandamme, E.P. and L.K.J. Vandamme, *Current crowding and its effect on 1/f noise and third harmonic distortion - a case study for quality assessment of resistors.* Microelectronics Reliability, 2000. **40**(11): p. 1847-1853.
212. Mottaghi, M. and G. Horowitz, *Field-induced mobility degradation in pentacene thin-film transistors.* Organic Electronics, 2006. **7**(6): p. 528-536.
213. Marinov, O., M.J. Deen, J. Yu, G. Vamvounis, S. Holdcroft, and W. Woods, *Low-frequency noise in polymer thin-film transistors.* IEE Proceedings-Circuits Devices and Systems, 2004. **151**(5): p. 466-472.
214. Sundar, V.C., J. Zaumseil, V. Podzorov, E. Menard, R.L. Willett, T. Someya, M.E. Gershenson, and J.A. Rogers, *Elastomeric transistor stamps: Reversible probing of charge transport in organic crystals.* Science, 2004. **303**(5664): p. 1644-1646.

215. Lee, J.Y., S. Roth, and Y.W. Park, *Anisotropic field effect mobility in single crystal pentacene.* Applied Physics Letters, 2006. **88**(25).
216. Dimitrakopoulos, C.D. and P.R.L. Malenfant, *Organic thin film transistors for large area electronics.* Advanced Materials, 2002. **14**(2): p. 99.
217. Horowitz, G., *Organic field-effect transistors.* Advanced Materials, 1998. **10**(5): p. 365-377.
218. Probst, K.H. and N. Karl, *Energy-Levels of Electron and Hole Traps in Band-Gap of Doped Anthracene-Crystals.* Physica Status Solidi a-Applied Research, 1975. **27**(2): p. 499-508.
219. Niemax, J., A.K. Tripathi, and J. Pflaum, *Comparison of the electronic properties of sublimation- and vapor-Bridgman-grown crystals of tetracene.* Applied Physics Letters, 2005. **86**(12): p. 122105.
220. Pflaum, J., J. Niemax, and A.K. Tripathi, *Chemical and structural effects on the electronic transport in organic single crystals.* Chemical Physics, 2006. **325**(1): p. 152-159.
221. Mayer, A.C., R. Ruiz, H. Zhou, R.L. Headrick, A. Kazimirov, and G.G. Malliaras, *Growth dynamics of pentacene thin films: Real-time synchrotron x-ray scattering study.* Physical Review B, 2006. **73**(20): p. 205307.
222. Sadowski, J.T., G. Sazaki, S. Nishikata, A. Al-Mahboob, Y. Fujikawa, K. Nakajima, R.M. Tromp, and T. Sakurai, *Single-nucleus polycrystallization in thin film epitaxial growth.* Physical Review Letters, 2007. **98**(4): p. 046104.
223. Chapman, B.D., A. Checco, R. Pindak, T. Slegrist, and C. Kloc, *Dislocations and grain boundaries in semiconducting rubrene single-crystals.* Journal of Crystal Growth, 2006. **290**(2): p. 479-484.
224. Verlaak, S., C. Rolin, and P. Heremans, *Microscopic description of elementary growth processes and classification of structural defects in pentacene thin films.* Journal of Physical Chemistry B, 2007. **111**(1): p. 139-150.
225. Tsetseris, L. and S.T. Pantelides, *Intercalation of oxygen and water molecules in pentacene crystals: First-principles calculations.* Physical Review B, 2007. **75**(15): p. 153202.
226. Verlaak, S. and P. Heremans, *Molecular microelectrostatic view on electronic states near pentacene grain boundaries.* Physical Review B, 2007. **75**(11): p. 115127.
227. Nickel, B., R. Barabash, R. Ruiz, N. Koch, A. Kahn, L.C. Feldman, R.F. Haglund, and G. Scoles, *Dislocation arrangements in pentacene thin films.* Physical Review B, 2004. **70**(12): p. 125401.
228. Ruiz, R., B. Nickel, N. Koch, L.C. Feldman, R.F. Haglund, A. Kahn, and G. Scoles, *Pentacene ultrathin film formation on reduced and oxidized Si surfaces.* Physical Review B, 2003. **67**(12): p. 125406.
229. Ruiz, R., B. Nickel, N. Koch, L.C. Feldman, R.F. Haglund, A. Kahn, F. Family, and G. Scoles, *Dynamic scaling, island size distribution, and morphology in the aggregation regime of submonolayer pentacene films.* Physical Review Letters, 2003. **91**(13): p. 136102.

230. Heringdorf, F., M.C. Reuter, and R.M. Tromp, *The nucleation of pentacene thin films.* Applied Physics a-Materials Science & Processing, 2004. **78**(6): p. 787-791.
231. Weidkamp, K.P., R.M. Tromp, and R.J. Hamers, *Epitaxial growth of large pentacene crystals on Si(001) surfaces functionalized with molecular monolayers.* Journal of Physical Chemistry C, 2007. **111**(44): p. 16489-16497.
232. Kiguchi, M., M. Nakayama, K. Fujiwara, K. Ueno, T. Shimada, and K. Saiki, *Accumulation and depletion layer thicknesses in organic field effect transistors.* Japanese Journal of Applied Physics Part 2-Letters, 2003. **42**(12A): p. L1408-L1410.
233. Gomar-Nadal, E., In Preperation, 2007.
234. Salzmann, I., S. Duhm, R. Opitz, J.P. Rabe, and N. Koch, *Impact of low 6,13-pentacenequinone concentration on pentacene thin film growth.* Applied Physics Letters, 2007. **91**(5): p. 051919.
235. Salzmann, I., R. Opitz, S. Rogaschewski, J.P. Rabe, N. Koch, and B. Nickel, *Phase separation in vacuum codeposited pentacene/6,13-pentacenequinone thin films.* Physical Review B, 2007. **75**(17): p. 174108.
236. Yang, S.Y., K. Shin, S.H. Kim, H. Jeon, J.H. Kang, H.C. Yang, and C.E. Park, *Enhanced electrical percolation due to interconnection of three-dimensional pentacene islands in thin films on low surface energy polyimide gate dielectrics.* Journal of Physical Chemistry B, 2006. **110**(41): p. 20302-20307.
237. Sadowski, J.T., T. Nagao, S. Yaginuma, Y. Fujikawa, A. Al-Mahboob, K. Nakajima, T. Sakurai, G.E. Thayer, and R.M. Tromp, *Thin bismuth film as a template for pentacene growth.* Applied Physics Letters, 2005. **86**(7): p. 073109.
238. Muller, E.M. and J.A. Marohn, *Microscopic evidence for spatially inhomogeneous charge trapping in pentacene.* Advanced Materials, 2005. **17**(11): p. 1410.
239. Jaquith, M., E.M. Muller, and J.A. Marohn, *Time-resolved electric force microscopy of charge trapping in polycrystalline pentacene.* Journal of Physical Chemistry B, 2007. **111**(27): p. 7711-7714.
240. Gonzalez, D.L. and G. Tellez, *Statistical behavior of domain systems.* Physical Review E, 2007. **76**(1): p. 011126.
241. Ruiz, R., B. Nickel, N. Koch, L.C. Feldman, R.F. Haglund, A. Kahn, F. Family, and G. Scoles, *Dynamic Scaling, Island size distribution, and morphology in the aggregation regime of submonolayer pentacene films.* Physical Review Letters, 2003. **91**: p. 136102(1-4).
242. Gomar-Nadal, E., B.R. Conrad, W.G. Cullen, and E.D. Williams, *Effect of Impurities on Pentacene Thin Film Growth for Field-Effect Transistors.* Journal of Physical Chemistry C, 112(14); 5646-5650 (2008).
243. Mayer, A.C., A. Kazimirov, and G.G. Malliaras, *Dynamics of bimodal growth in pentacene thin films.* Physical Review Letters, 2006. **97**(10): p. 105503.
244. Ruiz, R., B. Nickel, N. Koch, L.C. Feldman, R.F. Haglund, A. Kahn, and G. Scoles, *Pentacene ultrathin film formation on reduced and oxidized Si surfaces.* Physical Review B, 2003. **67**: p. 125406(1-7).

245. Pratontep, S., M. Brinkmann, F. Nüesch, and L. Zuppiroli, *Correlated growth in ultrathin pentacene films on silicon oxide: Effect of Deposition rate.* Physical Review B, 2004. **69**: p. 165201(1-7).
246. Brinkmann, M., S. Pratontep, and C. Contal, *Correlated and non-correlated growth kinetics of pnetacene in the sub-monolayer regime.* Surface Science, 2006. **600**: p. 4712-4716.
247. Sadowski, J.T., G. Sazaki, S. Nishikata, A. Al-Mahboob, Y. Fujikawa, K. Nakajima, R.M. Tromp, and T. Sakurai, *SIngle-Nucleus Polycrytallization in Thin Film Epitaxial Growth.* Physical Review Letters, 2007. **98**: p. 046104(1-4).
248. Venables, J.A., G.D.T. Spiller, and M. Hanbucken, *Nucleation and Growth of thin films.* Reports on Progress in Physics, 1984. **47**: p. 339-459.
249. Pimpinelli, A. and T.L. Einstein, *Capture-Zone Scaling in Island Nucleation: Universal Fluctuation Behavior.* Physical Review Letters, 2007. **99**(22): p. 226102.
250. Venables, J.A., *Atomic Processes in Crystal Growth.* Surface Science, 1994. **299/300**: p. 798.
251. Amar, J.G. and F. Family, *Critical Cluster-Size - Island Morphology and Size Distribution in Submonolayer Epitaxial-Growth.* Physical Review Letters, 1995. **74**(11): p. 2066-2069.
252. Arciprete, F., E. Placidi, V. Sessi, M. Fanfoni, F. Patella, and A. Balzarotti, *How kinetics drives the two- to three-dimensional transition in semiconductor strained heterostructures: The case of InAs/GaAs(001).* Applied Physics Letters, 2006. **89**(4): p. 041904.
253. Mayer, A.C., R. Ruiz, H. Zhou, R.L. Headrick, A. Kazimirov, and G.G. Malliaris, *Growth dynamics of pentacene thin films: Real-time synchrotron x-ray scattering study.* Physical Review B, 2006. **73**: p. 205307(1-5).
254. Evans, J.W., P.A. Thiel, and M.C. Bartelt, *Morphological evolution during epitaxial thin film growth: Formation of 2D islands and 3D mounds.* Surface Science Reports, 2006. **61**(1-2): p. 1-128.
255. Tsai, V., X.S. Wang, E.D. Williams, J. Schneir, and R. Dixson, *Conformal oxides on Si surfaces.* Applied Physics Letters, 1997. **71**(11): p. 1495-1497.
256. Thurmer, K., D.J. Liu, E.D. Williams, and J.D. Weeks, *Onset of step antibanding instability due to surface electromigration.* Physical Review Letters, 1999. **83**(26): p. 5531-5534.
257. Parisse, P., S. Picozzi, and L. Ottaviano, *Electronic, morphological and transport properties of 6,13-pentacenequinone thin films: Theory and experiments.* Organic Electronics, 2007. **8**(5): p. 498-504.
258. Northrup, J.E. and M.L. Chabinyc, *Gap states in organic semiconductors: Hydrogen- and oxygen-induced states in pentacene.* Physical Review B, 2003. **68**(4): p. 041202.
259. Verlaak, S. and P. Heremans, *Molecular microelectrostatic view on electronic states near pentacene grain boundaries.* Physical Review B, 2007. **75**(11): p. 115127

260. Pimpinelli, A., H. Gebremariam, and T.L. Einstein, *Evolution of terrace-width distributions on vicinal surfaces: Fokker-Planck derivation of the generalized Wigner surmise.* Physical Review Letters, 2005. **95**(24): p. 246101.
261. Blackman, J.A. and P.A. Mulheran, *Scaling behavior in submonolayer film growth: A one-dimensional model.* Physical Review B, 1996. **54**(16): p. 11681-11692.
262. Mulheran, P.A. and J.A. Blackman, *Capture zones and scaling in homogeneous thin-film growth.* Physical Review B, 1996. **53**(15): p. 10261-10267.
263. Mulheran, P.A. and J.A. Blackman, *The Origins of Island Size Scaling in Heterogeneous Film Growth.* Philosophical Magazine Letters, 1995. **72**(1): p. 55-60.
264. Brinkmann, M., S. Graff, and F. Biscarini, *Mechanism of nonrandom pattern formation of polar-conjugated molecules in a partial wetting regime.* Physical Review B, 2002. **66**(16): p. 165430.
265. Brinkmann, M., F. Biscarini, C. Taliani, I. Aiello, and M. Ghedini, *Growth of mesoscopic correlated droplet patterns by high-vacuum sublimation.* Physical Review B, 2000. **61**(24): p. 16339-16342.
266. Giesen, M. and T.L. Einstein, *Analysis of terrace width distributions on vicinal copper surfaces using the 'Wigner surmise': comparison with Gaussian approach.* Surface Science, 2000. **449**(1-3): p. 191-206.
267. Einstein, T.L. and O. Pierre-Louis, *Implications of random-matrix theory for terrace-width distributions on vicinal surfaces: improved approximations and exact results.* Surface Science, 1999. **424**(1): p. L299-L308.
268. Street, R.A., D. Knipp, and A.R. Völkel, *Hole transport in polycrystalline pentacene transistors.* Applied Physics Letters, 2002. **80**: p. 1658-1660.
269. Verlaak, S., V. Arkhipov, and P. Heremans, *Modeling of transport in polycrystalline organic semiconductor films.* Applied Physics Letters, 2003. **82**(5): p. 745-747.
270. Muller, E.M. and J.A. Marohn, *Microscopic evidence for spatialy inhomogenous charge trapping in pentacene.* Advanced Materials, 2005. **17**: p. 1410-1414.
271. Kalb, W.L., F. Meier, K. Mattenberger, and B. Batlogg, *Defect healing at room temperature in pentacene thin films and improved transistor performance.* Physical Review B, 2007. **76**(18): p. 184112.
272. Ju-Hyung, K., H. Sung-Yoon, K. Tae-il, and H.L. Hong, *Thin pentacene interlayer for polymer bulk-heterojunction solar cell.* Applied Physics Letters, 2008. **93**(14): p. 143305.
273. Knipp, D., R.A. Street, A. Volkel, and J. Ho, *Pentacene thin film transistors on inorganic dielectrics: Morphology, structural properties, and electronic transport.* Journal of Applied Physics, 2003. **93**(1): p. 347-355.
274. Gomar-Nadal, E., B.R. Conrad, W.G. Cullen, and E.A. Willams, *Effect of impurities on pentacene thin film growth for field-effect transistors.* Journal of Physical Chemistry C, 2008. **112**(14): p. 5646-5650.
275. Choudhary, D., P. Clancy, and D.R. Bowler, *Adsorption of pentacene on a silicon surface.* Surface Science, 2005. **578**(1-3): p. 20-26.

276. Ruiz, R., A.C. Mayer, G.G. Malliaras, B. Nickel, G. Scoles, A. Kazimirov, H. Kim, R.L. Headrick, and Z. Islam, *Structure of pentacene thin films.* Applied Physics Letters, 2004. **85**(21): p. 4926-4928.
277. Yang, H.C., T.J. Shin, M.M. Ling, K. Cho, C.Y. Ryu, and Z.N. Bao, *Conducting AFM and 2D GIXD studies on pentacene thin films.* Journal of the American Chemical Society, 2005. **127**(33): p. 11542-11543.
278. Fritz, S.E., S.M. Martin, C.D. Frisbie, M.D. Ward, and M.F. Toney, *Structural characterization of a pentacene monolayer on an amorphous SiO_2 substrate with grazing incidence X-ray diffraction.* Journal of the American Chemical Society, 2004. **126**(13): p. 4084-4085.
279. Schroeder, P.G., C.B. France, J.B. Park, and B.A. Parkinson, *Energy level alignment and two-dimensional structure of pentacene on Au(111) surfaces.* Journal of Applied Physics, 2002. **91**(5): p. 3010-3014.
280. Guaino, P., A.A. Cafolla, D. Carty, G. Sheerin, and G. Hughes, *An STM investigation of the interaction and ordering of pentacene molecules on the Ag/Si(111)-(root 3 x root 3)R30 degrees surface.* Surface Science, 2003. **540**(1): p. 107-116.
281. Repp, J., G. Meyer, S.M. Stojkovic, A. Gourdon, and C. Joachim, *Molecules on insulating films: Scanning-tunneling microscopy imaging of individual molecular orbitals.* Physical Review Letters, 2005. **94**(2): p. 026803
282. Al-Mahboob, A., J.T. Sadowski, T. Nishihara, Y. Fujikawa, Q.K. Xue, K. Nakajima, and T. Sakurai, *Epitaxial structures of self-organized, standing-up pentacene thin films studied by LEEM and STM.* Surface Science, 2007. **601**(5): p. 1304-1310.
283. Lublow, M. and H.J. Lewerenz, *Real-time monitoring of SiO_2/Si(111) interlayer etching by Brewster-angle reflectometry.* Surface Science, 2008. **602**(9): p. 1677-1687.
284. Lublow, M. and H.J. Lewerenz, *Combined AFM and Brewster-angle analysis of gradually etched ultrathin SiO2 - Comparison with SRPES results.* Surface Science, 2007. **601**(7): p. 1693-1700.
285. Homma, Y., M. Suzuki, and N. Yabumoto, *Observation of Atomic Step Morphology on Silicon-Oxide Surfaces.* Journal of Vacuum Science & Technology a-Vacuum Surfaces and Films, 1992. **10**(4): p. 2055-2058.
286. Fritz, S.E., T.W. Kelley, and C.D. Frisbie, *Effect of dielectric roughness on performance of pentacene TFTs and restoration of performance with a polymeric smoothing layer.* Journal of Physical Chemistry B, 2005. **109**(21): p. 10574-10577.
287. Stockhausen, A., T.U. Kampen, and W. Monch, *Oxidation of Clean and H-Passivated Si(111) Surfaces.* Applied Surface Science, 1992. **56-8**: p. 795-801.
288. Westermann, J., H. Nienhaus, and W. Monch, *Oxidation Stages of Clean and H-Terminated Si(001) Surfaces at Room-Temperature.* Surface Science, 1994. **311**(1-2): p. 101-106.
289. Hasunuma, R., J. Okamoto, N. Tokuda, and K. Yamabe, *Nommiformity in ultrathin SiO_2 on Si(111) characterized by conductive atomic force*

microscopy. Japanese Journal of Applied Physics Part 1-Regular Papers Short Notes & Review Papers, 2004. **43**(11B): p. 7861-7865.
290. Ono, Y., M. Tabe, and H. Kageshima, *Scanning-Tunneling-Microscopy Observation of Thermal Oxide-Growth on Si(111)7x7 Surfaces.* Physical Review B, 1993. **48**(19): p. 14291-14300.
291. Watanabe, H., T. Baba, and M. Ichikawa, *Mechanism of layer-by-layer oxidation of Si(001) surfaces by two-dimensional oxide-island nucleation at SiO_2/Si interfaces.* Japanese Journal of Applied Physics Part 1-Regular Papers Short Notes & Review Papers, 2000. **39**(4B): p. 2015-2020.
292. Hasunuma, R., A. Ando, K. Miki, and Y. Nishioka, *Analysis on electrical properties of ultrathin SiO_2/Si(111) interfaces with an atomic force microscope.* Applied Surface Science, 2000. **162**: p. 547-552.
293. Neuwald, U., H.E. Hessel, A. Feltz, U. Memmert, and R.J. Behm, *Initial-Stages of Native Oxide-Growth on Hydrogen Passivated Si(111) Surfaces Studied by Scanning Tunneling Microscopy.* Applied Physics Letters, 1992. **60**(11): p. 1307-1309.
294. Moore, T.L., B.R. Conrad, B. Riddick, and E.D. Williams, *In Preparation*. 2008.
295. Nabok, D., P. Puschnig, C. Ambrosch-Draxl, O. Werzer, R. Resel, and D.M. Smilgies, *Crystal and electronic structures of pentacene thin films from grazing-incidence x-ray diffraction and first-principles calculations.* Physical Review B, 2007. **76**(23): p. 235322
296. Busmann, H.G., R. Hiss, H. Gaber, and I.V. Hertel, *Growth mechanisms of C_{60}-molecular beam epitaxy on mica.* Surface Science, 1993. **289**(3): p. 381-388.
297. Palasantzas, G., D. Tsamouras, and J.T.M. De Hosson, *Roughening aspects of room temperature vapor deposited oligomer thin films onto Si substrates.* Surface Science, 2002. **507-510**: p. 357-361.
298. Goldberg, J.L., X.S. Wang, N.C. Bartelt, and E.D. Williams, *Surface Height Correlation-Functions of Vicinal Si(111) Surfaces Using Scanning Tunneling Microscopy.* Surface Science, 1991. **249**(1-3): p. L285-L292.
299. Gotoh, M., K. Sudoh, H. Itoh, K. Kawamoto, and H. Iwasaki, *Analysis of SiO_2/Si(001) interface roughness for thin gate oxides by scanning tunneling microscopy.* Applied Physics Letters, 2002. **81**(3): p. 430-432.
300. Ishigami, M., J.H. Chen, W.G. Cullen, M.S. Fuhrer, and E.D. Williams, *Atomic structure of graphene on SiO2.* Nano Letters, 2007. **7**(6): p. 1643-1648.
301. Teichert, C., J.F. Mackay, D.E. Savage, M.G. Lagally, M. Brohl, and P. Wagner, *Comparison of Surface-Roughness of Polished Silicon-Wafers Measured by Light-Scattering Topography, Soft-X-Ray Scattering, and Atomic-Force Microscopy.* Applied Physics Letters, 1995. **66**(18): p. 2346-2348.